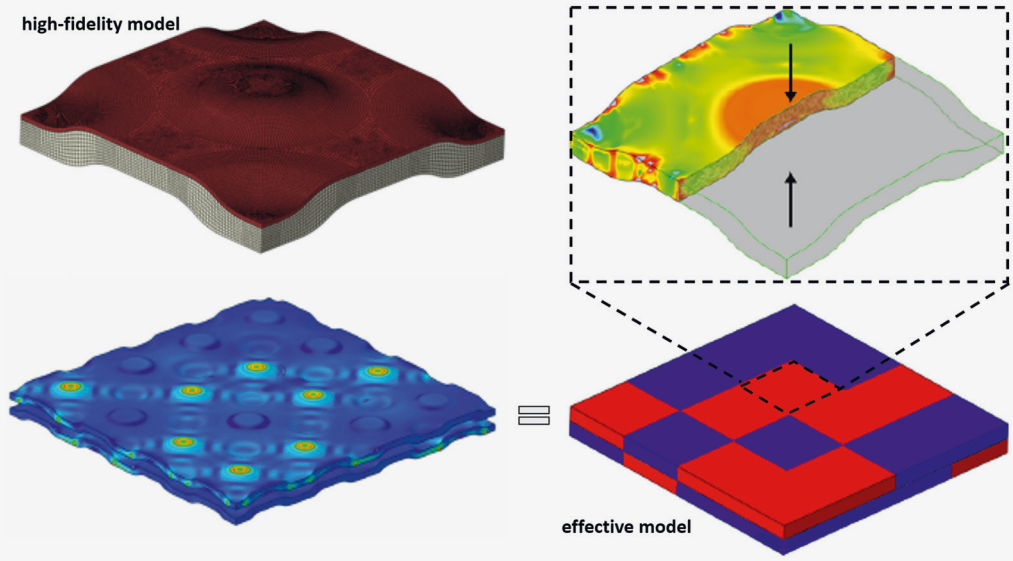

A constitutive theory to represent non-idealities in contacting of SOC interconnect contacts

Ralston Martin Pinto

Energie & Umwelt / Energy & Environment
Band / Volume 673
ISBN 978-3-95806-846-9

Mitglied der Helmholtz-Gemeinschaft

JÜLICH
Forschungszentrum

Schriften des Forschungszentrums Jülich
Reihe Energie & Umwelt / Energy & Environment Band / Volume 673

Forschungszentrum Jülich GmbH
Institute of Energy Materials and Devices (IMD)
Werkstoffsynthese und Herstellungsverfahren (IMD-2)

A constitutive theory to represent non-idealities in contacting of SOC interconnect contacts

Ralston Martin Pinto

Schriften des Forschungszentrums Jülich
Reihe Energie & Umwelt / Energy & Environment Band / Volume 673

ISSN 1866-1793 ISBN 978-3-95806-846-9

Bibliografische Information der Deutschen Nationalbibliothek.
Die Deutsche Nationalbibliothek verzeichnet diese Publikation in der
Deutschen Nationalbibliografie; detaillierte Bibliografische Daten
sind im Internet über http://dnb.d-nb.de abrufbar.

Herausgeber und Vertrieb:	Forschungszentrum Jülich GmbH Zentralbibliothek, Verlag 52425 Jülich Tel.: +49 2461 61-5368 Fax: +49 2461 61-6103 zb-publikation@fz-juelich.de www.fz-juelich.de/zb
Umschlaggestaltung:	Grafische Medien, Forschungszentrum Jülich GmbH
Druck:	Grafische Medien, Forschungszentrum Jülich GmbH
Copyright:	Forschungszentrum Jülich 2025

Schriften des Forschungszentrums Jülich
Reihe Energie & Umwelt / Energy & Environment, Band / Volume 673

D 82 (Diss. RWTH Aachen University, 2025)

ISSN 1866-1793
ISBN 978-3-95806-846-9

Vollständig frei verfügbar über das Publikationsportal des Forschungszentrums Jülich (JuSER)
unter www.fz-juelich.de/zb/openaccess.

Abstract

The electrical contact resistance at solid oxide cell (SOC) contacts is a key aspect which contributes to ohmic losses in an SOC stack. These resistances are primarily dependent on the mechanical contact pressures applied in the active area, which are influenced by non-idealities caused by manufacturing limitations. Finite element methods (FEM) can be used to study these phenomena, but conventional simulation approaches are often impractical due to excessive computation times. Such excessive computational times are caused by complex designs of repeating components and high mesh resolutions required for accurate modeling.

To address these challenges, this work investigates the use of computational homogenization techniques in the SOC stack. These methods characterize the periodically repeating structure of interconnect contacts as an equivalent material response, capturing the required effects while significantly reducing computation time. The non-idealities arising from manufacturing tolerances are incorporated using a constitutive material model demonstrating an *offset-formulation*, while the soft porous coating on the contacts is represented through a *coating-formulation*. Furthermore, the model shows temperature-dependent and rate-dependent behavior, making it capable of simulating the various loading stages in the lifecycle of an SOC contact.

On developing a simplified modeling approach for the aforementioned challenges, a framework is developed to extrapolate key parameters relevant to SOC performance directly from this simplified model. This motivates the use of the simplified model as a replacement of full-field modeling approaches. The developed modeling framework is validated through experimental case studies, which focus on evaluating the mechanical contact pressure after stacking and also the electrical contact resistance during operation.

The findings from this work have important implications for optimizing several process parameters to achieve an ideal contact configuration in the active area of an SOC stack. These parameters may include stacking force, tolerance limits, temperature distribution,

material properties and the geometric design of contacts, which can be evaluated efficiently using the proposed computational approach.

Kurzfassung

Der elektrische Kontaktwiderstand an den Kontakten von Festoxidzellen (SOC) ist ein wichtiger Aspekt, der zu den ohmschen Verlusten in einem SOC-Stack beiträgt. Diese Widerstände hängen in erster Linie von den im aktiven Bereich ausgeübten mechanischen Kontaktdrücken ab, die durch Nichtidealitäten aufgrund von Fertigungsbeschränkungen beeinflusst werden. Finite-Elemente-Methoden (FEM) können zur Untersuchung dieser Phänomene verwendet werden, doch herkömmliche Simulationsansätze sind aufgrund übermäßiger Rechenzeiten häufig unpraktisch. Solche übermäßigen Rechenzeiten werden durch komplexe Designs sich wiederholender Komponenten und hohe Maschenauflösungen verursacht, die für eine genaue Modellierung erforderlich sind.

Um diese Herausforderung anzugehen, untersucht diese Arbeit die Verwendung von rechnergestützten Homogenisierungstechniken im SOC-Stack. Diese Methoden charakterisieren die sich periodisch wiederholende Struktur der Verbindungskontakte als äquivalente Materialreaktion und erfassen die erforderlichen Effekte bei gleichzeitiger erheblicher Reduzierung der Rechenzeit. Die Nichtidealitäten, die sich aus Fertigungstoleranzen ergeben, werden mithilfe eines konstitutiven Materialmodells berücksichtigt, das eine *Offset-Formulierung* demonstriert, während die weiche, poröse Beschichtung der Kontakte durch eine *Beschichtungsformulierung* dargestellt wird. Darüber hinaus zeigt das Modell ein temperatur- und geschwindigkeitsabhängiges Verhalten, wodurch es die verschiedenen Belastungsphasen im Lebenszyklus eines SOC-Kontakts simulieren kann.

Bei der Entwicklung eines vereinfachten Modellierungsansatzes für die oben genannten Herausforderungen wird ein Rahmen entwickelt, um wichtige Parameter, die für die SOC-Leistung relevant sind, direkt aus diesem vereinfachten Modell zu extrapolieren. Dies motiviert die Verwendung des vereinfachten Modells als Ersatz für Vollfeld-Modellierungsansätze. Der entwickelte Modellierungsrahmen wird durch experimentelle Fallstudien validiert, die sich auf die Bewertung des mechanischen Kontaktdrucks nach dem Stapeln und auch des elektrischen Kontaktwiderstands während des Betriebs konzentrieren.

Die Erkenntnisse aus dieser Arbeit haben wichtige Auswirkungen auf die Optimierung mehrerer Prozessparameter, um eine ideale Kontaktkonfiguration im aktiven Bereich eines SOC-Stapels zu erreichen. Diese Parameter können Stapelkraft, Toleranzgrenzen, Temperaturverteilung, Materialeigenschaften und das geometrische Design von Kontakten umfassen, die mit dem vorgeschlagenen rechnerischen Ansatz effizient bewertet werden können.

Acknowledgements

I would like to express my heartfelt gratitude to Hon. Prof. Norbert H. Menzler for his invaluable insights and for sharing his vast knowledge into SOC technology with me. Thank you for always making time for me and for always looking out for me.

A special thanks to my supervisor, Dr. Nils Giesselmann, for consistently pushing me beyond my limits and helping me uncover my true potential. Your practical reasoning challenged my ideas and transformed my theories into the robust work that is reflected here.

I am immensely grateful to Dr. Fabian Welschinger for co-supervising me, and providing me with his immense knowledge. The intensive discussions with you gave me valuable insights and your advanced reasoning gave my work direction. Thank you for your time, effort, and for helping to shape my work so significantly.

My deepest thanks goes to my mentor, Dr. Holger Reinshagen. Your guidance has been a cornerstone throughout my journey. You helped me navigate the toughest decisions with clarity, and after every discussion, even the most complicated problems seemed manageable. I truly could not have succeeded without your knowledge, advice, and unwavering mentorship.

I also wish to extend my sincere thanks to Prof. Dr. Robert Vaßen for your excellent reasoning and valuable insights. You are among the smartest individuals I have had the privilege to meet. Even though you were not deeply involved into my topic, our discussions were profoundly insightful. You always identified the weakest links of my work and inspired me to refine and improve it.

To my girlfriend, Janice Elangikal, thank you for standing by me through the highs and lows of this journey and for believing in me until the very end.

I am deeply thankful to Randell Pinto and Ericka Guedes. Your support and companionship made all the difference.

Lastly, my heartfelt gratitude goes to my parents, Treza and Martin Pinto, for encouraging me to take on this challenge and for their constant support and encouragement throughout this journey.

Abbreviations

1-D	One-dimensional
2-D	Two-dimensional
3-D	Three-dimensional
ASR	Area specific resistance
C3D8	Hexagonal linear elements
CGO	Gadolinium-doped ceria
CSS8	Continuum Solid Shell Elements
ES-SOFC	Electrolyte supported-solid oxide fuel cell
FC	Fuel cell
FDP-8010E	Fujifilm software
FE	Finite Element
LSC	Lanthanum strontium-substituted cobalt
HPC	High performance cluster
LSCF	Lanthanum strontium cobalt ferrite
LSM	Strontium-doped lanthanum manganite
OCV	Open circuit voltage
ORR	Oxygen reduction reaction
RVE	Representative volume element
RU	Repeat unit
SRU	Single repeat unit
SOC	Solid oxide cell
SOEC	Solid oxide electrolysis cell
SOFC	Solid oxide fuel cell
TEC	Thermal expansion coefficient
TPB	Triple phase boundary
T	Temperature in $^{\circ}C$
YSZ	Yttria-stabilized zirconia

Notations

$\phi(\boldsymbol{\sigma})$	Yield criteria
σ_{eq}	Equivalent stress
σ_0	Effective yield stress
α_{xx}	Coefficients that define plastic orhtotropy in the Hill tensor.
σ_{xx}	Stress component in xx-direction
σ_{eff}	Effective yield stress
$\boldsymbol{\varepsilon}$	Second order strain-tensor
$\boldsymbol{\varepsilon}^e$	Second-order elastic strain-tensor
$\boldsymbol{\varepsilon}^{of}$	Second-order offset strain-tensor
$\boldsymbol{\varepsilon}^{co}$	Second-order coating strain-tensor
$\boldsymbol{\varepsilon}^{vp}$	Second-order visco plastic strain-tensor
$\psi(\boldsymbol{\varepsilon}^e)$	Specific free energy for anisotropic elasticity
$\mathbb{C}$	Fourth-order orhtotropic elasticity tensor
$\mathbb{C}_{ijkl}$	Fourth order tensor component ijkl of tensor $\mathbb{C}$
$\boldsymbol{N}^{of}$	Second-order tensor in the out-of-plane direction
$\tilde{\varepsilon}^{of}_{tol}$	Limiting offset strain in the out-of-plane direction
$\tilde{\varepsilon}^{of}$	Magnitude of offset strain
$\tilde{\varepsilon}^{co}$	Magnitude of coating strain
$\boldsymbol{N}^{co}$	Second-order tensor in the out-of-plane direction
$\mathbb{M}$	Fourth-order Hill-type tensor
$\mathbb{M}_{ijkl}$	Fourth order tensor component ijkl of tensor $\mathbb{M}$
$\dot{E}_0, \sigma_0, n$	viscoplastic material parameters for power-law equation
$\mathbb{I}^s$	Fourth-order symmetric identity tensor
$\mathbb{P}$	Fourth-order projection tensor
$\boldsymbol{\sigma}^{tr}$	Trial stress for algorithmic iteration
$\lambda(\boldsymbol{\sigma})$	Plastic multiplier
$\boldsymbol{r}(\boldsymbol{\sigma})$	Residual for local Newton iteration
$\mathcal{D}$	Dissipation energy

T	Temperature in K
$\boldsymbol{\alpha}^{th}$	Second order tensor representing anisotropic thermal expansion coefficients
$\mathbb{A}$	Fourth-order tensor
$\mathbb{A}_{ijkl}$	Fourth order tensor component ijkl of tensor $\mathbb{A}$
$\boldsymbol{\varepsilon}^{tot}$	Second-order total strain-tensor
$\boldsymbol{\varepsilon}^{th}$	Second-order thermal strain-tensor
$\boldsymbol{u}$	Displacement vector
$\boldsymbol{n}$	Unit normal vector
$\boldsymbol{t}$	Stress vector
ρ	Density
V	Volume
$\boldsymbol{b}$	Vector representing body forces
$\boldsymbol{q}$	Vector representing heat flux across surface
r	Heat supplied across volume
e	Internal energy
η	Entropy
$\boldsymbol{N}$	Flow direction vector for plastic flow
$R_{contact}$	Contact resistance
$\mathcal{F}_0, \mathcal{F}_n$	Domain of experimentally applied forces for contact experiments

Contents

1 Introduction

1.1 Motivation

In recent decades, significant technological advancements in solid oxide cells (SOCs) have led to new designs and materials which has made SOC technology a promising solution for clean energy conversion. However, for this technology to reach widespread commercialization and accelerate its development, it must meet market demands in terms of reliability, robustness, efficiency and cost. To achieve this, a fundamental understanding of all designed components in an SOC stack, relevant manufacturing processes and their impact on the overall product is required. While such knowledge can be gained through extensive experimentation and testing on a cell level, these tests may become cost-prohibitive and time-consuming when carried out on the stack level. This is attributed to the complexity and number of repeat units in a stack [1, 2].

To understand stack-level phenomena more effectively, simulation tools may provide attractive alternative approaches. Structural and multiphysics simulations may be used to to intuitively explore and analyze SOC designs without high costs associated with physical experiments [3, 4]. Additionally, internal conditions within a closed SOC stack at operational temperatures may be difficult to measure experimentally and can be estimated through simulations. Moreover, some intrinsic quantities like stresses, fluxes, etc. may be explicitly evaluated using simulation tools which is vital for stack design and can be difficult to visualize using an experimental setup [5,6]. Therefore, simulation methods are a powerful tool which complement experimental approaches to obtain a thorough analysis of an SOC stack system.

One key application of structural simulations in SOCs is estimating electrical resistance within a stack, particularly as it relates to the mechanical contact configuration between repeat units [7,8]. For optimal stack performance, the individual repeat units must establish sufficient contact pressure with the adjacent repeat unit to ensure effective electrical

conductivity. Application of mechanical pressure on the contacts ensures sufficient surface area for electron flow which reduces electrical resistance. While insufficient contact pressures cause loss of performance through increased contact resistance, excessively high contact pressures may lead to plastic deformation and eventual component failure. Therefore, a suitable magnitude of contact pressures are essential for both, performance and durability of the stack [9].

Although finite element simulation methods are commonly used in research and development, these simulations are often associated with ideal design conditions. In reality, however, manufacturing variations may cause deviations from the ideal design because of machining limits and tolerances. For a consistent stack performance, each cell manufactured should meet strict quality standards [10, 11]. Even a small deviation may significantly affect the overall performance of the stack. Therefore, understanding the influence of manufacturing tolerances on critical components is essential for setting appropriate tolerance limits. [12, 13]

One such component in a planar SOC stack is the interconnect, which is particularly sensitive to dimensional tolerances, especially, the variability in height dimensions of individual contacts [14–17]. The interconnect acts as a compartment that separate air from fuel, and variations in contact dimensions can lead to non-uniform fuel distribution, accelerating degradation and potentially causing failure [18, 19]. Additionally, the function of the interconnect is to ensure electrical conductivity between repeat units. Dimensional variability on the interconnect contacts may result in heterogeneous contact pressure distributions which directly influence ohmic contact resistance and therefore, stack performance. [20–25].

Because of the cost and effort associated with experimental approaches, alternative methods are required to evaluate the electrical resistance at a stack level, with finite element methods as a promising approach. However, conventional finite element simulation techniques for stack-level analysis for the Bosch-Ceres stack design are computationally intensive and require significant time for completion [26–29]. Furthermore, considering such kind of intricate interconnect designs along with their tolerances and modeling thousands of such interconnect contacts for each repeat unit demands impractical modeling effort. The goal of this work is to overcome these challenges by creating a simplified model and reducing simulation times without compromising on accuracy. While doing so, the model should also consider geometric variability due to tolerances at each contact, enabling the simulation of real-world manufactured components. This makes it possible to estimate

their impact on stack performance and suggest appropriate measures to increase robustness and reliability of manufactured stacks.

1.2 Research Objectives

Using the stated challenges as motivation to develop new methods, the objectives of this work are described in this section

- This work attempts to create a methodology to simulate mechanical aspects of SOC components.
- The challenge of large computational times associated with conventional approaches are addressed.
- Non-idealities associated with manufacturing processes of components are taken into consideration.
- Lastly, the evaluation of certain key parameters like contact pressure and electrical contact resistance which are known to influence stack performance is conducted.

1.3 Outline

In Chapter 2, a brief overview of an SOC and its components is provided, alongside certain relevant fundamentals on continuum mechanics and computational homogenization are covered. Chapter 3 aims on performing experimental tests of SOC contacts with a focus on evaluating their material behavior. Furthermore, investigations on how this behavior varies under different loading conditions throughout the SOC contact life-cycle are carried out. Chapter 4 highlights the challenge associated with long computational times and proposes the use of homogenization techniques for model reduction. Upon comparing with experimental tests and identifying distinct deviations, the missing features are attempted to be incorporated into the simplified model.

In Chapter 5, the necessary model equations are developed taking into consideration the experimental deviations and are implemented in an algorithmic framework. Chapter 6 discusses the calibration of parameters for the simplified model to match the full-field model, with validation performed for various load-case scenarios. In Chapter 7, a post-processing workflow is outlined to extract the model parameters relevant to the electrical

contact problem. Finally, in Chapter 8, a comparison of simulation results with experimental investigations are carried out, which validate the proposed methodology for the intended use-case.

2 Literature

To meet the objectives outlined in Chapter 1, the literature relevant to two technical areas require attention. First, a comprehensive understanding of the SOC design is essential to address challenges related to component functionality and the evaluation of key performance parameters. Then, a fundamental understanding of computational mechanics is necessary to develop the theoretical framework needed to effectively tackle the aforementioned challenges stated in Chapter 1.

This chapter addresses these two key aspects. It begins with an overview of SOCs, discussing their working principles, components, types, and performance indicators, while providing a detailed explanation of the specific design relevant to this work. Later, the chapter introduces the fundamentals of continuum mechanics, including the definitions of quantities such as strain and stress, as well as the thermodynamic considerations for material modeling. Additionally, the theory of plasticity and computational homogenization are discussed to establish the theoretical foundation for the subsequent chapters.

2.1 Fundamentals of Solid Oxide Cells

As this work is primarily motivated for the Fuel Cell (FC) application of SOCs, we are concerned with the operational principles and fundamentals of the solid oxide fuel cells (SOFCs) in this section. A similar design may be used for the electrolysis application in solid oxide electrolysis cell (SOEC) mode [30, 31]. Thus, the challenges outlined and methodology used in this work is also relevant for SOEC designs. Therefore, for a broader range of design applications, this work addresses all SOC designs, however, it is primarily applied to the SOFC use-case.

2.1.1 Working principle

SOFCs are usually based on ceramic materials and operate within a temperature range between 600°C to 1000°C [32]. In a typical SOFC design, as illustrated in Figure 2.1(a) [33], a solid-state electrolyte is sandwiched between an anode and a cathode which have a porous microstructure. The fuel consisting of hydrogen (H_2) or hydrogen based compounds are supplied to the anode, while the cathode is kept in the vicinity of air containing oxygen (O_2) [34]. The working principle of an SOFC requires the occurrence of a redox reaction where the fuel gets oxidized at the anode and the oxygen from the air gets reduced at the cathode. During this process the oxygen atoms react with free electrons at the cathode to form oxygen ions. The oxygen ions are transported through the porous cathode and dense electrolyte layers to the anode where hydrogen atoms are oxidized to from hydrogen ions and free electrons. This results in a chemical reaction with the formation of water (H_2O) as a by-product and the transportation of electrons through an external circuit which generates electricity [35–37].

The interfaces between the anode-cathode-electrolyte layers must be mechanically robust and chemically compatible at operational temperatures over prolonged timescales [38]. For practical applications, a single SOFC unit generates a rather small magnitude of voltage for the flow of electricity, therefore multiple SOFCs are stacked together forming a series circuit which act as a large power source as demonstrated in Figure 2.1(b) [33]. These individual fuel cells are often separated by interconnecting materials which perform the task of current collection and provide mechanical stability to the stack [39].

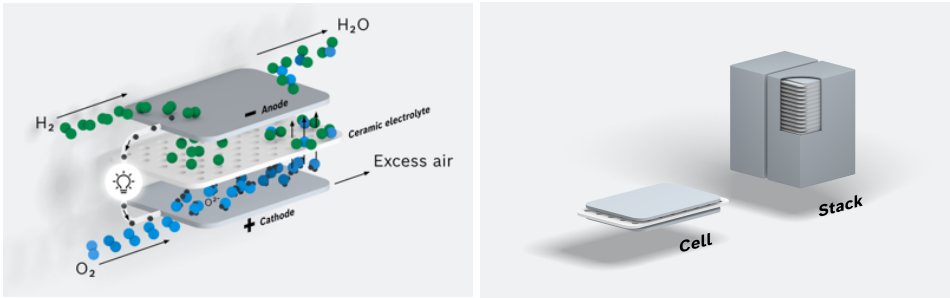

(a) Cell (b) Stack

Figure 2.1: Fundamentals of fuel cells

The overall chemical reaction occurring during the process combines hydrogen molecules

with oxygen molecules to from water and can be expressed as:

$$H_2 + \frac{1}{2} O_2 \longrightarrow H_2O \tag{2.1.1}$$

At the cathode, the oxygen molecules ionize to form O^{2-} ions and may be expressed with the following reaction:

$$\frac{1}{2} O_2 + 2\,e^- \longrightarrow O^{2-} \tag{2.1.2}$$

At the anode, hydrogen molecules are oxidized to form H^+ with the release of free electrons e^- and is expressed in the following chemical equation as,

$$H_2 \longrightarrow 2\,H^+ + 2\,e^- \tag{2.1.3}$$

followed by the combination with the free O^{2-} ions to form water and is expressed in the form,

$$2\,H^+ + O^{2-} \longrightarrow H_2O \tag{2.1.4}$$

Upon transportation of the O^{2-} ions from the cathode on to the anode following the reactions in Equation 2.1.2, Equation 2.1.3 and Equation 2.1.4 occurs, giving the overall chemical reaction shown in Equation 2.1.1.

2.1.2 Components

As already described in subsection 2.1.1, the SOFC comprises three fundamental components which are the anode, cathode and electrolyte. Upon stacking individual cells together, the role of the interconnect becomes vital. In order to operate efficiently, each of these components must possess certain inherent properties which are highlighted as follows:

Cathode: The cathode plays a critical role in the oxygen reduction reaction (ORR), which influences the performance of SOFC. Typically, the cathode must exhibit high electronic conductivity, a thermal expansion coefficient (TEC) compatible with other cell components and chemical stability under operational conditions. Additionally, it should possess a porous microstructure which enhances the ORR beyond the triple phase boundary (TPB) of the cathode/electrolyte interface and lastly, it should have high catalytic activity for oxygen molecule reduction. For high-temperature SOFC applications, materials such as lanthanum strontium manganite (LSM: $La_{1-x}Sr_xMnO_{3-\delta}$) are used, which have a

perovskite structure, wherein the doped strontium replaces lanthanum enhancing its electronic conductivity. However, its limited oxide-ion conductivity confines the ORR primarily to the TPB which limits its performance. Furthermore, thermal and mechanical degradation of LSM at elevated operational temperatures has led to the development of alternative materials for intermediate-temperature SOFCs [40–42].

One such alternative is lanthanum cobaltite ($LaCoO_3$), which, when doped with strontium, forms strontium-substituted cobaltite perovskite (LSC: $La_{1-x}Sr_xCoO_{3-\delta}$). LSC is a mixed ionic-electronic conductor (MIEC) with excellent ionic conductivity and catalytic properties for ORR. However, its high TEC can create compatibility issues with other cell components, particularly commonly used electrolytes like yttria-stabilized zirconia (YSZ) and gadolinium-doped ceria (CGO). In order to tackle these limitations, Co was substituted with Fe, resulting in lanthanum strontium cobalt ferrite (LSCF: $La_{1-x}Sr_xCo_{1-y}Fe_yO_{3-\delta}$), a state-of-the-art cathode material. LSCF possesses good electronic conductivity at an intermediate temperature ranges. Additionally, mixed valence states of $Fe_3{}^+/Fe_4{}^+$ and $Co_3{}^+/Co_4{}^+$ facilitate the formation of oxygen vacancies, thereby enhancing ionic conductivity. Alongside, the TEC of LSCF aligns well with that of other cell components, making it more compatible. Despite the advantages, one limitation is that LSCF reacts with YSZ and affects the cell performance over time. However, it remains compatible with CGO. To address the incompatibility with YSZ, incorporating a ceria-based barrier layer between the cathode and electrolyte has proven to be an effective solution.

Lastly, the primary challenges associated with LSCF involve its degradation over time during operation, which includes strontium segregation and chromium poisoning. Strontium segregation leads to the formation of a SrO layer on the cathode surface, inhibiting the ORR at the air/cathode interface. Whereas, chromium poisoning arises from the volatilization of chromium species from metallic interconnects at operational temperatures. These chromium species deposit on the cathode surface, further degrading its performance.

Electrolyte: The electrolyte is a dense ceramic layer, through which oxide ions migrate from the cathode to the anode. Consequently, the electrolyte must exhibit high oxide-ion conductivity, which depends on its internal resistance to ion flow and the distance traveled by oxide ions between the electrodes. Moreover, the electrolyte material must be electronically insulating as any electronic conductivity could short-circuit the cell. Furthermore, the electrolyte should be chemically stable with the electrodes and possess a TEC compatible with other cell components. [43]

Yttria-stabilized zirconia (YSZ), composed of zirconium dioxide (ZrO_2) fully stabilized with yttria (Y_2O_3) or other dopants like (MgO) and (Sc_2O_3), is the most commonly used electrolyte material for SOFCs. The dopants induce oxygen vacancies, which enable oxide-ion conduction. Despite its widespread use, YSZ is chemically instable at operational temperatures when combined with common cathode materials like LSCF. This interaction leads to the formation of insulating phases such as $SrZrO_3$ and $La_2Zr_2O_7$, which degrade cell performance. [44–47]

To address this challenge, ceria-based electrolytes (CeO_2), doped with gadolinium ions ($Gd_3{}^+$), have been proposed as alternatives due to their superior ionic conductivity and TEC compatibility with other cell components. However, at operational temperatures, $Ce_4{}^+$ ions in ceria may reduce to $Ce_3{}^+$ ions at the anode, resulting in an electronic conductivity and short-circuiting, which compromises cell performance [48–50].

Recently, magnesium-doped lanthanum gallate (LSGM:$La_xSr_{1-x}Ga_yMg_{1-y}O_{3-\delta}$) has shown promise as an electrolyte material for intermediate-temperature SOFCs. LSGM exhibits excellent ionic conductivity, attributed to the oxygen vacancies in the perovskite structure of lanthanum gallate ($LaGaO_3$) doped with strontium and magnesium. Additionally, LSGM demonstrates a TEC compatible with other SOFC components, making it an attractive alternative for intermediate temperature applications [51].

Anode: The primary function of the anode material in an SOFC is to catalyze fuel oxidation and facilitate the conduction of electrons generated during the oxidation process to the external circuit [52]. Therefore, an ideal anode material should possess high catalytic activity for fuel oxidation, excellent electronic conductivity to transport electrons and sufficient ionic conductivity for conducting oxide-ions [53, 54].

Nickel is widely recognized as an effective anode material due to its economic viability, high electronic conductivity and catalytic activity for hydrogen oxidation. However, its high TEC makes it mechanically incompatible with common electrolytes like YSZ. To address this, nickel is typically dispersed over yttria-stabilized zirconia (YSZ), forming nickel–YSZ (Ni–YSZ), the most commonly used anode material [55]. Recent studies have also highlighted nickel doped with gadolinia (Ni–CGO) as a promising alternative, particularly for intermediate-temperature SOFC applications [56].

Ni-YSZ electrodes typically face challenges like sulphur poisoning and carbon deposition, which adversely impacts electrochemical performance. Nevertheless, Ni–YSZ is the state-of-the-art anode for high-temperature SOFCs because of its excellent electrochemical activity and mechanical stability. For intermediate-temperature SOFCs, Ni–CGO is an

optimal choice due to its lower carbon deposition but is mechanically less robust compared to Ni–YSZ [57]. While the anode plays a crucial role in SOFC operation, its role in determining overall cell performance is generally less significant compared to the cathode and electrolyte.

Interconnect: Interconnects provide electrical contacting between cells, along with their role of separating fuel from air. Typically, an interconnect contains excellent oxidation resistance, electrical conductivity, good thermal conductivity and compatible TEC with other cell components.

Metallic interconnects may form a layer of alumina (Al_2O_3) or chromia (Cr_2O_3) to provide oxidation resistance under operating conditions. Cr-based oxide alloys like Ducrolloy ($Cr_5Fe_1Y_2O_3$) operate at high temperatures. Moreover, it shows good oxidation resistance and has a comparable TEC with other SOFC components. However, excessive of chromia scales results in high area specific resistance (ASR) which limit its use. Alternatively, Fe-Cr-based alloys exhibit higher ductility and lower cost as compared to Cr-based alloys. Fe-Cr-based alloy like ferritic stainless steel, with an optimum Cr-content of 17%-25%, shows good oxidation resistance and electrical conductivity. Lastly, they have a compatible TEC as other SOC components making them a good choice for SOFC interconnects. Furthermore, Ni-Cr-based alloys exhibit excellent oxidation resistance and electrical conductive oxide scales, but are limited for application, due to their high TEC compared to other cell materials. One exception is Haynes242, which has a TEC that matches well with LSM and Ni-YSZ electrodes. Moreover, the formation of a fast-growing nickel oxide layer (NiO) is effective against Cr migration.

Cr-containing alloys show two limitations which are, Cr_2O_3-scale growth which increases resistance and evaporation of Cr from interconnects causing poisoning of the cathode. Both these limitations must be considered while considering Cr-based alloys as interconnects. [58–60].

2.1.3 Types of SOC designs

Over the recent years, two types of SOC designs have been widely developed, which are planar and tubular designs [61].

Planar design: These are the most widely manufactured SOFC design due to their planar structure which provides robust manufacturing capabilities. The planar design may be subdivided into:

- Self-supported
- External supported

In the self supported design, the cathode, anode or the electrolyte may be used as the supporting layer and is generally thicker compared to the other layers to provide mechanical stability for the cell. In the external supported SOFC design, a thick porous substrate or metal may be used as support [62]. A schematic of the aforementioned designs are shown in Figure 2.2

Based on certain observations made in recent works for self supported cells, the overall performance may generally be improved by reducing the thickness of the support. The performance of an electrolyte-supported SOFC is most sensitive to the thickness of the electrolyte as it has higher attenuation to ions passing through it. Whereas, for the designs with thicker electrodes, the difficulty lies in the passage of fuel or oxidizer which results in loss of performance. As electrode supported cells have thin electrolytes, the ohmic losses are significantly reduced and the operational temperatures may be lowered which increases the lifetime of the stack [63, 64].

Externally supported cells have benefits in terms of mechanical strength, along with excellent electrical conductivity and high thermal conductivity which causes faster start-up time of cell. For a metal supported cell, the thermal expansion coefficients of the metallic support match closely with other fuel cell materials like YSZ, Ni-YSZ etc. which is beneficial against the effects associated with thermal cycling.

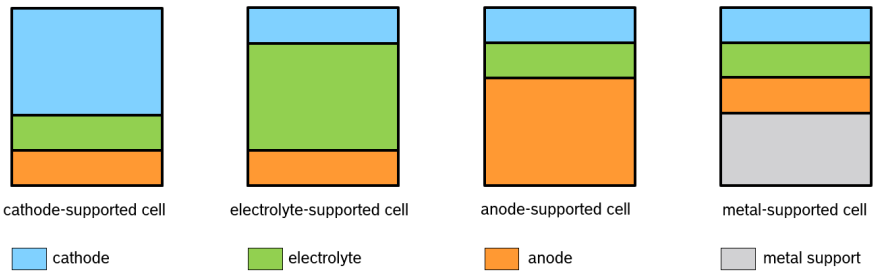

Figure 2.2: Schematic illustrating common types of planar SOFC designs (sketches are not to scale)

Tubular design: The tubular designed SOFCs are known to enhance the volumetric power densities compared to its planar counterpart. Like the self-supported planar design,

the tubular design also has cathode-, anode- and electrolyte-supported configurations of SOFCs. For the tubular design, the volumetric power density is dependent on the cell diameter, which is reduced to enhance performance. However, this also depends on the compatibility with the overall robustness of the supporting material. The anode-supported cell is the most widely used variant for tubular SOFCs due to the difficulty in manufacturing electrolyte- and cathode- supported cells. Moreover, anode materials are generally cheaper than cathode, therefore, the anode-supported design is an attractive choice in terms of manufacturing cost. The tubular design was first invented by Siemens-Westinghouse SOFC company which was a cathode supported design on 1.8 m long tubes of about 2 cm in diameter [65–68].

2.1.4 Current-voltage characteristics

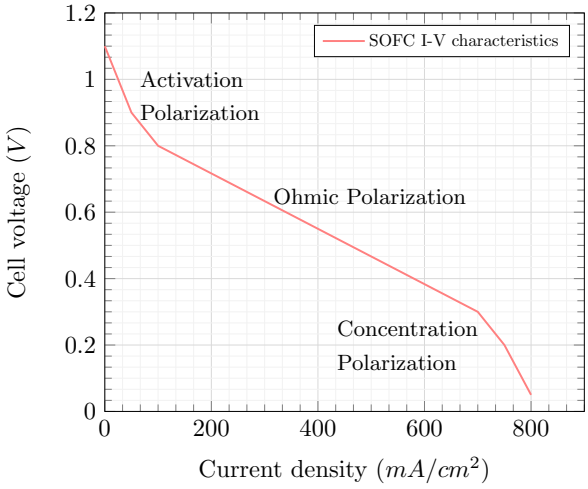

Figure 2.3: I-V characteristics for a SOFC

An ideal SOFC, in theory may be modeled to be a constant voltage source which is not the case based on the I-V characteristics of real SOFCs. The open circuit voltage (OCV) of a single cell is typically in the range of 1-1.2 V, however, when connected to an external circuit, this value drops sharply. Figure 2.3 shows the I-V curves for a cell in practice, wherein, it may be seen that the current density increases as the voltage drops almost linearly. This behavior attributes to the internal resistances caused by various components of the cell and may be referred to as *Ohmic Polarization*. However, at lower and higher

current values, other losses become more significant. At lower currents, the activity of chemical reactions are slower, limiting the electrical output. This form of loss is referred to as *Activation Polarization*. Conversely, at high current values, a reduction in the efficiency of gas exchange leads to a drop in voltage, which occurs primarily due to increasing presence of by-products like water. This form of loss is referred to as *Concentration Polarization*.

The overall performance of the SOFC depends on these losses. Therefore, during application, the electrical loading densities should be chosen to operate the cell in the optimal range of current densities.

2.1.5 Design of solid oxide cell repeat unit

A schematic of a solid oxide cell (SOC), adapted from the design of Ceres Power Limited [69–71] is shown in Figure 2.4, which illustrates the key components of this SOC system. These components include the metallic interconnect, substrate, anode-cathode-electrolyte layers (collectively referred to as the cell) and fuel gaskets. In a typical stack with such kind of design, fuel is introduced through one of the fuel ports and exits through the other, ensuring a steady-state fuel flow within the gas-tight channel formed between the interconnect and substrate across the active area. The metallic substrate plate contains holes that allow fuel to reach the anode, where the electrochemical reaction occurs. The stack is generally exposed to air, enabling a second electrochemical reaction at the cathode. To ensure smooth operation and prevent leakage, air-tight gaskets seal the fuel ports, separating the fuel from air [72].

For the functionality of the cell, the electrochemical reaction at the cathode generates oxygen ions due to the supply of electrons through the metallic interconnect. The oxygen ions are transported through the solid-state electrolyte onto the anode, where they react with the oxidized hydrogen to form water, while the free electrons are transported through an external circuit onto the cathode, generating electricity. The electrons are collected by the cathode bulk at each repeat unit through the metallic interconnect, which causes the reduction of oxygen from the atmosphere [73–76].

The metallic interconnect is the component of primary interest for this work and has two critical roles. Firstly, it forms a compartment that separates the air from fuel, with its design optimized to ensure uniform fuel distribution across the active area. Secondly, it establishes electrical contacts with the cathode bulk by locally supplying electrons to

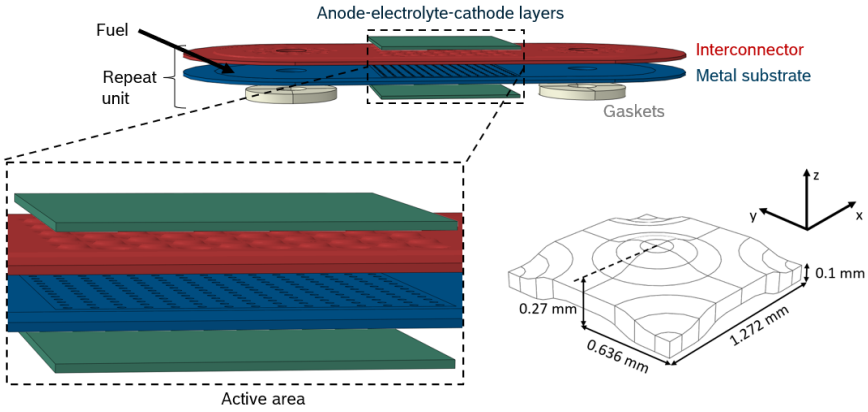

Figure 2.4: Schematic of a standard repeating fuel cell unit and definition of the representative volume element.

the cathode from the external circuit [77–80]. Uniform contacting in the active area is considered as one of the critical features of the interconnect for the SOC stacking system [81]. This is because, during operation, free electrons for the reduction reaction at the cathode are supplied by the interconnect. Due to the high in-plane resistivity of the cathode bulk, these electrons must be supplied locally across the active area by the interconnect, therefore it is important to have good contacting in all regions of the active area to avoid excessive ohmic losses [82, 83].

Given the overview of SOC components and their functionalities, it is common to use finite element methods to evaluate mechanical robustness of the stack from an engineering perspective [84–86]. Here, the focus is to gain insights into the contacting configuration and the distribution of contact pressure across the active area of the stack. Therefore, a detailed discussion on the fundamentals of continuum mechanics, which is necessary to model materials in the finite element framework, is carried out in the next section.

2.2 Fundamentals of continuum mechanics

This section briefly gives an overview on general concepts of continuum mechanics which is essential for building up a constitutive material model. This section refers to the

following literature which provide a fundamental background of continuum mechanics [87–92]. First, we start by deriving stress and strain from basic principles of motion in the next subsection.

2.2.1 Kinematics

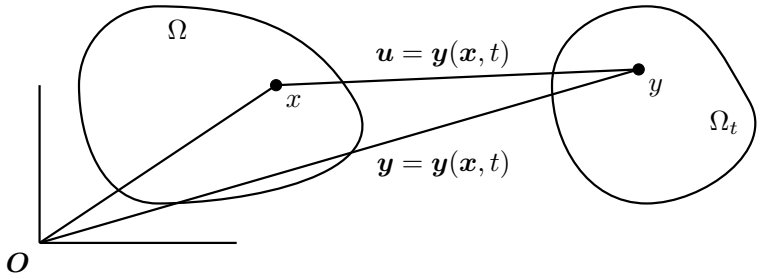

Figure 2.5: Undeformed and deformed configuration of an arbitrary material

Consider a body in Figure 2.5 in its undeformed state occupying a region Ω in 3-D space $\mathbb{R}^3$ located at position $\boldsymbol{x}$ from the origin $\boldsymbol{O}$. At time t, the body occupies a new configuration Ω_t under the influence of *motion*, which can be expressed mathematically using a vector valued function $\boldsymbol{y} = \boldsymbol{y}(\boldsymbol{x}, t)$. The resulting *displacement* from initial to final configuration may be represented as,

$$\boldsymbol{u}(\boldsymbol{x}, t) = \boldsymbol{y}(\boldsymbol{x}, t) - \boldsymbol{x} \tag{2.2.1}$$

Now, let us consider two material points in Ω with reference to position $\boldsymbol{x}$ by defining vectors $\boldsymbol{\Delta x}$ and $\boldsymbol{\delta x}$, as shown in Figure 2.6. In the deformed configuration, $\Delta \boldsymbol{x}$ is mapped onto $\boldsymbol{\Delta y}$ such that, $\boldsymbol{y} = \boldsymbol{\Delta y}(\boldsymbol{x} + \boldsymbol{\Delta x}) - \boldsymbol{y}(\boldsymbol{x})$. Similarly, $\boldsymbol{\delta x}$ corresponds to $\boldsymbol{\delta y}$ such that, $\boldsymbol{\delta y} = \boldsymbol{y}(\boldsymbol{x} + \boldsymbol{\delta x}) - \boldsymbol{y}(\boldsymbol{x})$, which can be expressed using Taylor's expansion as,

$$\begin{aligned} \boldsymbol{\Delta y} &= \boldsymbol{\Delta x} + \boldsymbol{\nabla u \Delta x} + \boldsymbol{o}(|\boldsymbol{\Delta x}|) \\ \boldsymbol{\delta y} &= \boldsymbol{\delta x} + \boldsymbol{\nabla u \delta x} + \boldsymbol{o}(|\boldsymbol{\delta x}|) \end{aligned} \tag{2.2.2}$$

where $\boldsymbol{o}(|\boldsymbol{\delta x}|)$ and $\boldsymbol{o}(|\boldsymbol{\Delta x}|)$ are higher order terms. On considering the difference of the product of these material points in the deformed and undeformed states,

$$\boldsymbol{\Delta y}.\boldsymbol{\delta y} - \boldsymbol{\Delta x}.\boldsymbol{\delta x} = (\boldsymbol{\nabla u \Delta x}).\boldsymbol{\delta x} + (\boldsymbol{\nabla u \delta x}).\boldsymbol{\Delta x} + (\boldsymbol{\nabla u \Delta x}).(\boldsymbol{\nabla u \delta x}) + \boldsymbol{o}(|\boldsymbol{\delta x}|^2 + |\boldsymbol{\Delta x}|^2) \tag{2.2.3}$$

Upon simplifying the above expression, we get the definition of strain in terms of the displacement field which may be defined as,

$$\boldsymbol{\varepsilon}(\boldsymbol{u}) = \frac{1}{2}[\boldsymbol{\nabla u} + (\boldsymbol{\nabla u})^T + (\boldsymbol{\nabla u})^T.\boldsymbol{\nabla u}] \tag{2.2.4}$$

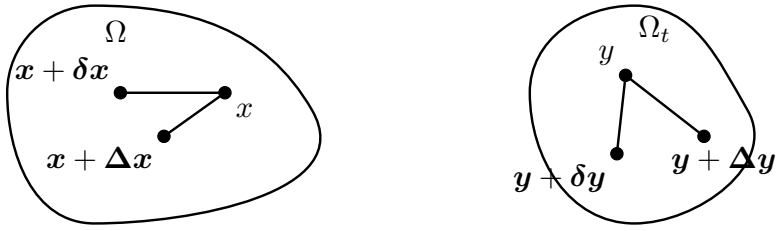

Figure 2.6: Undeformed and deformed configuration of the material body for the definition of strain

In the context of small strains, the higher order term $(\boldsymbol{\nabla u})^T.\boldsymbol{\nabla u}$ may be neglected and Equation 2.2.4 takes the form,

$$\boldsymbol{\varepsilon}(\boldsymbol{u}) = \frac{1}{2}[\boldsymbol{\nabla u} + (\boldsymbol{\nabla u})^T] \tag{2.2.5}$$

Along with strain, an accompanied volume change ΔV is associated for any material. The volume change between the undeformed state Ω and deformed state Ω_t may be expressed as,

$$\Delta V = V_t - V = \int_\Omega (J(x) - 1)dx \tag{2.2.6}$$

where, J may be defined as the *Jacobian*. On considering infinitesimal deformation, the change in volume takes the form,

$$\Delta V = \int_\Omega div\boldsymbol{u}dx \tag{2.2.7}$$

2.2.2 Cauchy's Stress Theorem

Consider a part Ω' as a subset of body Ω and is bounded by a surface $\partial\Omega'$, as illustrated in Figure 2.7. In the deformed configuration of this body, we introduce the *stress vector* $\boldsymbol{t}$ which acts on an infinitesimal surface element da of $\partial\Omega'$. This stress vector $\boldsymbol{t}$ represents the force exerted by the surrounding material of the body Ω onto the portion Ω'. According to the Cauchy stress theorem, the stress vector $\boldsymbol{t}$ at any point on the surface $\partial\Omega'$

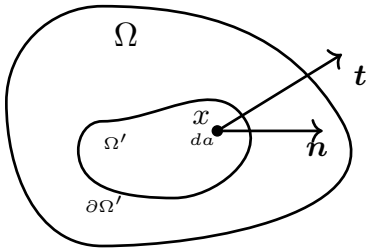

Figure 2.7: Continuum material experiencing a body force in the form of traction $\boldsymbol{t}$ on infinitesimal surface area da

depends linearly on the outward unit normal vector $\boldsymbol{n}$ to the surface, which is given by:

$$\boldsymbol{t} = \boldsymbol{\sigma}(\boldsymbol{x}, t).\boldsymbol{n} \tag{2.2.8}$$

where $\boldsymbol{\sigma}$ is the Cauchy stress tensor that characterizes the internal forces within the material [93, 94].

2.2.3 Thermodynamic considerations

Having defined strain and stress from the fundamental principles of motion and displacement, we can now proceed to derive the balance laws of thermodynamics. These balance laws provide a foundation for the dissipation inequality, which is essential for formulating elastoplastic theories of materials. This framework allows the derivation of constitutive models within the thermodynamic framework, which can be used to model complex material behavior. [95–102].

Balance of mass: We begin with the balance of mass, which states that the total mass of a portion of closed system Ω' with volume V remains constant over time t. This principle ensures that mass is conserved throughout any physical process, which forms a fundamental aspect of continuum mechanics and thermodynamics. It can be expressed as,

$$\frac{d}{dt}\int_{\Omega'_t} \rho_t dV_t = \frac{d}{dt}\int_{\Omega'} J\rho dV = 0 \tag{2.2.9}$$

where ρ is the density, J is the Jacobian defined in the previous section.

Balance of linear momentum: The balance of linear momentum states that the time rate of change of the linear momentum of the volume Ω' is equal to the sum of the external forces acting on the body. This principle reflects Newton's second law and is fundamental

in describing the motion and deformation of continuous bodies under the influence of external forces. It can be expressed as,

$$\frac{d}{dt}\int_{\Omega'}\rho\dot{\boldsymbol{u}}dV = \frac{d}{dt}\int_{\Omega'}\boldsymbol{b}dV + \frac{d}{dt}\int_{\partial\Omega'}\boldsymbol{t}ds \tag{2.2.10}$$

where ρ is the density, $\dot{\boldsymbol{u}}$ is the velocity, $\boldsymbol{b}$ represents body forces, and $\boldsymbol{t}$ denotes surface tractions. This balance of linear momentum can be reduced to a differential form using the divergence theorem and assuming that the integrals hold for any arbitrary volume Ω'. The resulting equation is:

$$div\boldsymbol{\sigma} + \boldsymbol{b} = \rho\dot{\boldsymbol{u}} \tag{2.2.11}$$

Balance of angular momentum: The balance of angular momentum states that the time derivative of the moment of linear momentum of Ω' must be equal to the sum of the moments of the forces acting on the body with respect to the same point. Without loss of generality of Equation 2.2.10, upon taking the moment with respect to the origin with $\boldsymbol{x}$ representing the position vector, and the equation may be expressed as:

$$\frac{d}{dt}\int_{\Omega'}\boldsymbol{x}\times\rho\dot{\boldsymbol{u}}dV = \frac{d}{dt}\int_{\Omega'}\boldsymbol{x}\times\boldsymbol{b}dV + \frac{d}{dt}\int_{\partial\Omega'}\boldsymbol{x}\times\boldsymbol{t}ds \tag{2.2.12}$$

which results in the conclusion that the Cauchy stress tensor must be symmetric. For angular momentum to be conserved, the internal moments generated by stress must balance out taking the form:

$$\boldsymbol{\sigma} = \boldsymbol{\sigma}^T \tag{2.2.13}$$

Balance of energy: The first law of thermodynamics, or the energy balance law, can be expressed for any volume Ω' of the body Ω, bounded by surface $\partial\Omega'$ and states that the time rate of change of internal energy and kinetic energy within Ω' is equal to the sum of the rate of mechanical work done on the part by external forces and the heat supplied to Ω'. In mathematical form, this can be written as:

$$\frac{d}{dt}\int_{\Omega'}(e+\frac{1}{2}\rho\dot{\boldsymbol{u}}^2)dV = \int_{\Omega'}\boldsymbol{b}.\dot{\boldsymbol{u}}dV + \int_{\partial\Omega'}\boldsymbol{t}.\dot{\boldsymbol{u}}ds + \int_{\Omega'}rdV - \int_{\partial\Omega'}\boldsymbol{q}.\boldsymbol{n}ds \tag{2.2.14}$$

where, ρ is the mass density, e is the internal energy, $\dot{\boldsymbol{u}}$ is the velocity, $\boldsymbol{t}$ is the traction vector, $\boldsymbol{q}$ is the heat flux across the surface $\partial\Omega'$, r is the heat supply per unit volume. On simplifying Equation 2.2.14 by incorporating the definition of stress and using the balance of linear momentum, we arrive at a more compact form of the energy balance.

$$\dot{e} = \boldsymbol{\sigma} : \dot{\boldsymbol{\varepsilon}} + r - div\boldsymbol{q} \tag{2.2.15}$$

Balance of entropy: For a body with entropy η and temperature greater than absolute zero $T > 0$, the second law of thermodynamics states that the rate of change of entropy

in the body in not less then the total entropy supplied to the body through heat. This may be mathematically formulated as:

$$\frac{d}{dt}\int_{\Omega'} \eta dV \geq \int_{\Omega'} T^{-1} r dV - \int_{\partial\Omega'} T^{-1}\boldsymbol{q}.\boldsymbol{n} ds \tag{2.2.16}$$

On simplifying Equation 2.2.16, we can express it in the form,

$$\dot{\eta} \geq -div(T^{-1}\boldsymbol{q}) + T^{-1} r \tag{2.2.17}$$

Also known as the *Clausius Duhem* form of the second law of thermodynamics.

In elasticity and elastoplastic theories, it is customary to work with the *Helmholtz free energy* ψ instead of internal energy which is defined as $\psi = e - \eta T$. Upon substituting this into Equation 2.2.15 and Equation 2.2.17 we get,

$$\dot{\psi} + \eta\dot{T} - \boldsymbol{\sigma} : \dot{\boldsymbol{\varepsilon}} + T^{-1}\boldsymbol{q}.\nabla T \leq 0 \tag{2.2.18}$$

which is called the *local dissipation inequality*. To generalize this relation to a purely mechanical setting, we assume isothermal conditions along with no heat flow within the body and no heat supply from outside. And Equation 2.2.18 reduces to the form,

$$\boldsymbol{\sigma} : \dot{\boldsymbol{\varepsilon}} - \dot{\psi} \geq 0 \tag{2.2.19}$$

which motivates the definition of stress in the thermodynamic setting as

$$\boldsymbol{\sigma} = \frac{\partial \psi}{\partial \boldsymbol{\varepsilon}^e} \qquad \text{with} \qquad \left(\frac{\partial \psi}{\partial \boldsymbol{\varepsilon}^e} - \boldsymbol{\sigma}\right) : \dot{\boldsymbol{\varepsilon}} \geq 0 \tag{2.2.20}$$

The *linearly elastic material* is recovered assuming that the elastic part of the free energy $\psi(\boldsymbol{\varepsilon}^e)$ is a quadratic function of strain in the form,

$$\psi(\boldsymbol{\varepsilon}^e) = \frac{1}{2}\boldsymbol{\varepsilon}^e : \mathbf{C} : \boldsymbol{\varepsilon}^e \tag{2.2.21}$$

where, $\mathbf{C}$ is the elasticity tensor with major and minor symmetries of the form $\mathbb{C}_{ijkl} = \mathbb{C}_{klij} = \mathbb{C}_{jikl} = \mathbb{C}_{ijlk}$ and $\boldsymbol{\varepsilon}^e$ is the elastic component of strain. Upon decomposing the total strain rate $\dot{\boldsymbol{\varepsilon}}$ into its kinematic constituents and substituting them into Equation 2.2.19, the sum of dissipative components such as inelastic strains $\boldsymbol{\varepsilon^{ie}}$ may be expressed in the form of the *reduced dissipation inequality*.

$$\boldsymbol{\sigma} : \dot{\boldsymbol{\varepsilon}}^{\boldsymbol{ie}} \geq 0 \tag{2.2.22}$$

The condition given in Equation 2.2.22 must be fulfilled for all loading cases.

2.2.4 Theory of plasticity

For the small strains in plasticity theory, the total strain in a body is usually decomposed into a recoverable elastic strain $\boldsymbol{\varepsilon}^{el}$ and a dissipative plastic strain $\boldsymbol{\varepsilon}^{p}$, which is written in the form,

$$\boldsymbol{\varepsilon} = \boldsymbol{\varepsilon}^{el} + \boldsymbol{\varepsilon}^{pl} \tag{2.2.23}$$

As an immediate consequence of solving the local dissipation inequality in Equation 2.2.19, we see that, the elastic strain tensor is related to the Cauchy stress tensor,

$$\boldsymbol{\sigma} = \mathbb{C} : \boldsymbol{\varepsilon}^{el} \tag{2.2.24}$$

On considering plasticity, the allowable permissible stress is restricted to a domain $\mathcal{S}$ which can be defined using a yield function $\phi(\boldsymbol{\sigma})$,

$$\mathcal{S} = \{\boldsymbol{\sigma} \mid \phi(\boldsymbol{\sigma}) \leq 0\} \tag{2.2.25}$$

where, the yield function forms the boundary of domain $\mathcal{S}$ called the yield surface. We can also define an elastic domain $\mathcal{E}$ as a subset of $\mathcal{S}$, where the material exhibits elastic behavior,

$$\mathcal{E} = \{\boldsymbol{\sigma} \mid \phi(\boldsymbol{\sigma}) < 0\} \tag{2.2.26}$$

With the definition of the elastic domain $\mathcal{E}$, the onset of plasticity occurs when the stress is on the yield surface $\phi(\boldsymbol{\sigma}) = 0$, rendering the condition $\phi(\boldsymbol{\sigma}) > 0$ as not permissible. The theory of maximum plastic work, is a commonly used postulate in plasticity theory which infers that the domain $\mathcal{S}$ is convex. Moreover, it also infers that the evolution of stress is always normal to the yield surface. Upon defining the conditions for plastic strain to occur, it is necessary to define evolution equations for plastic flow also known as the flow rule.

$$\dot{\boldsymbol{\varepsilon}}^{\boldsymbol{pl}} = \dot{\varepsilon}^{pl}\boldsymbol{N} \qquad \text{with} \qquad \boldsymbol{N} = \frac{\partial \phi}{\partial \boldsymbol{\sigma}} \tag{2.2.27}$$

where $\dot{\varepsilon}^{pl}$ is defined as the plastic strain rate multiplier and $\boldsymbol{N}$ is called the flow direction. Having a non-zero plastic multiplier ($\dot{\varepsilon}^{pl} > 0$) implies that the stress is on the yield surface ($\phi(\boldsymbol{\sigma}) = 0$) and vice versa. This gives rise to complementary condition called the consistency condition: $\phi\dot{\varepsilon}^{pl} = 0$. Together these are called the *Kuhn-Tucker* conditions and can be summarized as,

$$\phi \geq 0, \qquad \dot{\varepsilon}^{pl} \geq 0 \qquad \text{and} \qquad \phi\dot{\varepsilon}^{pl} = 0 \tag{2.2.28}$$

It is usually common to assume a yield function $\phi(\boldsymbol{\sigma})$ based on the requirements of the model. A widely used yield function is the *von Mises* yield criteria which is based on the

assumption that the threshold of elastic behavior is determined by elastic shear density and is expressed as:

$$\phi(\boldsymbol{\sigma}) = \sqrt{(\sigma_{11}-\sigma_{22})^2+(\sigma_{22}-\sigma_{33})^2+(\sigma_{11}-\sigma_{33})^2+6\sigma_{12}^2+6\sigma_{23}^2+6\sigma_{31}^2} \tag{2.2.29}$$

with its tensorial form,

$$\phi(\sigma) = \sqrt{\frac{1}{2}\boldsymbol{\sigma} : \mathbb{P} : \boldsymbol{\sigma}} \tag{2.2.30}$$

where $\mathbb{P}$ is a fourth order deviatoric projection tensor of the form $\mathbb{P} = \mathbb{I} - \frac{1}{3}\mathbf{1}\otimes\mathbf{1}$ where $\mathbb{I}_{ijkl} = \frac{1}{2}(\delta_{ik}\delta_{jl}+\delta_{jk}\delta_{il})$. For anisotropic plasticity, $\mathbb{P}$ is replaced with a Hill-type tensor $\mathbb{M}$ which modifies this yield criteria and defines an anisotropic yielding structure. The *von Mises* yield criteria considers no accompanied volume change during plastic deformation which is observed in metal plasticity [103–107].

With this the fundamental framework of the constitutive theory of plasticity is complete. These fundamentals will be used in Chapter 5 to develop a constitutive material model for the current work.

2.2.5 Computational Homogenization

In this subsection, fundamentals of computational homogenization which is a technique for model reduction, is discussed referring to the following literature [108–112].

Scale separation:

A medium may be defined by a periodically repeating unit volume that is representative of the bulk volume. If the dimensions of the periodic unit volume are small enough compared to the dimensions of the macroscopic bulk volume, then a separation of scales may be assumed by considering two scales expressed as:

- The macroscopic scale defined by macroscopic or global coordinates denoted by $\bar{\boldsymbol{x}}$.
- The microscopic scale defined by the microscopic or local coordinates denoted by $\boldsymbol{x}$.

The separation of scales ($\bar{\boldsymbol{x}} >> \boldsymbol{x}$) assumes the microscopic representative unit volume as a macroscopic material point. Thus, at the macroscale, the heterogeneous, complex geometric structure of the microscopic unit volume may be represented by a simpler, homogenous structure, which has an averaged equivalent material response.

Connection between scales:

For linking the micro- and macro-scale equations, a connection between scales must be established over time t. To achieve this, computational homogenization suggests the volume averaging of the microscopic stress $\boldsymbol{\sigma}$ and strain $\boldsymbol{\varepsilon}$ fields to obtain their macroscopic counterparts ($\bar{\boldsymbol{\sigma}}$ and $\bar{\boldsymbol{\varepsilon}}$). Moreover, it may be shown using the divergence theorem that the stress and strain averages within a unit cell comprised of volume V are connected to the traction and displacement vectors applied at their boundaries ∂V:

$$\bar{\boldsymbol{\sigma}}(\bar{\boldsymbol{x}}, t) = \frac{1}{V}\int_V \boldsymbol{\sigma}(\bar{\boldsymbol{x}}, \boldsymbol{x}, t)\, dV = \frac{1}{V}\int_{\partial V} \boldsymbol{\sigma}(\bar{\boldsymbol{x}}, \boldsymbol{x}, t).\boldsymbol{n}(\boldsymbol{x}) \otimes \boldsymbol{x}\, dS \tag{2.2.31}$$

$$\bar{\boldsymbol{\varepsilon}}(\bar{\boldsymbol{x}}, t) = \frac{1}{V}\int_V \boldsymbol{\varepsilon}(\bar{\boldsymbol{x}}, \boldsymbol{x}, t)\, dV = \frac{1}{V}\int_{\partial V} \left(\boldsymbol{u}(\bar{\boldsymbol{x}}, \boldsymbol{x}, t) \otimes \boldsymbol{n}(\boldsymbol{x}) + \boldsymbol{n}(\boldsymbol{x}) \otimes \boldsymbol{u}(\bar{\boldsymbol{x}}, \boldsymbol{x}, t)\right)\, dS \tag{2.2.32}$$

where $\boldsymbol{n}$ is the outward normal at each point on the boundary of the unit cell ($\forall \boldsymbol{x} \in \partial V$).

Periodicity:

When assuming periodicity within a unit cell for a strain driven problem, it is implied that the displacement vector $\boldsymbol{u}$ for a microscopic material point denoted by $Q(\bar{\boldsymbol{x}}, \boldsymbol{x})$ may be expressed additively as,

$$\boldsymbol{u}(\bar{\boldsymbol{x}}, \boldsymbol{x}, t) = \bar{\boldsymbol{\varepsilon}}(\bar{\boldsymbol{x}}, t).\boldsymbol{x} + \boldsymbol{u'}(\bar{\boldsymbol{x}}, \boldsymbol{x}, t) + \boldsymbol{u_0}(\bar{\boldsymbol{x}}, t) \tag{2.2.33}$$

In Figure 2.8, the affine part of the local displacement is related to the macroscopic strain

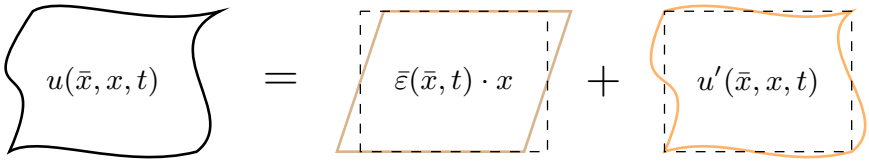

Figure 2.8: Displacement field as a sum of an affine and periodic fluctuation

$\bar{\boldsymbol{\varepsilon}}$ and the periodic fluctuations within the unit cell are given by $\boldsymbol{u'}$. The last term in Equation 2.2.33, denoted by $\boldsymbol{u_0}$ represents the rigid body motion as a consequence of the microscopic problem which is reflected in the macroscopic problem.

The periodic fluctuations $\boldsymbol{u'}$ have the same magnitude on opposite boundaries of the unit cell denoted by $\boldsymbol{x_{+ve}}$ and $\boldsymbol{x_{-ve}}$ and may be expressed as,

$$\boldsymbol{u'}(\bar{\boldsymbol{x}}, \boldsymbol{x_{-ve}}, t) = \boldsymbol{u'}(\bar{\boldsymbol{x}}, \boldsymbol{x_{+ve}}, t) \qquad \text{with} \qquad (\boldsymbol{x_{-ve}}, \boldsymbol{x_{+ve}} \in \partial V) \tag{2.2.34}$$

On substituting Equation 2.2.33 in Equation 2.2.34,

$$\boldsymbol{u'}(\bar{\boldsymbol{x}}, \boldsymbol{x_{-ve}}, t) - \boldsymbol{u'}(\bar{\boldsymbol{x}}, \boldsymbol{x_{+ve}}, t) = \bar{\boldsymbol{\varepsilon}}(\bar{\boldsymbol{x}}, t).(\boldsymbol{x_{+ve}} - \boldsymbol{x_{-ve}}) \tag{2.2.35}$$

The local microscopic strain field under the periodicity assumption may be expressed as,

$$\boldsymbol{\varepsilon}(\bar{\boldsymbol{x}}, \boldsymbol{x}, t) = \bar{\boldsymbol{\varepsilon}}(\bar{\boldsymbol{x}}, t) + \boldsymbol{\varepsilon'}(\bar{\boldsymbol{x}}, \boldsymbol{x}, t) \tag{2.2.36}$$

where,

$$\boldsymbol{\varepsilon'}(\bar{\boldsymbol{x}}, \boldsymbol{x}, t) = \frac{1}{2}\left(\nabla_{\boldsymbol{x}}\boldsymbol{u'}(\bar{\boldsymbol{x}}, \boldsymbol{x}, t) + (\nabla_{\boldsymbol{x}}\boldsymbol{u'}(\bar{\boldsymbol{x}}, \boldsymbol{x}, t))^T\right) \tag{2.2.37}$$

and $\boldsymbol{\varepsilon'}$ is the local microscopic strain induced by period fluctuation $\boldsymbol{u'}$, which implies,

$$\frac{1}{V}\int_V \boldsymbol{\varepsilon'}(\bar{\boldsymbol{x}}, \boldsymbol{x}, t)\, dV = \frac{1}{2V}\int_{\partial V} (\boldsymbol{u'}(\bar{\boldsymbol{x}}, \boldsymbol{x}, t) \otimes \boldsymbol{n}(\boldsymbol{x}) + \boldsymbol{n}(\boldsymbol{x}) \otimes \boldsymbol{u'}(\bar{\boldsymbol{x}}, \boldsymbol{x}, t))\, dS = \boldsymbol{0} \tag{2.2.38}$$

to establish a compatibility between Equation 2.2.33 and Equation 2.2.32. With this, Equation 2.2.36 has the physical interpretation that the microscopic strain is equal to the macroscopic strain.

Solution of the microscale problem:

The solution of the microscale constitutive problem defines the macroscopic constitutive behavior of the representative unit volume and consequently, individual material points in the macroscale problem. Conversely, for a loading on any macroscopic material point, the microscopic loading may be determined by resolving the load on the microscopic unit cell problem.

Solution of the macro-scale problem:

The macroscopic problem is treated as a normal mechanical analysis, where every material point in the macroscopic problem may be treated as the equivalent material behavior obtained from the microscopic problem.

2.3 Summary

A brief overview on all the necessary areas addressed and methodologies used for this work is outlined in this chapter. Firstly, a detailed overview of the working principles of the SOC was shown. Alongside, the required components and performance indicators were

reviewed. Lastly, the SOC design relevant for this work was highlighted and the challenge of homogenous contacting problem was introduced.

To address this challenge, finite element method is an efficient tool which is derived from the fundamentals of continuum mechanics. These fundamentals form the basis of building material models which is vital for mechanical simulations. However, based on the current state of the art, large computational times pose a challenge in using these approaches for SOC stack simulations. This is addressed here using computational homogenization. This apporach along with the knowledge from the stated literature is used to synthesize new methods to perform detailed mechanical simulations for SOC stacks with practical computational times.

3 Experimental derivation of material data

In the previous chapter, a schematic layout of the components within an SOC was presented, alongside a discussion of their functionality and general working principles. As outlined in Chapter 1, the objective of this research is to model mechanical contact pressures between repeat units to estimate the area specific resistance (ASR) within a stack during operation. To do so, finite element methods are employed in the current chapter. A finite element model is developed to simulate the components under investigation with an aim of replicating experimental conditions.

The primary focus of this chapter is to perform suitable tests to derive accurate material parameters and then validate the finite element model against experimental results. To achieve this, mechanical compression tests are performed on individual interconnect contacts to evaluate the stiffness behavior of the interconnect and its coating material. The data obtained from these tests motivate further investigation of material data which is then used to construct a finite element model. This model is then validated against experimental results and serves as a foundation for further analysis in subsequent chapters. Additionally, the mechanical stability of the metallic interconnect is evaluated for thermal and rate-dependent boundary conditions to estimate its behavior during operation. The resulting material data is incorporated into the finite element model, making sure that it accurately reflects the specified test conditions.

3.1 Process steps in the life-time of a single SOC contact

This chapter focuses on analyzing individual SOC interconnect contacts. Therefore, it is essential to have an overview on the various loading conditions that a single SOC

contact may encounter during its life-time. These conditions may span from manufacturing to operation and are summarized in three stages, as depicted schematically in Figure 3.1.

Initially, the loading on an SOC contact begins at state 0, as depicted in Figure 3.1(a). During stacking of repeat units, the contacts are mechanically compressed at room temperature, driven by the strain shown in Figure 3.1(a), leading to stress state 1, highlighted in Figure 3.1(c). After mechanical loading, the strain is held constant and the stack undergoes a temperature increase from room temperature to operational temperature as shown in Figure 3.1(b). During this stage, the stress path may be visualized in Figure 3.1(c) which suggests that the contact may initially be within the elastic domain at room temperature, however, significant temperature increase may cause a reduction in the yield limit, leading to onset of plasticity and a consequent decrease in stress to state 2. During operation, viscous effects such as relaxation may further reduce stress state over prolonged time periods. This transition from stress state 2 to stress state 3 is shown schematically in Figure 3.1(c), where it may also be noted that the time scales for this loading step are considerably longer than for mechanical and thermal loadings. The rate of relaxation seen in this loading step is influenced by the stress state at the end of thermal loading at state 2.

These stages summarize the stress states during the loading steps in the life-time of an SOC contact in Figure 3.1(c). They can be classified according to their driving parameters:

- **Assembly at Room Temperature:** The primary driving parameter is strain during mechanical loading from state 0 to state 1.
- **Temperature Ramp-Up:** Temperature acts as a driving parameter causing a change in stress from state 1 to state 2.
- **Operation:** Time acts as the driving parameter, causing a stress relaxation over large time-scales from state 2 to state 3.

This schematic characterizes the influence of different driving parameters on the stress state which will be explored in more detail in the subsequent sections.

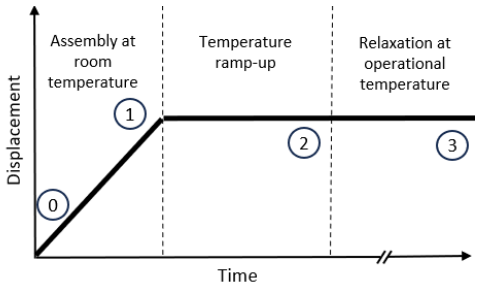

(a) Strain over time

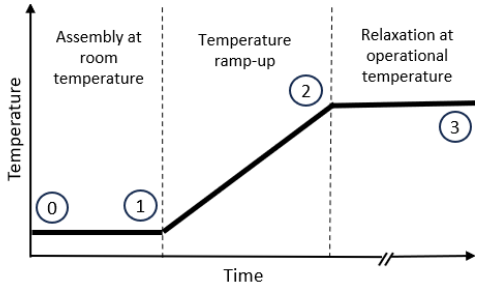

(b) Temperature over time

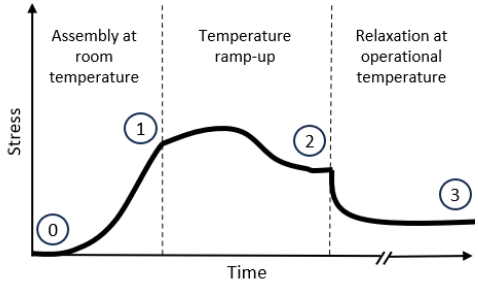

(c) Stress over time

Figure 3.1: Process steps in the life cycle of an SOC contact

3.2 Mechanical compression tests on single contacts

With the overview of the various components and loading conditions on SOC contacts, this section focuses on evaluating the mechanical properties of the interconnect. The interconnect plays a crucial role in the compression system of an SOC stack due to its corrugated geometry and its critical functionality of current collection. Therefore, it is essential to understand the compression behavior of a single interconnect contact. In order to gain a complete understanding of the compression system at the stack level, this section examines the compression behavior of individual interconnect contacts. Due to its periodically repeating structure in the active area, these investigations provide fundamental insights regarding the stack compression behavior as a whole.

A metallic interconnect is typically a corrugated structure produced through sheet metal forming processes and is illustrated in Figure 3.2(a) [113]. These interconnects are generally composed of Crofer 22 APU and consist of several hundred contacts that form the active area of the cell [114,115]. These contacts are usually coated with a material, as shown in Figure 3.2(b), designed to prevent corrosion or reduce contact resistance [116–119]. In this case, the coating is a soft, porous material whose mechanical properties are considered important for the stack compression system.

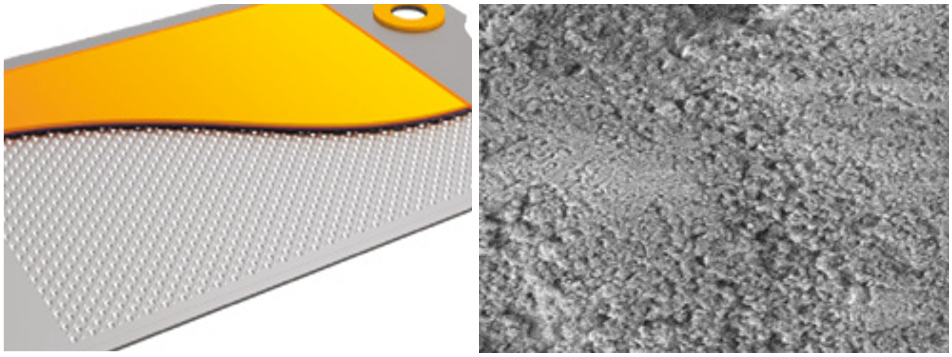

(a) Metallic interconnect (b) Coating

Figure 3.2: Metallic interconnect and coating

Mechanical testing

In order to perform mechanical compression tests on individual contacts, the interconnect is clamped on a test-bench and is compressed at individual contacts using a mechanical

pressing tool. The applied force is gradually increased over the duration of the compression cycle until a target reaction force is reached. The reaction force and displacement of the mechanical press is recorded over time and plotted for each test.

The objective of this test is to characterize the elastoplastic deformation behavior of single interconnect contacts and their coatings. There are two types of samples considered for the tests: *1. Uncoated contacts* and *2. Coated contacts*. After running the compression routine for several samples, the normalized force and normalized deformation responses are recorded from the tests and plotted in Figure 3.3(a) for the uncoated contact and in Figure 3.3(b) for the coated contact.

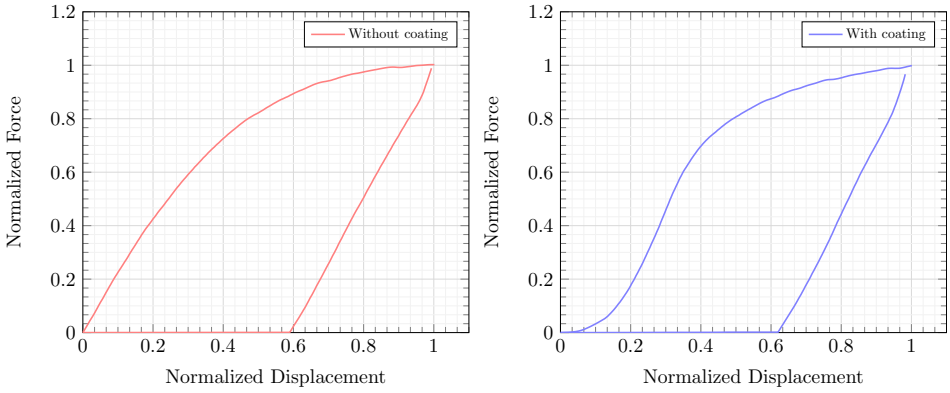

(a) Force-Deformation behavior of a single uncoated interconnect contact

(b) Force-Deformation behavior of a single coated interconnect contact

Figure 3.3: Mechanical compression test for single interconnect contacts

It may be noted that the resulting force-deformation relations obtained from each test was very repeatable and showed negligible variance. Upon comparing the force-deformation relations in Figure 3.3, a typical elastoplastic behavior of the coated and uncoated interconnect contacts are observed.

Moreover, there is a clear distinction observed between the coated and uncoated contacts. Initially, a linear elastic response is observed until a normalized force of 0.6 is reached, beyond which the onset of plasticity is seen. The magnitude of plastic deformation may also be apparent in the unloading curve. Additionally, the coated interconnect contact exhibits an initial non-linear response until a normalized deformation of approximately 0.2 is reached, unlike the uncoated contact. This exponential increase in stiffness may

be attributable to the porous nature of the coating material as its pore-density tends to decrease with applied deformation.

In summary, the mechanical testing characterizes the elastoplastic response of the metallic interconnect and potentially suggests an exponential stiffness behavior for the porous coating. These effects may be distinctly characterized on comparing the force-deformation relations of the uncoated and coated interconnects in Figure 3.3(a) and Figure 3.3(b). Along with the force-deformation relations of the mechanical tests, the 3-D image data of these samples were analyzed before and after the mechanical tests, which is seen in the next subsection.

Verification of image data

In addition to mechanical tests mentioned in the previous subsection, 3-D image data of the contacts were captured before and after the deformation using a high-precision measurement device called ALICONA InfiniteFocus. The images produced spatial data pixels representing the contacts under investigation. This data was post-processed in MATLAB, a commercially available software, to create contours and generate corresponding surface profiles of the contacts. The data was fitted to a second-degree polynomial function which represents the profile of a single contact, as shown in Figure 3.4(a). The residuals from the fit polynomial projects the curved surface of a coated contact as a plane. It represents the deviation of the data pixels from the fitted curve, effectively characterizing the surface roughness of the coating as a plane. The resulting contours are shown in Figure 3.4(b) and Figure 3.4(c).

Upon comparing the contours for a single contact before the test in Figure 3.4(b) and after the tests in Figure 3.4(c), the indented portion of the contact is distinctly visible after indentation. A profile of the coated surfaces before and after the test is shown in Figure 3.4(d). The data indicates that the deformation in the coating is comparable to the initial non-linear deformation recorded during the tests. This suggests that the initial exponential stiffness observed in Figure 3.3(b) is attributable to the deformation of the coating. Furthermore, in Figure 3.4(d) it is observed that for the given compression tests, there is no lateral deformation in the coating profile. This indicates a significant volume change in the deformed state, which is typically compensated by the reduction in pore-density of the coating. However, due to significant surface roughness and localized unevenness seen in Figure 3.4(d), a detailed evaluation of the effective coating stiffness is required and is carried out in the next section.

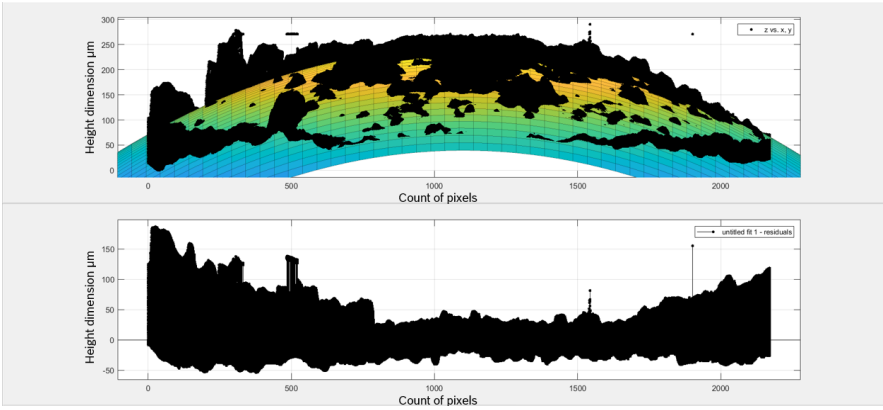

(a) Postprocessing of image data: curve-fitting and generating residuals

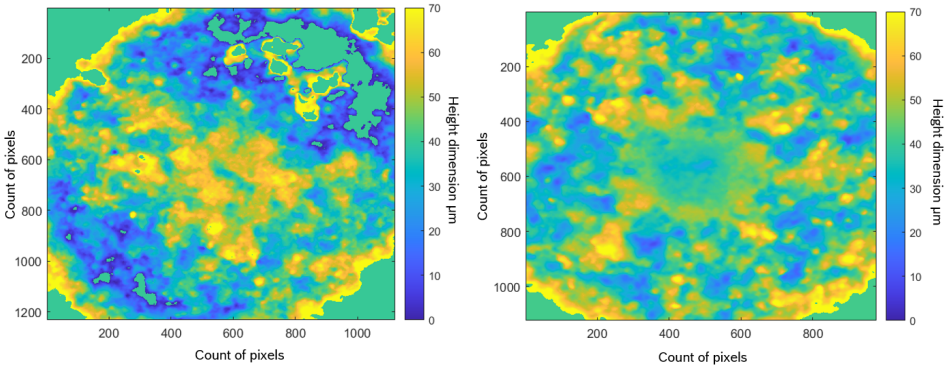

(b) Profile of the coated interconnect contact before test

(c) Profile of the coated interconnect contact after test

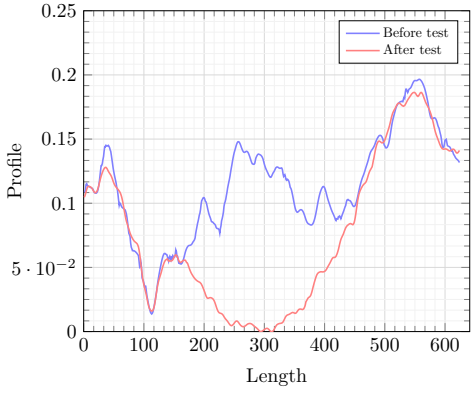

(d) Comparison of surface data before and after compression

Figure 3.4: Analysis of image data before and after compression tests

3.3 Evaluation of mechanical behavior of the porous coating

Upon analysis of image data from the previous section, it is evident that the high surface roughness and localized unevenness of the soft coating layer poses significant challenges for the use of conventional analytical methods to evaluate the coating stiffness. Mechanical tests reveal that the stiffness varies across different locations and is largely influenced by local surface roughness. Consequently, an effective stiffness may be more accurately evaluated using a quantitative approach. To facilitate this, a sheet of coated material was prepared to carry out indentation tests, as shown in Figure 3.5.

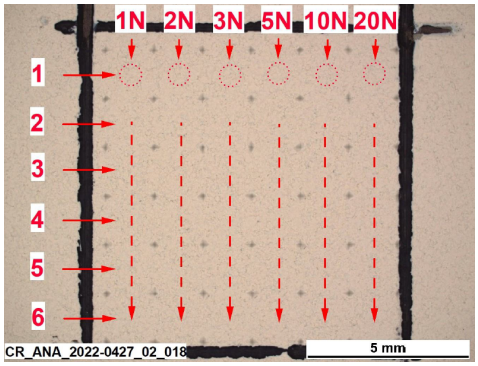

Figure 3.5: Indentation experiments for a sheet of coating material

3-D surface images of the sheet profile were captured at the measurement station. Indentation tests were then conducted on the coated surface over a range of applied forces, as depicted in Figure 3.5. The indentation at each force was repeated six times. Following the indentation, 3-D image data of the indented coating surface was again measured on the measurement station and subsequently post-processed in MATLAB.

To evaluate the effective material properties of the coating, the indented and unindented configurations of the data were compared after appropriate post-processing. The corresponding images before and after one of the indentations are shown in Figure 3.6(a) and Figure 3.6(b). The effective stiffness can be determined by analyzing the deformation for each indentation. This was done by fitting the deformed coating profile to an equation representing the spherical indenter. In the deformed configuration, the data points in close proximity to the indenter were considered to be in contact with the indenter and were deformed during the indentation test. Figure 3.6(c) depicts the spherical indenter and the

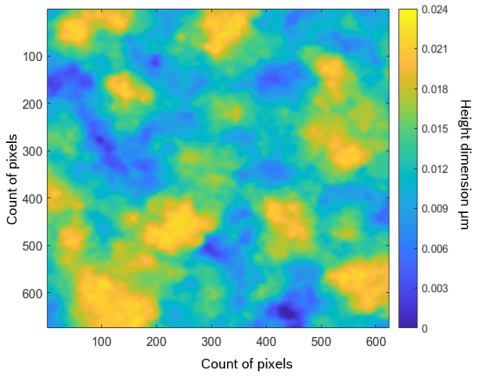

(a) Before indentation

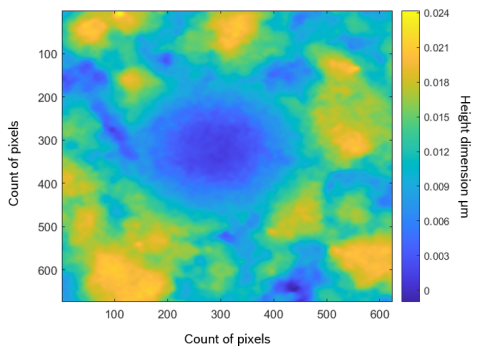

(b) After indentation

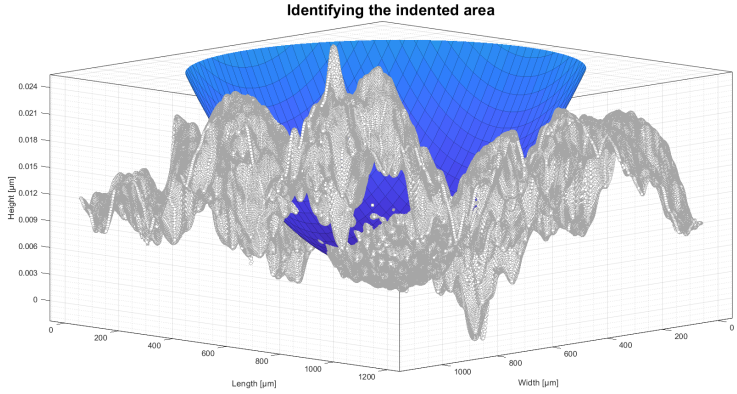

(c) Identifying area indented by spherical indenter

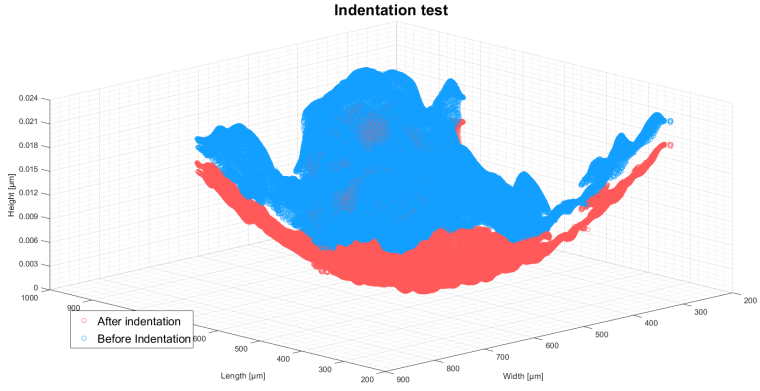

(d) Effective deformation of profile

Figure 3.6: Postprocessing of image data before and after indentation tests

data points in the deformed configuration of the indentation. Data points with residuals within a specified limit relative to the spherical indenter's equation were considered to be in contact with the sphere during indentation and can be considered as the deformed data points. Finally, on identifying the deformed profile of the coating, it was segmented and its corresponding undeformed profile was determined by projecting the deformed area onto the undeformed area. The segmented deformed and undeformed profiles of the coating are shown distinctly together in Figure 3.6(d).

For this data set, the deformation for each data point is represented as $\{x\}_{i=1}^{n}$ where n denotes the total number of indented data points for the current indentation. Additionally, the total force k required for each indentation is known. Based on the force-deformation behavior seen in Figure 3.3(b), an exponential function may be selected as the stiffness function and is represented as follows:

$$f(x_i) = ae^{bx_i} \tag{3.3.1}$$

where, suitable coefficients a and b need to be determined. To do so, the squared errors $E(a, b)$ between the sum of forces acting over the data set $\{x\}_{i=1}^{n}$ given by, $f(x_i) \times x_i$ and total force applied on the indent k must approach zero. The error function $E(a, b)$ can be minimized by optimizing the coefficients a and b of the stiffness function $f(x)$ as follows,

$$E(a, b) = (\sum_{i=1}^{n} ae^{bx_i} x_i - k)^2 \tag{3.3.2}$$

On minimizing $E(a, b)$ considering the entire data set of all 36 indentations, the optimized coefficients of a and b are evaluated. Upon substituting these coefficients in Equation 3.3.1 and resolving the pixel resolution into metric units, the pressure and deformation relationship for the coating is plotted in Figure 3.7(a). The squared errors for each of the force is shown in Figure 3.7(b).

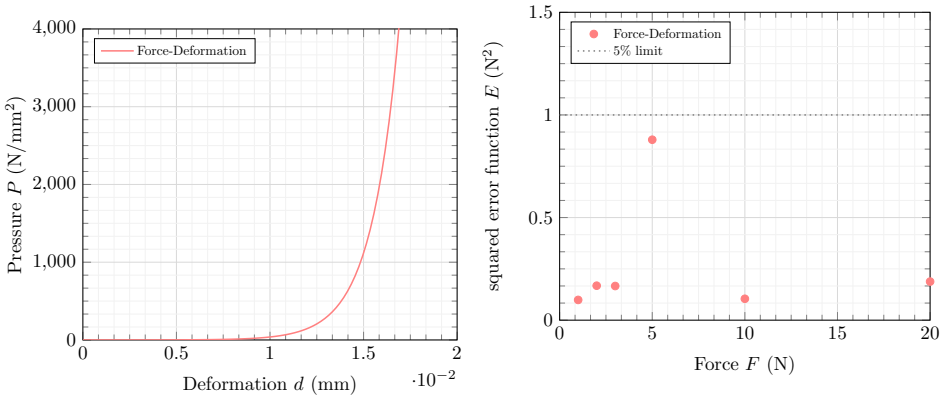

(a) Pressure-Deformation behavior

(b) Squared error function plotted with applied force

Figure 3.7: Generation of effective coating stiffness function and error

3.4 Calibrating mechanical simulations for a single contact

Upon evaluating the effective coating stiffness and characterizing the elastoplastic behavior of the metallic interconnect, a finite element model was developed to simulate the compression of a single interconnect contact. The geometry of the contact was designed to match the specifications of the Bosch-Ceres Power solid oxide fuel cell, identical to the samples tested in the Section 3.2. The characterized material data for Crofer 22 APU was taken from a data sheet of VDM metals, shown in Table 3.1 [120].

Table 3.1: Material data for metallic interconnect according to VDM Crofer 22 APU.

Temperature(°C)	Young's Modulus(GPa)	Yield strength(MPa)
20	220	277
200	210	194
400	195	181
600	183	127

The stiffness of the coating layer evaluated in Section 3.3 is summarized with the pressure-closure relationship in Table 3.2.

Table 3.2: Pressure-closure relation for coating layer.

Pressure (MPa)	Closure (mm)
0	0
0.0581	0.0004
0.087	0.001
1.7	0.005
10.41	0.008
80.70	0.011
476.116	0.0137
2137.63	0.0159
5558.8	0.0173

For discretizing the metallic interconnect, C3D8 hexahedral elements were chosen, while the coating layer was modeled using GK3D8N gasket elements. The gasket material model was selected due to its ability to accurately represent the exponential stiffness behavior observed in the coating layer, as shown in Figure 3.7(a). Moreover, the gasket material model represents plastic deformation in the thickness direction without causing a lateral strain, therefore, it was optimal for the coating. For the compression test, the arrangement of the interconnect and coating were sandwiched between rigid plates comprised of R3D4 discrete rigid elements. In order to select the appropriate mesh resolution for the interconnect contact geometry, a mesh convergence study was performed, which will be discussed in detail in Section 4.1. The single contact is loaded uniaxially under compression between the rigid plates over a period of one static time-step for a normalized deformation. The corresponding output parameters were numerically calculated by the finite element solver. All finite element calculations were done using commercially available software ABAQUS 2022 [121]. The corresponding normalized force-deformation relation for the contact was plotted in Figure 3.8 and was compared to the experimental relation obtained on compressing coated contacts in Section 3.2.

Comparison of the simulation results with experimental tests reveals that the input parameters and discretization used in the finite element model closely align with experimental tests. This indicates that the material parameters for the coating and the material moduli for the metallic interconnect are appropriate for mechanical simulations of a single SOC contact providing a reliable representation of the addressed phenomena. This model will be taken as a benchmark for further analysis in subsequent chap-

ters.

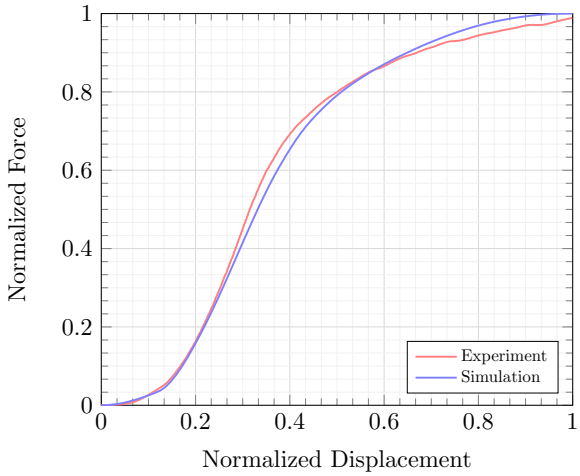

Figure 3.8: Force-deformation relation for experimental tests and simulations

3.5 Calibrating thermal simulations for a single contact

Following the experimental comparison of the mechanical simulation at room temperature, the *temperature ramp-up* loading case is studied in this section. As outlined in Section 3.1, during this phase, the deformation of the contact is constrained while the temperature is increased, causing thermal expansion of the contact which in turn causes an increase in the applied force. With the existing equipment, it was not possible to directly measure the forces acting on the contact at elevated temperatures. Therefore, instead of holding the deformation, the force is kept constant during temperature change and the resulting plastic deformation is evaluated. This forms a basis for validation of the elastoplastic moduli at elevated temperature for the given loading conditions.

The finite element model incorporates the temperature-dependent elastoplastic properties of the metallic interconnect as outlined in Table 3.1, as well as the compressed configuration of the coating. As a suitable set of loading conditions, first, the contact is compressed mechanically until a constant target force is achieved. On reaching this force, the model is then subjected to a temperature increase from room temperature, up to

operational temperature, while maintaining the constant force. The temperature is then reduced back to room temperature with the constant force throughout the process. Finally, the force is unloaded to evaluate the total plastic deformation over the loading cycle.

The temperature-deformation relation is plotted in Figure 3.9(a). The blue circle in Figure 3.9(a) shows the plastic deformation at the end of the loading cycle. As stated in Section 3.1, the increase in temperature leads to a decrease in the yield limit of the material. When the yield limit falls below the applied stress, it causes the onset of plasticity. This phenomenon is precisely seen in the temperature-deformation relationship plotted in Figure 3.9(a).

To validate the simulation results, an experimental setup is designed where a single interconnect contact is compressed at room temperature under a force magnitude corresponding to that used in the simulation. The compressed contact is held under a constant force and heated in an oven from room temperature to operational temperature. The temperature at the contact is monitored using a thermoelement over the duration of the thermal loading. The contact is held at this temperature for a specified period of time and then cooled down to room temperature. After the thermal loading cycle, the contact is mechanically unloaded and the plastic deformation is measured by comparing the initial an final geometric profiles of the contact.

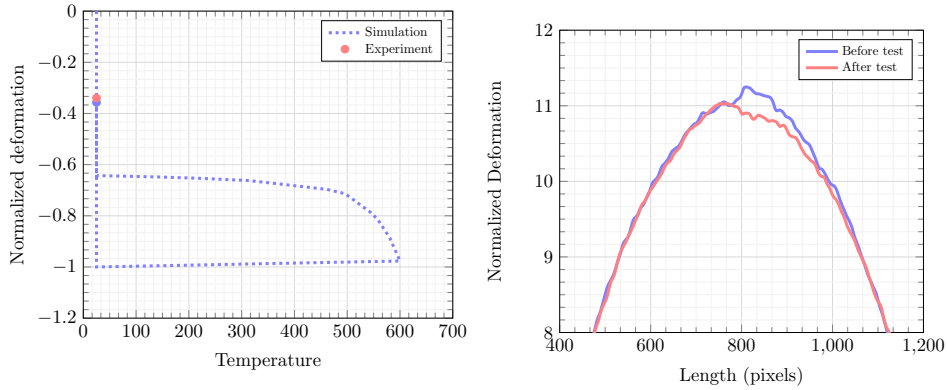

(a) Temperature-deformation relation on loading a single contact

(b) Profile of the contact before and after test

Figure 3.9: Temperature-deformation relation for experimental tests and simulations

The measured profiles of the contact under thermal loading at constant force, before and after the test, are plotted in Figure 3.9(b). The corresponding plastic deformation

obtained from the experiment is projected onto the simulated temperature-deformation curve shown in Figure 3.9(a) using the red circle. A comparison of the measured and simulated plastic deformation shows that the simulation results closely aligns with the experimental tests which in turn confirms that the finite element model captures the behavior of the contact. This provides confidence that model parameters can be used as a benchmark for subsequent analysis of thermal loading on the contact.

3.6 Calibrating rate-dependent simulations for a single contact

After validating the model parameters for thermal loading during the temperature ramp-up phase, the next step is the evaluation of the model under operational conditions. Typically during operation, the deformation and temperature of the stack are held constant over extended time periods as outlined in Section 3.1. This prolonged loading conditions lead to viscous relaxation of the contact forces. However, it is difficult to obtain direct force measurements under these operating conditions with high temperatures and small force ranges experimentally, over a single contact.

Table 3.3: Creeping material data

Temperature (°C)	Power law multiplier (A)	Eq stress order (n)
600	$2.9902E-13$	3.8515

Therefore, instead of measuring the contact forces directly, the model may be alternatively validated for a constant force while measuring the plastic deformation at the end of the loading cycle. This allows the model parameters to be tested for the creep behavior. Although, in practice may be possible, however, the time scales required to obtain the deformed configuration of a contact is of the order of several thousand hours, which is experimentally expensive and not feasible for a single contact. Due to the availability of well characterized material data from several past works and the high reliability on simulation data for this aspect, the model may be assumed to represent the phenomena based on Norton creep law $\dot{\boldsymbol{\varepsilon}} = A.\boldsymbol{\sigma}^n$ with coefficients A and n mentioned in Table 3.3 [29, 122–125].

To simulate this behavior, the finite element model of a single interconnect contact was first loaded mechanically until a nominal target force was achieved. With the force held constant, the model is subjected to a thermal loading to increase the temperature to operational levels. The system is then maintained in this configuration over extended time periods to simulate the creeping effect under operating conditions over a viscous time step. The resulting deformation over time is plotted in Figure 3.10. This graph illustrates the gradual creep deformation that occurs under constant load and operational temperatures. It may be noted that the plot in Figure 3.10 was normalized and the time scale is in the order of several thousand hours.

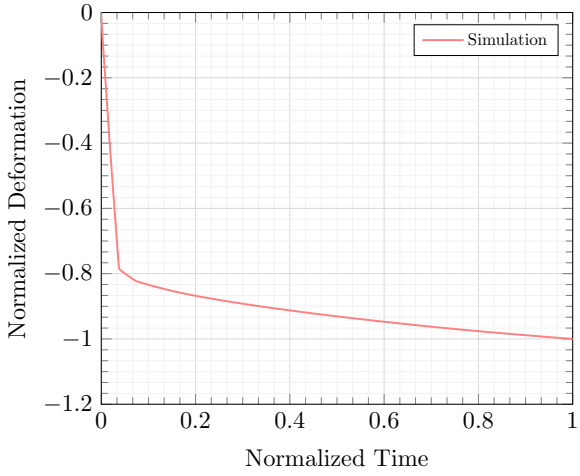

Figure 3.10: Time-deformation behavior on loading a single contact

3.7 Summary

In summary of this chapter, the mechanical loading behavior of the metallic interconnect and coating was characterized. A finite element model was developed and validated against experimental tests, demonstrating that the model accurately represents the test conditions across various loading cases. The goal of this chapter was to construct a model that closely reflects experimental tests by defining appropriate model parameters for the applied boundary conditions. From this point on, the model will serve as a benchmark for further evaluation and development of this work.

4 Modeling approach and constraints

In the previous chapter, a finite element model was developed for a single SOC contact and validated against experimental tests for selected loading steps. This chapter initially focuses on the challenges of modeling SOC stacks within a finite element framework. The constraints with the significant computational resources required for stack-level simulations is discussed along with highlighting the necessity for model simplification. The approach proposed in this work uses computational homogenization which is applied to the previously stated loading cases in the life-cycle of an SOC contact: *1. Assembly at room temperature*, *2. Temperature ramp-up* and *3. Relaxation at operational temperature*. After a successful attempt at applying computational homogenization to an ideal contact, experimental tests are examined, revealing manufacturing non-idealities across repeat-units. These non-idealities are measured and characterized, disclosing that existing simulation methods cannot precisely model such tolerances for each contact without requiring an impractically large computational effort. In the subsequent chapters, the computational homogenization approach will be further developed to address these challenges within the finite element framework.

4.1 Requirement for model reduction

In Section 3.4, a finite element model was developed for the mechanical compression of the metallic interconnect coated with a soft, porous coating layer and was validated against experimental tests. On comparing the simulated force-deformation behavior with experimental data, the finite element simulation showed a high degree of accuracy in representing the observed phenomena. Additionally, the model provided valuable insights into the stress distribution and deformation behavior of a single contact under applied loads, giving a more detailed understanding of the compression process.

For such kind of accuracy, however, the model required a high level of discretization because of its complex design and corrugated geometry which in turn requires large computational resources for completion. This is because the mesh resolution directly impacts the model's accuracy for such kind of design and thus, an optimal balance between accuracy and computational cost must be determined. This is achieved through a mesh convergence study, which evaluates the number of elements necessary for a fairly accurate finite element analysis while optimizing computational costs [126–128].

The metallic interconnect contact was discretized using C3D8 hexagonal elements in ABAQUS 2022, while the soft porous coating was modeled using GK3D8N gasket elements, as described in Section 3.4. In order to assess the model accuracy with different mesh resolutions, five different configurations of discretization were tested: the model was discretized into 1,692 elements, 5,338 elements, 16,148 elements, 63,225 elements, and 217,292 elements, as shown in Figure 4.1. Each configuration of these discretized geometries were then subjected to uniaxial compression of 0.05 mm in the out-of-plane direction, and the corresponding force-deformation responses were plotted in Figure 4.2.

The results indicate that the initial deformations in the elastic region showed good agreement across all mesh resolutions. However, with increased deformation, a deviation in the force of about 11% was observed between the coarsest and finest meshes. This deviation between configurations diminished as the mesh resolution increased. The configuration using 63,225 elements converged closely with the 217,292 element model and is regarded as the optimal mesh resolution for this study. Consequently, this discretization was used for all subsequent full-field simulations, including those presented in Chapter 3.

With a discretization of 63,225 elements, the computation time required for the compression of a single contact was recorded as 01:38:45. While this level of detail is feasible for modeling individual contacts, it becomes impractical for commercial stack-level simulations because of the use of hundreds of repeat units with each containing thousands of such contacts. This results in an enormous number of elements leading to excessively long computational times.

In order to make stack-level simulations more manageable, it is essential to reduce the number of elements. There have been several approaches in literature to model the mechanical robustness of the SOC stack. While some of the simulation approaches still rely on brute force of computations [26], others may consider a symmetric section of the stack [27, 129]. Some other models consider a repeat unit as representative of the

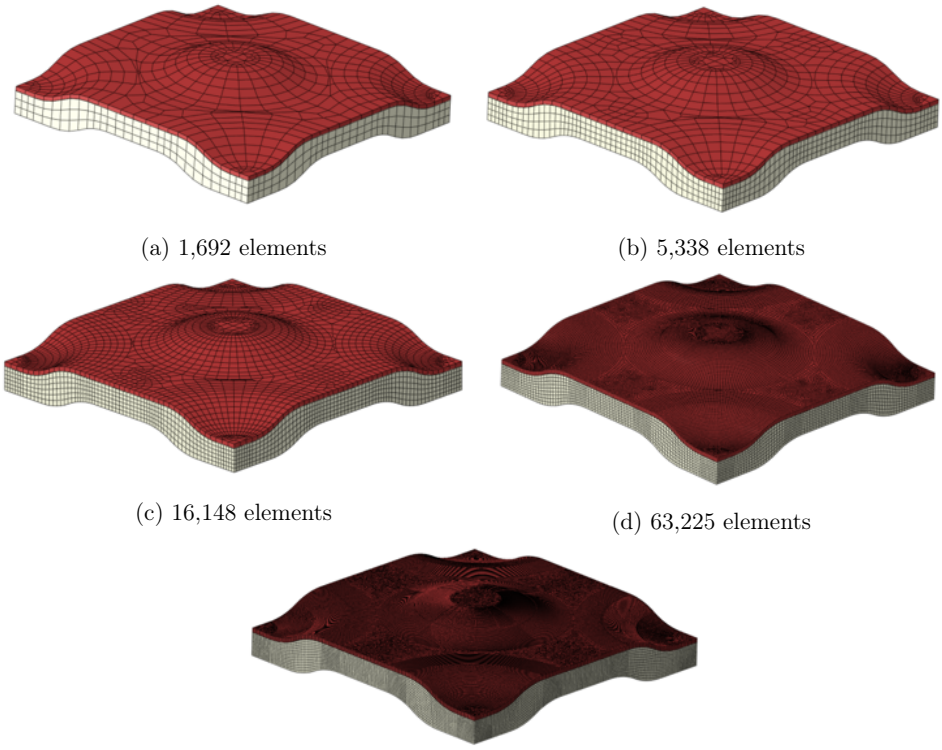

(a) 1,692 elements

(b) 5,338 elements

(c) 16,148 elements

(d) 63,225 elements

(e) 217,292 elements

Figure 4.1: Discretization of a single coated contact

stack and assume that all non-ideal features for the repeat unit are representative for the stack [7, 8]. However, most modeling approaches use some form of simplification to achieve convergence at practical computational run-times. Some recent works consider the homogenization approach [29, 122, 124] and exploit the periodically repeating structure of the contacts in a stack. This approach called computational homogenization is highly efficient and considers the representative volume as a homogeneous continuum of bulk material. Furthermore, it allows for a reduction in model complexity while preserving the accuracy of the key mechanical parameters and will be discussed in Section 4.2.

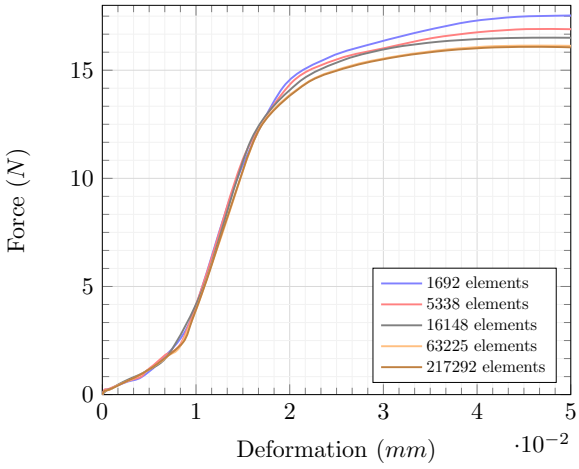

Figure 4.2: Mesh convergence study for different geometric discretization

4.2 Practical application of the computational homogenization approach

The interconnect geometry is a periodically repeating structure in the active area of the SOC stack and therefore may be exploited for periodic homogenization. The portion of the interconnect which appears to be periodic is identified as the representative volume element (RVE) and highlighted in Figure 4.3. The representative unit volume is primarily comprised of one interconnect contact and its coating. For homogenization in the out-of-plane loading direction, these components are sandwiched between rigid plates. These plates comprised of discrete rigid elements are generally limited when setting kinematic equation constraints at its nodes in finite element solvers, therefore, this geometry is again sandwiched between non-rigid plates for a consistent set of periodic boundary conditions as described in Figure 4.3. The non-rigid plates are only placed to link the corner, edge and face nodes at the top and bottom faces and show no contribution to the stress-strain response. For in-plane loading, the plates are not included for the kinematic equation constraints.

Periodic boundary conditions were applied to the representative unit volume referring to the work of Li et al. [130] and Chatzigeorgiou et al. [131–133]. Based on their work, kinematic equation constraints were set up on edges, corners and faces of the unit cell. These were linked to six reference nodes called *key degrees of freedom* in directions (xx,

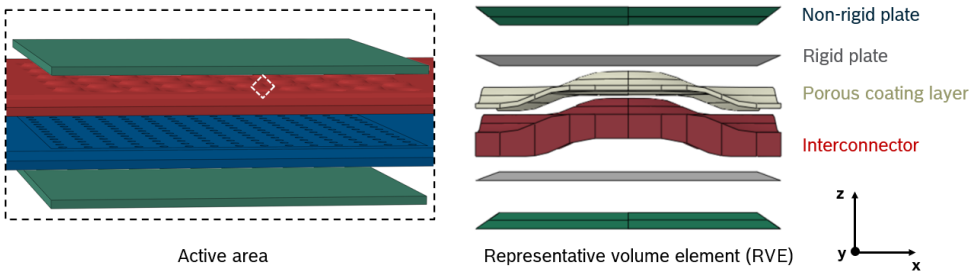

Figure 4.3: Definition of representative volume element

yy, zz, xy, yz, xz). In this approach, nodal displacements at these key degrees of freedom are equal to the homogenized strains in the corresponding direction. Based on these nodal constraints, the nodal displacement at the key degree of freedom in any direction is,

$$u^{cd}_{dir} = \frac{u^{cd}_{dir}}{l_{dir}} \qquad \text{and} \qquad \varepsilon_{dir} := u^{cd}_{dir} \tag{4.2.1}$$

where, u_{dir} represents the displacement in any given direction (dir), l_{dir} represents the initial dimension of the RVE in direction (dir) and ε_{dir} is equivalent to the homogenized strain component in that direction. Concentrated forces at the key degrees of freedom have dimensions equivalent to force times length. Therefore, the nodal force at the key degree of freedom in any direction (dir) is,

$$f^{cd}_{dir} = f_{dir}.l_{dir} \qquad \text{and} \qquad \sigma_{dir} := \frac{f^{cd}_{dir}}{V} \tag{4.2.2}$$

where, f_{dir} represents the force in any given direction (dir) and l_{dir} represents the initial dimension of the RVE in direction (dir). On dividing by the volume (V) of the RVE, σ_{dir} corresponds to the homogenized stress component in that direction. The homogenized stress is, therefore, equal to the concentrated force at the key degrees of freedom divided by the volume of the unit cell.

The representative volume is loaded with the stated periodic boundary conditions and subjected to several loading cases. The loading cases used are corresponding to the process steps in the lifecycle of an SOC contact outlined in Section 3.1. In the subsequent

subsections, these corresponding loading cases are evaluated for a homogenized SOC contact.

4.2.1 Assembly at room temperature

An SOC contact is typically compressed mechanically at room temperature to establish a mechanical pressure at the contacts. To simulate mechanical loading, the RVE was first subjected to periodic boundary conditions as demonstrated in Section 4.2 and was loaded in all the principle directions for a complete anisotropic mechanical loading configuration. Due to in-plane symmetry of the representative volume, the elastoplastic stress-strain responses were computed for only four out of the six loading cases. Each of the cases were loaded with a uniaxial strain of 0.05.

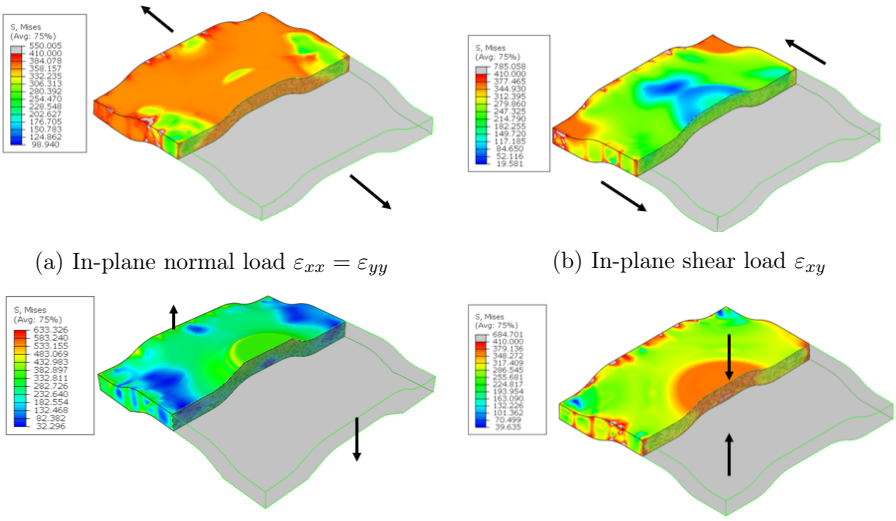

(a) In-plane normal load $\varepsilon_{xx} = \varepsilon_{yy}$

(b) In-plane shear load ε_{xy}

(c) Out-of-plane shear load $\varepsilon_{xz} = \varepsilon_{yz}$

(d) Out-of-plane normal load ε_{zz}

Figure 4.4: Von Mises stress distributions in the high-fidelity interconnect model.

The concentration of Von Mises stress in the cross section of the metallic interconnect contact for these loading cases are shown in Figure 4.4. Figure 4.4(a) shows the case for uniaxial normal loading in the in-plane direction (xx, yy). Similarly, Figure 4.4(d) shows the uniaxial normal loading case in the out-of-plane direction (zz). Figure 4.4(b) and Figure 4.4(c) show shear loading cases in the in-plane (xy) and out-

of-plane (xz, yz) directions. The results for all these loading cases are summarized in Figure 4.5(a).

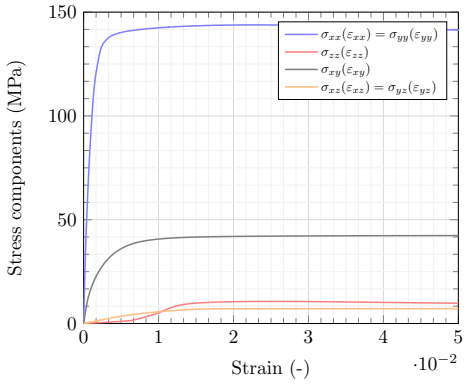

(a) Stress-strain responses for normal and shear loading in the in-plane and out-of-plane direction.

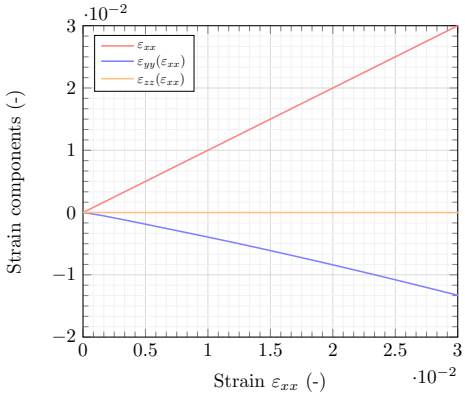

(b) Strain components $\varepsilon_{xx}(\varepsilon_{xx})$ and $\varepsilon_{yy}(\varepsilon_{xx})$ as a result of a normal in-plane strain driver ε_{xx}.

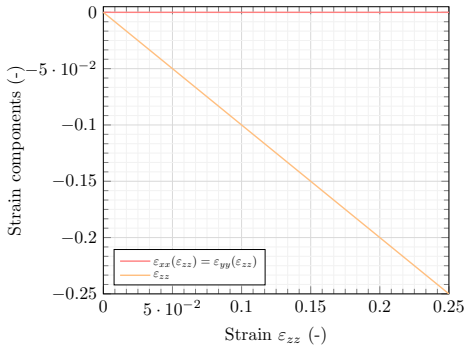

(c) Strain components $\varepsilon_{xx}(\varepsilon_{zz})$ and $\varepsilon_{yy}(\varepsilon_{zz})$ as a result of a normal out-of-plane strain driver ε_{zz}.

Figure 4.5: Results of computational homogenization

The stress-strain responses showed significant anisotropy between in-plane and out-of-plane loading directions. Figure 4.5(a) shows that the yield stress in the out-of-plane direction was about one order of magnitude lower than the in-plane direction. It also suggests that the interconnect contacts were significantly stiffer in-plane, however, there is no primary loading in this direction during stacking.

Another important parameter to consider is the volume dilation during uniaxial loading. This may be observed by examining the relationship between the applied driving strain with the resulting corresponding strain components for a uniaxial normal loading in Figure 4.5. Figure 4.5(b) shows the corresponding strains $\varepsilon_{yy}(\varepsilon_{xx})$ and $\varepsilon_{zz}(\varepsilon_{xx})$ resulting from an in-plane normal loading strain ε_{xx} and Figure 4.5(c) shows the corresponding in-plane strains $\varepsilon_{xx}(\varepsilon_{zz})$ and $\varepsilon_{yy}(\varepsilon_{zz})$ as a consequence of an out-of-plane normal loading strain ε_{zz}. Figure 4.5(c) suggests that the interconnect contacts collapse in the out-of-plane direction without significant in-plane dilation. Another observation in Figure 4.5(a) suggests that the normal out-of-plane loading ε_{zz} has an initial nonlinear stress response in the out-of-plane stress component $\sigma_{zz}(\varepsilon_{zz})$, which characterizes the influence of the coating layer discussed in Section 3.2. This behavior is crucial because it is in the direction of primary loading during the mechanical stack assembly process.

4.2.2 Temperature ramp-up

After the mechanical stacking process, the next loading step in the life-cycle of an SOC contact is the temperature ramp-up. At this stage, the contact is typically heated up from room temperature of about 25°C to operational temperature of 600°C. During such a thermal loading, various temperature-dependent parameters such as thermal expansion and change in elastoplastic moduli come into play and may affect the stress state of the contacts.

In order to simulate this step, the RVE is first subjected to periodic boundary conditions outlined in Section 4.2. Then, the RVE is compressed mechanically in the out-of-plane direction to represent the stacking process to reach a mechanically compressed stress configuration. The stress-concentration on a single homogenized contact is depicted in Figure 4.6 and the stress-strain response during this out-of-plane loading, denoted as $\sigma_{zz}(\varepsilon_{zz})$ is plotted in Figure 4.7(a).

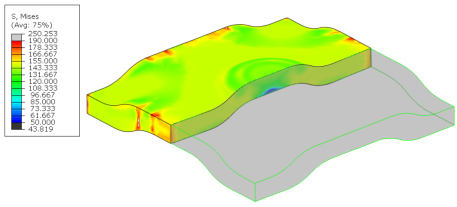

Figure 4.6: Thermal expansion of mechanically pressed contact

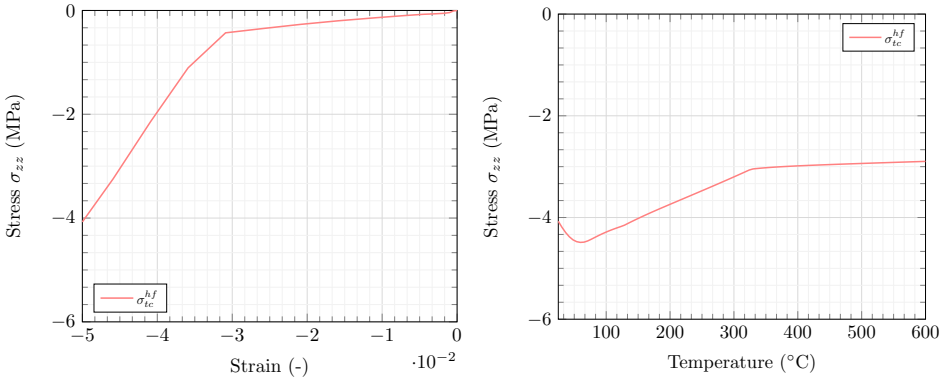

(a) Stress-Strain response for mechanically loading

(b) Stress-Temperature response for corresponding thermal loading

Figure 4.7: Results of computational homogenization for temperature ramp-up

During the stacking process, the primary mechanical loading occurs in the out-of-plane direction and the in-plane yield limit is significantly higher than the out-of-plane yield limit as shown in Section 4.2.1. Therefore, only the out-of-plane normal case is considered for the subsequent analysis.

Upon reaching the mechanically compressed configuration, shown in Figure 4.7(a), the RVE is held in this state by constraining its deformation in the out-of-plane direction. The RVE is then subjected to a thermal load, where the temperature T is increased from 25°C to 600°C. The corresponding stress $\sigma_{zz}(T)$ is plotted with temperature in Figure 4.7(b).

The stress-temperature relationship in Figure 4.7(b) exhibits a highly non-linear behavior. Initially, the stress increases with temperature because the material is within the elastic domain. However, as the temperature rises, the yield limit of the material decreases and becomes lower than the applied stress causing the onset of plasticity. This is because of the temperature-dependent nature of the yield limit which decreases as the temperature approaches the operating temperature of 600°C. Therefore, during temperature ramp-up the stress response shows a transition from elastic to plastic deformation due to the combined effects of thermal expansion and the onset of plasticity in the RVE.

4.2.3 Relaxation at operational temperature

Once the temperature of approximately 600°C is reached, the contact is held under steady-state conditions at constant temperature for prolonged time periods during operation. At this stage, the contacts remain in their current deformation state and a viscous relaxation occurs over time. This relaxation leads to a reduction in the stress on the contact over prolonged time scales.

In order to estimate the influence of relaxation on the current stress state, the RVE is subjected to periodic boundary conditions as described in Section 4.2. The homogenized stress-state at the start of operation is approximately 3 MPa, which is obtained after the temperature ramp-up loading step discussed in Section 4.2.2. Figure 4.8 illustrates the Von Mises stress concentration at a single homogenized contact during operation, at a constant temperature of 600°C.

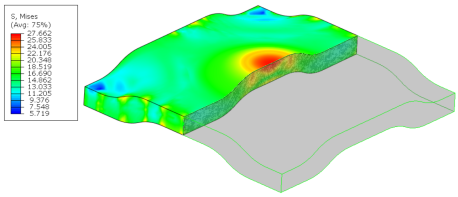

Figure 4.8: Relaxation behavior of contact during operation

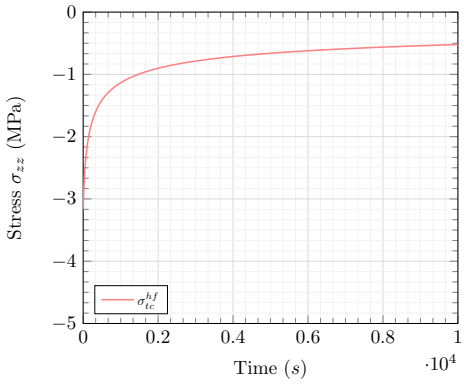

Figure 4.9: Stress-Time response for during operation

The RVE is held in this configuration with fixed displacement and temperature boundary conditions for a given time duration of $10^4 s$ using a viscous time step. The evolution

of the stress $\sigma_{zz}(t)$ in the out-of-plane direction is plotted over time in Figure 4.9. It is observed that there is a relaxation of homogenized stress response from 3 MPa at the start of operation to about 0.5 MPa by the end of the time step.

This stress relaxation is a critical aspect of the contact behavior during stack operation. The reduction in stress influences the mechanical contact pressure at the contacts and increases performance losses of the stack over its life-time.

4.2.4 Interpretation of results for computational homogenization

In the process of homogenizing interconnect contacts for the various loading cases described in Section 4.2.1, Section 4.2.2 and Section 4.2.3, the response for each loading step is computed in these corresponding sections. This is the homogenized response of the representative volume which captures the detailed geometry and material behavior of the interconnect contact and is referred to as the *high-fidelity model*.

This high-fidelity model may be replaced by a simpler model with reduced geometric complexity and lower mesh resolution which is referred to as the *effective model*. The objective of this approach is to fit the stress response behavior of the effective model with that of the high-fidelity model across all loading-steps and ensure that the effective model provides an accurate representation of the high-fidelity model with an optimized computational efficiency. Once the effective model is demonstrated to exhibit equivalent stress responses to the applied stress drivers across these loading cases, it may be used to represent the high-fidelity model under similar loading conditions.

Figure 4.10 illustrates the high-fidelity and effective models for the representative volume. This model simplification technique exploits the fact that the high mesh resolution is an attribute of the complex geometry which contributes to long simulation times. This complex geometry may be replaced with an equivalent material response, reducing the overall computational cost significantly while maintaining a desired level of accuracy in the average homogenized responses [134–137].

However, the approach suggests that the representative volume may be treated as a continuum, which implies, the stress is evenly distributed across the active area, in an ideally designed stack [29, 122, 124, 138]. Although, this may help simplify the analysis, it may not fully capture the real-world scenario with non-idealities. A set of brief

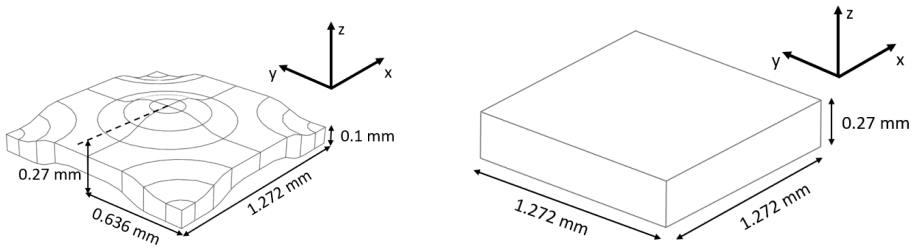

(a) High-fidelity model

(b) Effective-model

Figure 4.10: Homogenization strategy for model simplification

experimental investigations are looked at in the next Section 4.3. The insights obtained from such tests may motivate the development of more accurate simulation strategies to model the experimentally observed phenomena in the homogenization framework.

4.3 Observations from experimental investigations

Computational homogenization offers a potential solution to the challenge of long simulation times. However, to verify the suitability of this approach for accurately simulating the required phenomena, it must be compared with experimental results. To achieve this, experimental investigations are conducted on the coated metallic interconnect under mechanical loading, providing a basis for comparison with the homogenized model.

Some studies conducted in literature show experimental investigations using pressure films to evaluate the contact pressure distribution in the active area [139–143]. In this approach, a pressure film is placed on the contacting surface and a mechanical compressive load is applied onto the repeat unit. After removing the load, the imprint on the film serves as a visual representation of the pressure distribution. The data generated from the pressure film is subsequently postprocessed to generate a continuous pressure distribution contour. Figure 4.11(a) and Figure 4.11(b) depict the contact pressure contours for two different repeat units, tested under identical conditions. The experimental procedure and data analysis will be discussed in greater detail in Section 8.1.1.

During these tests, as observed in Figures 4.11(a) and 4.11(b), the mechanical contact pressure distribution in the active area is inhomogeneous during the mechanical assembly process, which cannot be captured by the suggested simulation approach in Section 4.2. Additionally, each repeat unit exhibited a unique contact pressure distribution pattern, despite identical testing conditions.

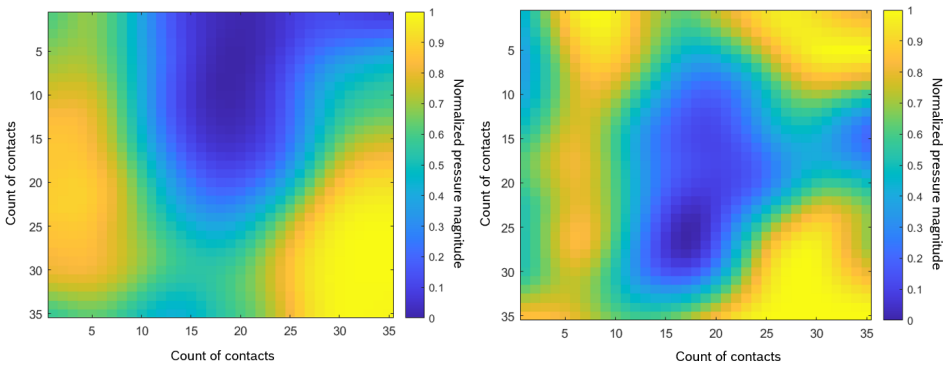

(a) Contact patterns: Cell-1

(b) Contact patterns: Cell-2

Figure 4.11: Contact pressure distribution for two cells using pressure film tests

From these observations, two key inferences may be drawn:

- Heterogeneity in the contact pressure distribution within a single repeat-unit may be due to non-idealities inherent to the repeat-unit.
- The variation in contact pressure distribution between different repeat-units may be caused by non-repeatability of repeat-units.

These observations point to the presence of non-idealities in the active area of individual cells, leading to non-uniform contact pressure distributions. Furthermore, the variance in these non-idealities between manufactured cells may explain the distinct contact patterns observed in Figure 4.11(a) and Figure 4.11(b). These insights provide a strong basis to investigate the variability between manufactured components which point to specific manufacturing parameters that could introduce such a variance in the contact quality during the mechanical stack assembly process. Once these parameters are identified, the homogenization approach may be further developed to consider these variances. This will in turn estimate their effect on the performance and help formulate appropriate measures.

4.3.1 Measurement of repeat units

In order to address the non-repeatability of contact distribution patterns observed in Section 4.3, interconnects and substrates of several repeat units were analyzed to identify the parameters contributing to this variance. These components were measured at a measurement station which comprised of scanners that generate a 3-D image of the workpiece under analysis.

The measurement device, shown in Figure 4.12, consists of two sensors positioned on either side of the workpiece, operating with the principle of laser triangulation [144]. Measurements are taken from both sides as the sensors move gradually across the spatial plane of the workpiece and capture height data over the entire surface of the components. This results in a comprehensive 3-D representation of each component which can be then post-processed using commercially available software like MATLAB.

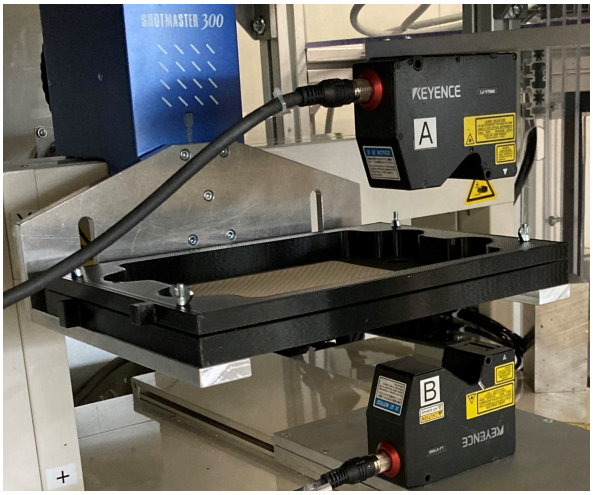

Figure 4.12: Measurement of components of an SOC repeat unit

On comparing the measurements of components like interconnects and substrates across several repeat units, it was observed that the manufactured components exhibit tolerances that may influence the contact behavior within a stack. These tolerances can be categorized as follows:

- Non-flatness of components across repeat units.
- Dimensional tolerances at interconnect contacts.

These identified non-idealities are inconsistent in individual components and is considered to be the source of non-repeatability of the contact behavior in the experimental tests. In the next subsections, these measured non-idealities are looked into in more detail.

4.3.2 Non-flatness of components

During manufacturing of components, dimensional non-idealities can occur in repeat units due to various factors associated with the manufacturing processes. One such form of tolerance distinctly observed from measurements of several parts is in the flatness profiles of components, such as substrates and interconnects, which were found to have distinct profiles. Due to the non-repeatability of flatness profiles among repeat units, the non-flatness could contribute to the non-repeatability of contact patterns among cells. Therefore, accurately measuring and quantifying the flatness of each repeat unit is essential. The measurement station described in Section 4.3.1 scans each component and generates three-dimensional spatial image. This image is post-processed in MATLAB to fit an n^{th}-order polynomial function in three dimensional space, to obtain the component profile, where n is of the order four or five. The equation of this polynomial plane may be expressed as:

$$f(x,y) = \sum_{i=0}^{n} \sum_{j=0}^{n-i} a_{ij} x^i y^j \tag{4.3.1}$$

where i and j are the powers of x and y with the limiting condition $(i+j \leq n)$ and a_{ij} corresponds to the coefficients which can be determined from a curve fitting routine. The image data measured on the interconnect and substrate for two such repeat units are fitted on to Equation 4.3.1 using a 5^{th} degree polynomial function and setting appropriate coefficients. Their corresponding profiles are plotted in Figure 4.13.

On comparing the profiles of the components of the two repeat units and on measuring several other components, it was observed that the flatness profiles of each manufactured component showed no correlation with any other components. This inferred that the flatness profiles for each manufactured component was unique.

On stacking such sheets with varying flatness profiles, the influence of such non-flatness is expected to affect the contacting configuration in a stack which could in turn be one of the causes for heterogenous contact pressure distributions. These mechanical contact pressure distributions are known to impact the electrical contact resistance and

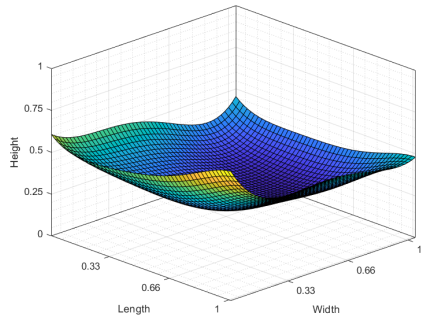

(a) Interconnect Measurement: Cell 1

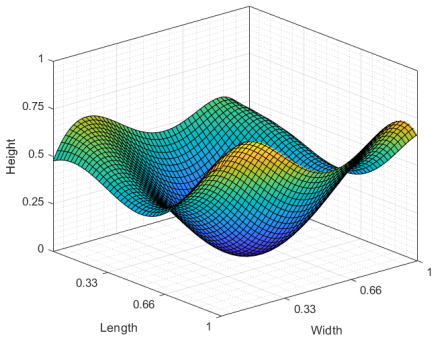

(b) Substrate Measurement: Cell 1

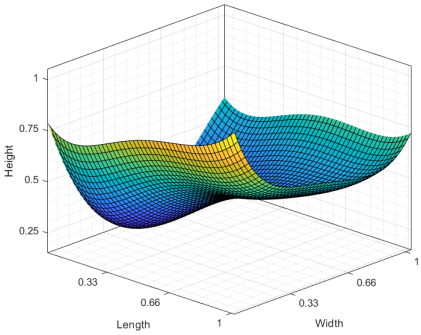

(c) Interconnect Measurement: Cell 2

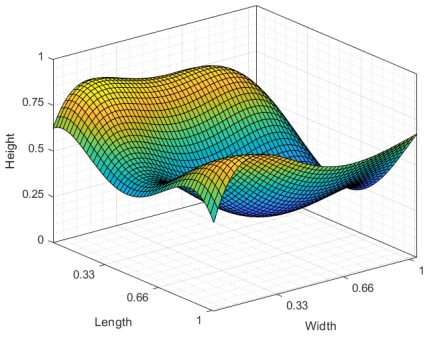

(d) Interconnect Measurement: Cell 2

Figure 4.13: Profile measurements of components of a cell (height axis is scaled in comparison with length and width)

thus the performance of the stack. The effect of such profile variability may be investigated in the finite element framework by characterizing profiles of individual components as done in Equation 4.3.1 and understanding their influence on the stacking process.

4.3.3 Dimensional tolerances on individual contacts

Along with the non-flatness of components, another non-ideal manufacturing effect seen was the dimensional tolerances of contacts. Based on several sets of measurement data, it was seen that the manufacturing processes of the interconnect had tolerances in repeatability of the contact dimensions in the active area. Of these tolerances, particularly the height dimension was considered critical for electrical contacting and needed to be investigated.

In order to do so, the 3-D spatial data obtained from the measurement station described in Section 4.3.1 was postprocessed so that the flatness profile is fit onto the 5^{th} degree polynomial function as described in Section 4.3.2. Upon isolating the effects of non-flatness, the distribution of contact heights are observed in Figure 4.14. The maximum heights of each contact on an uncoated metallic interconnect is evaluated and a matrix of these tolerance values in the active area is created. Figure 4.14(a) and Figure 4.14(c) show the distribution of dimensional tolerances in the active area for two interconnects. The probability distributions in Figure 4.14(b) and Figure 4.14(d) help understand the variance in the tolerances of multiple interconnects. It was seen that the tolerances were in the range of about 20 μm. The cause of such dimensional variability is because of manufacturing parameters like tool wear, material imperfections or process tolerances, which cannot be changed without significantly modifying production processes. Another observation seen from analyzing several parts is that the spatial distribution of contact height variance in the active area changes significantly between parts. Therefore, it may be inferred that each interconnect has a different configuration of height tolerances at the contacts.

This dimensional variability is expected to contribute to the heterogenous contact patterns seen in Section 4.3 causing large mechanical pressures on taller contacts and lower or no mechanical pressures on relatively short contacts. This not only results in large electrical resistances at short contacts but may also cause excessive plastic deformation of tall contacts and eventually lead to failure of the stack. Therefore, along with the influence of non-flatness, it is necessary to consider dimensional variance in the contact heights to

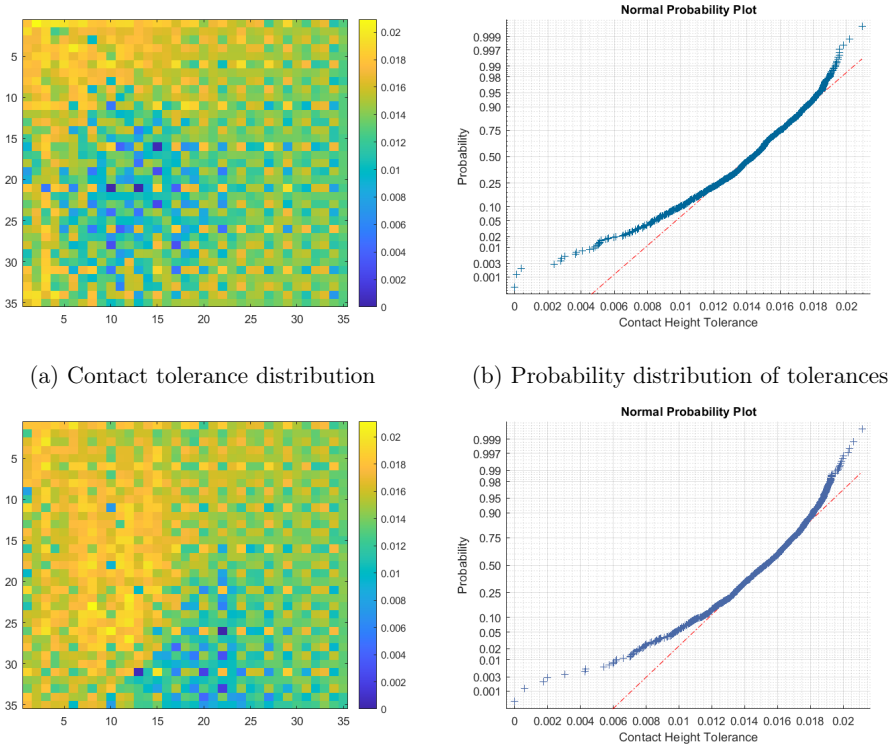

(a) Contact tolerance distribution

(b) Probability distribution of tolerances

(c) Contact tolerance distribution

(d) Probability distribution of tolerances

Figure 4.14: Contact height tolerances in the active area for two interconnects

understand the contact pressure distribution in a stack and eventually relate it to the electrical contact resistance.

4.4 Summary and outlook

In this chapter, the modeling constraints in regard to simulation resources required for a full-field model were highlighted, along with the proposition for the use of computational homogenization techniques to simplify the model complexity. This approach was investigated for the three process steps in the lifecycle of an SOC contact.

In Section 4.2.1, Section 4.2.2 and Section 4.2.3 the homogenized loading cases were applied to the representative unit volume and the corresponding stress was plotted with

their drivers for each loading case. The mechanical loading showed considerable anisotropy accompanied by the possibility for plastic deformation. Moreover, for the out-of-plane loading cases, the effect of the coating needs to be considered along with the unique volume dilation in the plastic domain which also needs to be accounted for. During thermal loading, an effect of the temperature dependence on the elastoplastic moduli was accompanied by thermal expansion. Lastly, a viscoplastic relaxation was observed during operation which must also be considered.

On performing experimental investigations, the non-idealities were observed in manufactured repeat units like varying flatness profiles and dimensional tolerances, must be accounted for to get a comprehensive understanding of the contacting quality. This summarizes the modeling characteristics required to be incorporated in the effective model. In the next chapters, these characteristics are systematically introduced into the effective model to construct a suitable modeling framework running with practical computational times.

5 Constitutive model

In Chapter 4, the computational homogenization approach was discussed to overcome the constraints posed by large computational times which lead to the development of a simplified effective model. Based on experimental investigations outlined in Section 4.3, certain manufacturing tolerances were observed to show significant impact on the contacting configuration in the active area for the chosen SOC design. These tolerances arise due to real-world manufacturing limitations and motivate the use of computational homogenization to account for their effects. Homogenization allows for evaluating the average responses of the geometrically complex representative volume and captures the essential physical responses without the need for computationally expensive models having a high degree of precision. However, the typically available material models in standard simulation software like ABAQUS are limited to conventional elastoplastic theories which are insufficient for accurately representing certain effects observed during experimental tests in Section 4.3. A novel constitutive model is proposed in the current chapter to address these limitations. This approach aims at bridging the gap between experimental observations and simulation results by introducing concepts of *offset-formulation* and *coating-formulation*. Out of the non-idealities seen in Section 4.3, the model developed in the current chapter aims at addressing the contact height tolerances as a material response. The tolerances in the profile bend may be addressed by capturing the geometric bending profiles of individual parts in ABAQUS and will be seen at a later stage.

5.1 Model requirements

The observations laid out at the end of Chapter 4 highlight the necessity for an effective material model that exhibits anisotropic elastoplastic behavior while accounting for: i) non-isochoric plasticity, ii) the variability in contact heights during mechanical loading and iii) the non-linear irreversible deformation of the soft coating layer. The following subsections will address these aspects individually.

5.1.1 Volumetric compressibility in the plastic domain

Several attempts to model volumetric compressibility in the plastic domain have been demonstrated in the literature, predominantly employing non-associative plasticity models. The primary difference between associative and non-associative approaches is, how internal variables are updated. In associative plasticity, the rate of change of internal variables is constrained to be normal to the yield surface, as dictated by the flow rule [145]. In contrast, non-associative plasticity does not imply normality, requiring a more generalized flow rule derived from a plastic flow potential, which may differ from the yield function. This gives non-associative models a purely phenomenological nature, where the second law of thermodynamics may not necessarily be enforced, and a variational structure may not always be formed.

This is not the case for associative models which maintain a variational structure and typically demonstrate an isochoric behavior within the plastic domain. However, plastic compressibility using an associative framework is demonstrated in some recent studies [138, 146, 147]. Xue & Hutchinson [147, 148] formulated a modified Hill criterion to account for plastic compressibility in the anisotropic framework which is briefly reviewed in this section. The widely used Hill criterion [149] for incompressible and orthotropic material models expresses the yield condition in the form:

$$\phi(\boldsymbol{\sigma}) = \sigma_{eq} - \sigma_0 = 0 \tag{5.1.1}$$

where, σ_0 is the effective yield stress and σ_{eq} is the equivalent stress defined as

$$\sigma_{eq} = \sqrt{\alpha_{12}(\sigma_{11}-\sigma_{22})^2 + \alpha_{23}(\sigma_{22}-\sigma_{33})^2 + \alpha_{13}(\sigma_{11}-\sigma_{33})^2 + 2\alpha_{44}\sigma_{12}^2 + 2\alpha_{55}\sigma_{23}^2 + 2\alpha_{66}\sigma_{31}^2} \tag{5.1.2}$$

with σ_{11}, σ_{22}, σ_{33}, σ_{12}, σ_{23} & σ_{13} being the stress components in the principal normal and shear directions. And α_{12}, α_{23}, α_{13}, α_{44}, α_{55} and α_{66} are dimensionless coefficients that define orthotropy. In Equation 5.1.2, it may be observed that the yield function does not depend on the hydrostatic stress components and has a plastic strain rate normal to yield surface causing volume incompressibility in the plastic domain.

In the work of Xue and Hutchinson [147], compressible anisotropic plasticity was introduced by creating a dependence of the effective stress on the hydrostatic stress components by adding three normal stress terms. The coefficients α_{11}, α_{22} and α_{33} create the dependence on the hydrostatic stress in conjunction with the assumption of normality, which gives rise to a volume change in the plastic domain. The other coefficients are identical

to those in the Hill criterion.

$$\begin{aligned} 2\sigma_{eff} = \alpha_{12}(\sigma_{11}-\sigma_{22})^2 + \alpha_{23}(\sigma_{22}-\sigma_{33})^2 + \alpha_{31}(\sigma_{33}-\sigma_{11})^2 \\ +6\alpha_{44}\sigma_{12}^2 + 6\alpha_{55}\sigma_{23}^2 + 6\alpha_{66}\sigma_{31}^2 + \alpha_{11}\sigma_{11}^2 + \alpha_{22}\sigma_{22}^2 + \alpha_{33}\sigma_{33}^2 \end{aligned} \tag{5.1.3}$$

The inclusion of the last three terms in Equation 5.1.3 addresses the concern of volume dilation within the plastic domain as demonstrated by Xue and Hutchinson [147].

5.1.2 Offset and coating formulations

It was seen in Section 4.3.3, that tolerances in the height dimension showed a significant effect on the contact pressure distribution after mechanical stacking. To understand this influence of height tolerances, let us consider two interconnect contacts in Figure 5.1(a) and Figure 5.1(b) with a difference of 25 μm in their height dimensions which are loaded uniaxially in the out-of-plane direction. Keeping the effective height of the representative volume constant, i.e., the distance between top and bottom plates, the homogenized stresses for the short contact σ_{zz}^{sc} and the tall contact σ_{zz}^{tc} are plotted in Figure 5.1(c). The shorter interconnect contact shows an offset in the stress-strain response on the strain axis and can be interpreted as a zone of zero stiffness until it contacts the plate above. From Figure 5.1(c) it is also evident that the magnitude of strain offset corresponds to the missing 25μm height dimension in Figure 5.1(b). This means that the geometric tolerances at individual contacts in the high-fidelity model can be represented in the form of a material response in the effective model. This is done by introducing a parameter called *offset-strain* which is the strain corresponding to the difference between the height dimension of the representative unit cell and of the measured interconnect contact.

Upon defining the offset strain, the idea may be extended for modeling the non linear coating behavior at the end of the offset domain. In this case, along with the offset representing the height variation, the coating is represented as a smooth transition from the offset domain to the elastic domain by using an exponential material law. The rheology for the material model is explained in the following section which highlights the different kinematic components in the system.

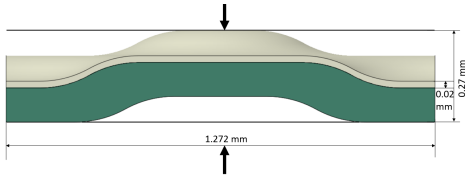

(a) Tall contact with coating.

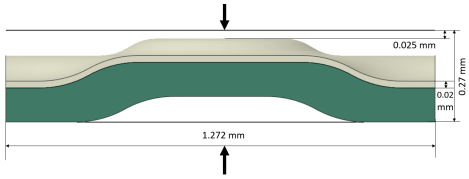

(b) Short contact with coating.

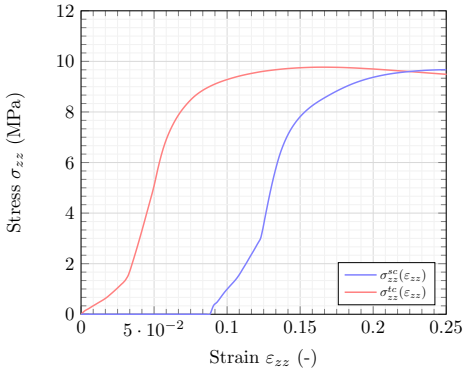

(c) Homogenized normal stress-strain responses.

Figure 5.1: Impact of height tolerances in interconnect contacts on the homogenized stress-strain response.

5.2 Rheology of the effective model

To represent the expected behavior outlined in Section 5.1, a one-dimensional rheological model is developed in this section. This model is used to define the desired material behavior in the out-of-plane direction and its structure is illustrated in Figure 5.2.

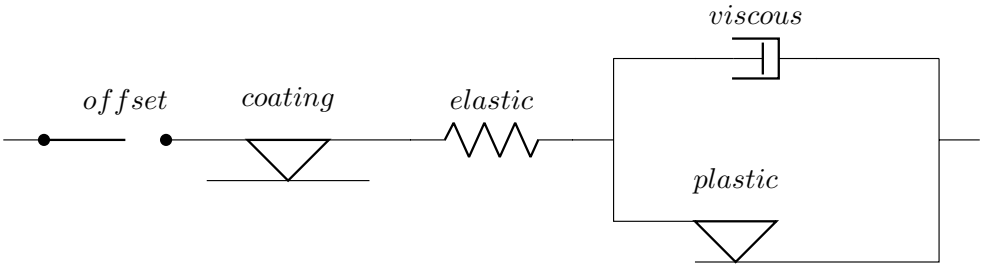

(a) Initial configuration ①

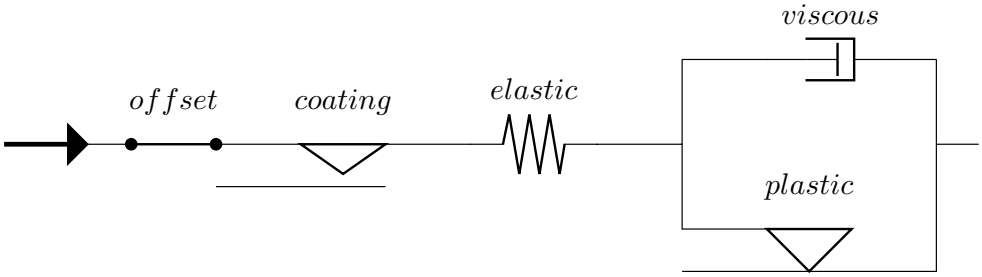

(b) Loading ②

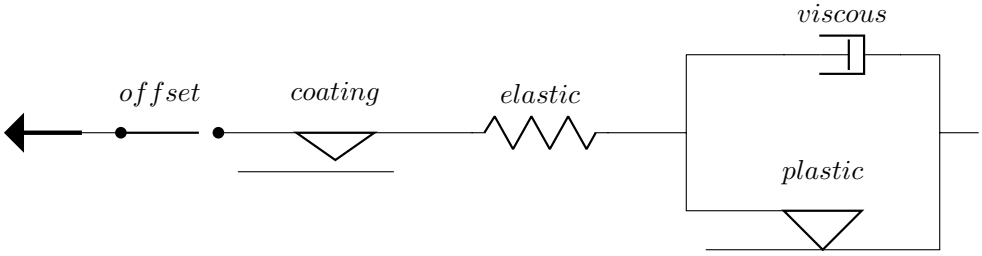

(c) Unloading ③

Figure 5.2: 1-D rheological model for material response

The model comprises of several kinematic components: an *offset* component, represented by an open link and a *coating* component modeled using a friction element. The fric-

tion element used for the porous coating material, progressively decays under compressive loading and eventually decouples from the system upon reaching saturation. Additionally, the *elastic* behavior is captured using a spring and the *plastic* behavior is represented by another friction element. To represent the *viscoplastic* effects over extended time scales, a damper is incorporated in parallel with the plastic friction element.

In the initial configuration, as shown in Figure 5.2(a) and denoted as state 1, the offset element is disengaged while the coating friction element is coupled with the system and the elastic spring remains unloaded. Both the plastic friction element and the viscous damper are in their initial positions. This setup corresponds to the stress-strain behavior observed at state 1 in Figure 5.3.

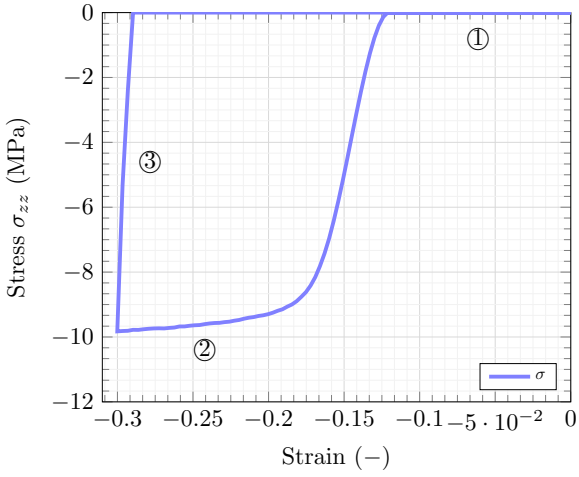

Figure 5.3: Material response to the rheological model

Upon the application of compressive loading, the system transitions to the configuration depicted in Figure 5.2(b). Initially, the offset element begins to close. Once a limiting strain is reached, the offset element becomes fully engaged allowing the coating friction element to slide and the elastic spring to compress. The friction within the coating element decreases exponentially as strain increases, and upon reaching a limiting compressive strain, the friction element saturates. Concurrently, the elastic spring continues to compress until its elastic limit is reached. Further compression causes the viscoplastic system, consisting of the friction element and damper, to change its configuration. This transition is represented by state 2 in the stress-strain plot shown in Figure 5.3, corresponding to the model in Figure 5.2(b).

During unloading, the model transitions from the configuration in Figure 5.2(b) to that in Figure 5.2(c), as a tensile load is applied to the system at state 2. As unloading begins, the compressed elastic spring starts to recover, while the plastic element remains in its deformed state. Once the spring is fully restored, additional tensile loading causes the offset element to open, resulting in no reactive force from the system. This state is depicted as unloading configuration 3 in Figure 5.3 and corresponds to the model shown in Figure 5.2(c).

5.3 Model Equations

Based on the rheological behavior outlined in Section 5.2, the model must be formulated mathematically through constitutive equations. These equations are derived from energy principles and must adhere to thermodynamic laws, consistent with the framework of associative plasticity. In this section, a set of constitutive equations are formulated to define the mechanical viscoplastic behavior of the rheological model outlined in Section 5.2 [150].

Basic kinematics and state variables

In a small strain setting, the total strain $\boldsymbol{\varepsilon}$ is additively decomposed into the stress producing elastic strain $\boldsymbol{\varepsilon}^e$ and the dissipative viscoplastic strain $\boldsymbol{\varepsilon}^{vp}$, as discussed in Section 2.2.4. However, to achieve the desired rheology stated in Figure 5.2, the total strain should additionally consist of offset strain $\boldsymbol{\varepsilon}^{of}$ and the coating strain $\boldsymbol{\varepsilon}^{co}$.

$$\boldsymbol{\varepsilon} = \boldsymbol{\varepsilon}^e + \boldsymbol{\varepsilon}^{of} + \boldsymbol{\varepsilon}^{co} + \boldsymbol{\varepsilon}^{vp} \tag{5.3.1}$$

where, the offset strain accounts for geometric variations in dimensions, as discussed in Section 5.1, while the coating strain models the nonlinear initial material response of the soft, porous coating layer, as outlined in Section 3.3.

Elastic response

The specific free energy for anisotropic elasticity is assumed to depend on the stress producing strain

$$\psi(\boldsymbol{\varepsilon}^e) = \frac{1}{2}\boldsymbol{\varepsilon}^e : \mathbf{C} : \boldsymbol{\varepsilon}^e \tag{5.3.2}$$

based on the elasticity tensor $\mathbf{C}$ which has minor and major symmetries $\mathbb{C}_{ijkl} = \mathbb{C}_{klij} = \mathbb{C}_{jikl} = \mathbb{C}_{ijlk}$. Exploitation of the dissipation inequality $\mathcal{D} = \boldsymbol{\sigma} : \dot{\boldsymbol{\varepsilon}} - \dot{\psi} \geq 0$ motivates the stress definition

$$\boldsymbol{\sigma} = \frac{\partial \psi}{\partial \boldsymbol{\varepsilon}^e} = \mathbf{C} : \boldsymbol{\varepsilon}^e \tag{5.3.3}$$

and the reduced form of the dissipation inequality can be expressed as

$$\mathcal{D} = \boldsymbol{\sigma} : \dot{\boldsymbol{\varepsilon}}^{of} + \boldsymbol{\sigma} : \dot{\boldsymbol{\varepsilon}}^{co} + \boldsymbol{\sigma} : \dot{\boldsymbol{\varepsilon}}^{vp} \geq 0 \tag{5.3.4}$$

that must be fulfilled for all deformation states. For subsequent analysis, we restrict ourselves to orthotropic elasticity, which takes the following form in Voigt notation

$$\mathbf{C} = \begin{bmatrix} \mathbb{C}_{11} & \mathbb{C}_{12} & \mathbb{C}_{13} & 0 & 0 & 0 \\ \mathbb{C}_{12} & \mathbb{C}_{22} & \mathbb{C}_{23} & 0 & 0 & 0 \\ \mathbb{C}_{13} & \mathbb{C}_{23} & \mathbb{C}_{33} & 0 & 0 & 0 \\ 0 & 0 & 0 & \mathbb{C}_{44} & 0 & 0 \\ 0 & 0 & 0 & 0 & \mathbb{C}_{55} & 0 \\ 0 & 0 & 0 & 0 & 0 & \mathbb{C}_{66} \end{bmatrix}. \tag{5.3.5}$$

Evolution of offset and coating strain

For the offset strain, representing the tolerances in the height dimension, we assume

$$\boldsymbol{\varepsilon}^{of} = \varepsilon^{of} \boldsymbol{N}^{of} \qquad \text{with} \qquad \boldsymbol{N}^{of} = \boldsymbol{e}_z \otimes \boldsymbol{e}_z \tag{5.3.6}$$

where $\boldsymbol{e}_z$ represents a unit normal basis vector in the out-of-plane direction, i.e., the direction of tolerances. The magnitude of compressive offset strain can be expressed as,

$$\varepsilon^{of} = \begin{cases} \tilde{\varepsilon}^{of}(\boldsymbol{\varepsilon}, \boldsymbol{\varepsilon}^{co}, \boldsymbol{\varepsilon}^{vp}) & \text{for } \tilde{\varepsilon}^{of}(\boldsymbol{\varepsilon}, \boldsymbol{\varepsilon}^{co}, \boldsymbol{\varepsilon}^{vp}) \leq \varepsilon^{of}_{tol}, \\ \varepsilon^{of}_{tol} & \text{otherwise.} \end{cases} \tag{5.3.7}$$

where the parameter $\varepsilon^{of}_{tol} < 0$ takes into account the geometric tolerances in the interconnect contact heights. The offset function considers inelastic deformations in the soft coating layer and viscoplastic deformations in the metal interconnect that may have occurred in the loading history

$$\tilde{\varepsilon}^{of}(\boldsymbol{\varepsilon}, \boldsymbol{\varepsilon}^{co}, \boldsymbol{\varepsilon}^{vp}) = (\boldsymbol{\varepsilon} - \boldsymbol{\varepsilon}^{co} - \boldsymbol{\varepsilon}^{vp}) : \boldsymbol{N}^{of} \tag{5.3.8}$$

Besides the offset strain correction, a coating strain is introduced that mimics the influence of a soft, porous coating material. Analogous to equation (5.3.6) we assume

$$\boldsymbol{\varepsilon}^{co} = \varepsilon^{co} \boldsymbol{N}^{co} \qquad \text{with} \qquad \boldsymbol{N}^{co} = \boldsymbol{e}_z \otimes \boldsymbol{e}_z \tag{5.3.9}$$

where $\boldsymbol{e}_z$ represents a unit normal basis vector in the out-of-plane direction (or direction of tolerance). The amount of compressive coating strain is governed by

$$\varepsilon^{co} = \min_{\tau\in[0,t]} \tilde{\varepsilon}^{co}_{\tau} \tag{5.3.10}$$

and can be regarded as a minimum equivalent strain measure obtained in a typical, possibly non-monotonic loading process. For the equivalent strain measure for the soft coating material we assume

$$\tilde{\varepsilon}^{co}(\boldsymbol{\varepsilon}) = -a\,\left(1 - \exp\left[b\,(\boldsymbol{\varepsilon} : \boldsymbol{N}^{co} - \varepsilon^{of}_{tol})\right]\right) \tag{5.3.11}$$

in terms of the material constants a and b.

Viscoplastic response

The evolution of the viscoplastic strain is assumed to have the following form

$$\dot{\boldsymbol{\varepsilon}}^{vp} = \dot{\varepsilon}^{vp}\boldsymbol{N}^{vp} \qquad \text{with} \qquad \boldsymbol{N}^{vp} = \mathbb{M} : \boldsymbol{\sigma}. \tag{5.3.12}$$

Here, the direction of anisotropic viscoplastic flow is governed by the Hill-type fourth order tensor $\mathbb{M}$ with the major and minor symmetries $\mathbb{M}_{ijkl} = \mathbb{M}_{klij} = \mathbb{M}_{jikl} = \mathbb{M}_{ijlk}$. According to the formulation defined by Xue & Hutchinson [147], reviewed in Section 5.1.1, a dependence of the effective stress on the hydrostatic stress components is considered by a Hill-type tensor which, in Voigt notation, takes the form

$$\mathbb{M} = \begin{bmatrix} \alpha_{12}+\alpha_{13}+\alpha_{11} & -\alpha_{12} & -\alpha_{13} & 0 & 0 & 0 \\ -\alpha_{12} & \alpha_{23}+\alpha_{12}+\alpha_{22} & -\alpha_{23} & 0 & 0 & 0 \\ -\alpha_{13} & -\alpha_{23} & \alpha_{13}+\alpha_{23}+\alpha_{33} & 0 & 0 & 0 \\ 0 & 0 & 0 & 6\,\alpha_{44} & 0 & 0 \\ 0 & 0 & 0 & 0 & 6\,\alpha_{55} & 0 \\ 0 & 0 & 0 & 0 & 0 & 6\,\alpha_{66} \end{bmatrix}. \tag{5.3.13}$$

The magnitude of viscoplastic flow is governed by

$$\dot{\varepsilon}^{vp} = \frac{\dot{E}_0}{\sigma_0}\left(\frac{\sigma^{eq}}{\sigma_0}\right)^{n-1} \qquad \text{with} \qquad \sigma^{eq} = \sqrt{\frac{1}{2}\boldsymbol{\sigma} : \mathbb{M} : \boldsymbol{\sigma}} \tag{5.3.14}$$

in terms of the material parameters $\dot{E}_0$, σ_0 and n. Incompressible isotropic plastic flow is recovered for $\mathbb{M} = \mathbb{P}$ with the fourth order deviatoric projection tensor $\mathbb{P} = \mathbb{I} - \frac{1}{3}\mathbf{1}\otimes\mathbf{1}$ and the fourth order identity tensor $\mathbb{I}_{ijkl} = \frac{1}{2}(\delta_{ik}\delta_{jl} + \delta_{jk}\delta_{il})$.

5.4 Algorithmic treatment of model equations

The constitutive equations described in the previous section need to be implemented into the finite element framework in the form of a numerically computable algorithm. Therefore, we consider a typical time-stepping procedure with process interval $[0, T]$. In this interval we are seeking the solutions at the discrete times $0, t_1, t_2, \ldots, t_n, t_{n+1}, \ldots, T$ where all field variables at time t_n are assumed to be known. Aiming at a compact notation, we drop in what follows the subscript t_{n+1} and consider all variables without subscript to be evaluated at time t_{n+1}. In a time discrete setting, the stresses are computed via

$$\boldsymbol{\sigma} = \mathbf{C} : \boldsymbol{\varepsilon}^e = \mathbf{C} : [\boldsymbol{\varepsilon} - \boldsymbol{\varepsilon}^{of}(\boldsymbol{\varepsilon}, \boldsymbol{\varepsilon}_n^{co}, \boldsymbol{\varepsilon}_n^{vp}) - \boldsymbol{\varepsilon}^{co}(\boldsymbol{\varepsilon}) - \boldsymbol{\varepsilon}^{vp}(\boldsymbol{\sigma}(\boldsymbol{\varepsilon}))] \tag{5.4.1}$$

The algorithmic counterpart of the offset strain formulation (5.3.8) reads

$$\varepsilon^{of} = \begin{cases} \tilde{\varepsilon}^{of}(\boldsymbol{\varepsilon}, \boldsymbol{\varepsilon}_n^{co}, \boldsymbol{\varepsilon}_n^{vp}) & \text{for } \tilde{\varepsilon}^{of}(\boldsymbol{\varepsilon}, \boldsymbol{\varepsilon}_n^{co}, \boldsymbol{\varepsilon}_n^{vp}) \leq \varepsilon_{tol}^{of}, \\ \varepsilon_{tol}^{of} & \text{otherwise.} \end{cases} \tag{5.4.2}$$

in terms of the time-discrete equivalent offset strain function

$$\tilde{\varepsilon}^{of}(\boldsymbol{\varepsilon}, \boldsymbol{\varepsilon}_n^{co}, \boldsymbol{\varepsilon}_n^{vp}) = (\boldsymbol{\varepsilon} - \boldsymbol{\varepsilon}_n^{co} - \boldsymbol{\varepsilon}_n^{vp}) : \boldsymbol{N}^{of} \tag{5.4.3}$$

in which a semi-implicit approach was chosen for the dependencies on the coating and viscoplastic strains. Similarly, the update of the amount of coating strain (5.3.10) follows by

$$\varepsilon^{co} = \begin{cases} \tilde{\varepsilon}^{co}(\boldsymbol{\varepsilon}) & \text{for } \tilde{\varepsilon}^{co}(\boldsymbol{\varepsilon}) \leq \varepsilon_n^{co}, \\ \varepsilon_n^{co} & \text{otherwise.} \end{cases} \tag{5.4.4}$$

where the irreversibility constraint for the coating strain is considered explicitly. The equivalent strain measure for the soft coating material reads

$$\tilde{\varepsilon}^{co}(\boldsymbol{\varepsilon}) = -a \left(1 - \exp\left[b\,(\boldsymbol{\varepsilon} : \boldsymbol{N}^{co} - \varepsilon_{tol}^{of})\right]\right). \tag{5.4.5}$$

The time-discrete counterpart of the evolution equation for the viscoplastic strain update (5.3.12) reads

$$\Delta\boldsymbol{\varepsilon}^{vp} = \Delta t \lambda(\boldsymbol{\sigma})\, \mathbb{M} : \boldsymbol{\sigma} \tag{5.4.6}$$

with $\lambda(\boldsymbol{\sigma})$ as the plastic multiplier defined by,

$$\lambda(\boldsymbol{\sigma}) = \frac{\dot{E}_0}{\sigma_0} \left(\frac{\sigma^{eq}}{\sigma_0}\right)^{n-1} \tag{5.4.7}$$

and σ^{eq} as the equivalent stress defined by a quadratic yield function using the 4^{th} order Hill-type tensor,

$$\sigma^{eq} = \sqrt{\frac{1}{2}\boldsymbol{\sigma} : \mathbb{M} : \boldsymbol{\sigma}}. \tag{5.4.8}$$

Reformulation of the stress update in equation (5.4.1) gives

$$\boldsymbol{\sigma} = \boldsymbol{\sigma}^{tr} - \mathbb{C} : \Delta\boldsymbol{\varepsilon}^{vp}(\boldsymbol{\sigma}) \tag{5.4.9}$$

with,

$$\boldsymbol{\sigma}^{tr} = \mathbb{C} : [\boldsymbol{\varepsilon} - \boldsymbol{\varepsilon}^{of}(\boldsymbol{\varepsilon}, \boldsymbol{\varepsilon}_n^{co}, \boldsymbol{\varepsilon}_n^{vp}) - \boldsymbol{\varepsilon}^{co}(\boldsymbol{\varepsilon}) - \boldsymbol{\varepsilon}_n^{vp}]. \tag{5.4.10}$$

where we introduced the trial stresses as a function of the total current strain and the coating and offset strains evaluated in a residual format and we obtain the nonlinear equation for the stresses

$$\boldsymbol{r}(\boldsymbol{\sigma}) := \boldsymbol{\sigma} - \boldsymbol{\sigma}^{tr} + \Delta t\, \lambda(\boldsymbol{\sigma})\, \mathbb{C} : \mathbb{M} : \boldsymbol{\sigma}. \tag{5.4.11}$$

This equation is solved using Newtons method with the following stress update

$$\boldsymbol{\sigma} \Leftarrow \boldsymbol{\sigma} + \Delta\boldsymbol{\sigma} \qquad \text{with} \qquad \Delta\boldsymbol{\sigma} = -\boldsymbol{r}(\boldsymbol{\sigma}) : \left[\frac{\partial \boldsymbol{r}}{\partial \boldsymbol{\sigma}}\right]^{-1} \tag{5.4.12}$$

until convergence is obtained in the sense of $\|\boldsymbol{r}(\boldsymbol{\sigma})\| \leq tol$. The required tangent reads

$$\frac{\partial \boldsymbol{r}}{\partial \boldsymbol{\sigma}} = \mathbb{I}^s + \Delta t \left[\frac{\partial \lambda}{\partial \sigma^{eq}} \mathbb{M} : \boldsymbol{\sigma} \otimes \mathbb{C} : \mathbb{M} : \boldsymbol{\sigma} + \lambda\, \mathbb{C} : \mathbb{M}\right] \tag{5.4.13}$$

where,

$$\frac{\partial \lambda}{\partial \sigma^{eq}} = \frac{(n-1)\dot{E}_0}{\sigma_0^2} \left(\frac{\sigma^{eq}}{\sigma_0}\right)^{n-2}. \tag{5.4.14}$$

If convergence of the local Newton iteration has been achieved, the viscoplastic strain can be updated

$$\boldsymbol{\varepsilon}^{vp} = \boldsymbol{\varepsilon}_n^{vp} + \Delta t\, \lambda(\boldsymbol{\sigma})\, \mathbb{M} : \boldsymbol{\sigma} \tag{5.4.15}$$

and the material tangent, required in a finite element context, can be calculated

$$\frac{\partial \boldsymbol{\sigma}}{\partial \boldsymbol{\varepsilon}} = \mathbb{C} : \left[\mathbb{I}^s - \frac{\partial \boldsymbol{\varepsilon}^{of}}{\partial \boldsymbol{\varepsilon}} - \frac{\partial \boldsymbol{\varepsilon}^{co}}{\partial \boldsymbol{\varepsilon}}\right] : \left[\frac{\partial \boldsymbol{r}}{\partial \boldsymbol{\sigma}}\right]^{-1} \tag{5.4.16}$$

containing the derivatives related to the offset and coating strains

$$\frac{\partial \boldsymbol{\varepsilon}^{of}}{\partial \boldsymbol{\varepsilon}} = \begin{cases} \boldsymbol{N}^{of} \otimes \boldsymbol{N}^{of} & \text{for } \tilde{\varepsilon}^{of}(\boldsymbol{\varepsilon}, \boldsymbol{\varepsilon}_n^{co}, \boldsymbol{\varepsilon}_n^{vp}) \leq \varepsilon_{tol}^{of}, \\ \mathbb{0} & \text{otherwise.} \end{cases} \tag{5.4.17}$$

and

$$\frac{\partial \boldsymbol{\varepsilon}^{co}}{\partial \boldsymbol{\varepsilon}} = \begin{cases} a\, b\, \exp\left[b\,(\boldsymbol{\varepsilon} : \boldsymbol{N}^{co} - \varepsilon_{tol}^{of})\right]\, \boldsymbol{N}^{co} \otimes \boldsymbol{N}^{co} & \text{for } \tilde{\varepsilon}^{co}(\boldsymbol{\varepsilon}) \leq \varepsilon_n^{co}, \\ \mathbb{0} & \text{otherwise.} \end{cases} \tag{5.4.18}$$

5.5 Incorporation into the finite element framework

The phenomenon of contact height tolerances and coating behavior observed in Section 5.1.2, which represent the offset and coating formulations are first expressed in the form of constitutive laws in Section 5.3. Subsequently, the constitutive equations defined are expressed in the algorithmic form in Section 5.4. This algorithmic framework is implemented in FORTRAN which may be visualized with the flow chart in Figure 5.4. On appropriate implementation, the constitutive model described in this chapter is introduced in the finite element solver ABAQUS as a user material (UMAT) subroutine. After calibration of suitable material parameters, this model may be fitted to the homogenized behavior of a coated interconnect contact to show its equivalent effective response.

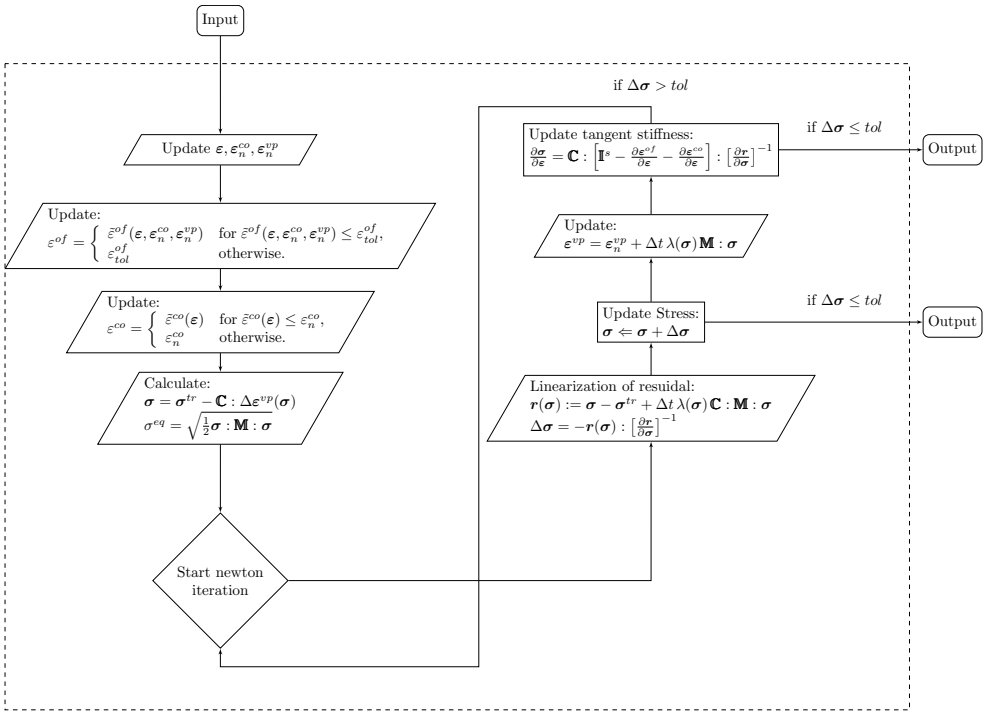

Figure 5.4: Algorithmic representation of constitutive model

5.6 Characteristics of the effective model

In this Section, the mechanical behavior of the effective model is discussed for several loading cases. As defined in Section 4.2.4, a block geometry with dimensions identical to the high-fidelity model, i.e., 1.272 mm x 1.272 mm x 0.27 mm, is investigated using nominal material parameters. A compressive strain rate of $0.3s^{-1}$ was assumed in the out-of-plane direction and a tensile strain rate of $0.008s^{-1}$ was assumed in the in-plane direction in their corresponding loading cases. The geometry was discretized using one C3D8 element with uniaxial and biaxial loading states applied to explain the main features of the model.

The material model was first tested for the offset formulation, with and without coating behavior, under uniaxial compression in the out-of-plane direction. The stress-strain response for this test is plotted in Figure 5.5(a). For the pure offset formulation, it is seen that, despite there being some strain in the element, the stress response ($\sigma_{zz}^{w/o\ co}$) is zero until a limiting strain threshold of about $\varepsilon_{zz} = 0.12$. When the strain in the element exceeds this threshold value, the material shows a typical elastoplastic response. For the offset and coating formulation, the stress response ($\sigma_{zz}^{w/\ co}$) can be characterized with a smooth exponential transition into the elastic domain and is also plotted in Figure 5.5(a).

The effect of the offset and coating formulation for a uniaxial loading in the in-plane direction is seen in Figure 5.5(b). The offset or coating parameters do not influence the in-plane behavior for a uniaxial loading case suggesting that the formulation developed in Section 5.3 does not cause any unforeseen effects in other directions for the uniaxial loading case.

The offset and coating formulation was then tested for a biaxial loading case using the same geometry under a normal loading in-plane and out-of-plane simultaneously with the mentioned strain rates. Figure 5.5(c) shows the stress-strain response over time for the simultaneous loading in in-plane and out-of-plane directions. In the offset domain, stress response in the in-plane direction is same as the uniaxial case in Figure 5.5(b). However, at the end of the offset domain, there is a decrease in the yield stress which depicts a typical biaxial loading behavior. This infers that the loading in the offset domain gives a stress response equivalent to the uniaxial loading case in the in-plane direction. But when the strain exceeds the offset threshold, the model shows a typical biaxial loading stress response.

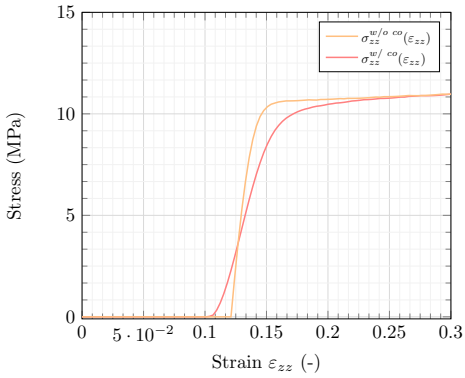

(a) Monotonic uniaxial out-of-plane load ε_{zz}.

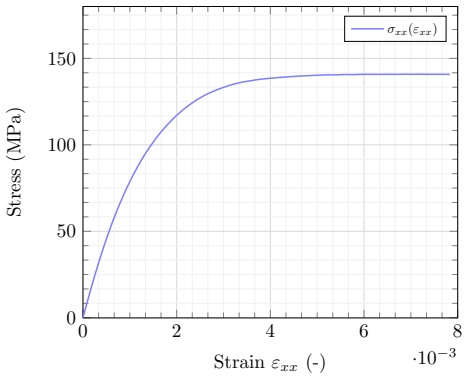

(b) Monotonic uniaxial in-plane load ε_{xx}.

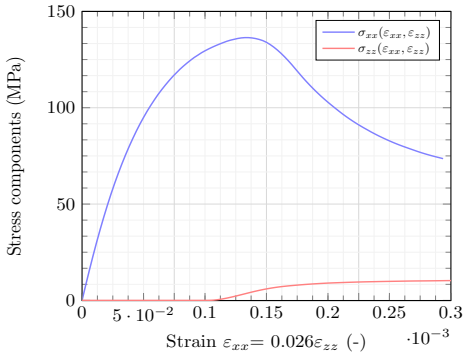

(c) Biaxial in-plane (ε_{xx}, ε_{yy}) and out-of-plane (ε_{xx}, ε_{zz}) load.

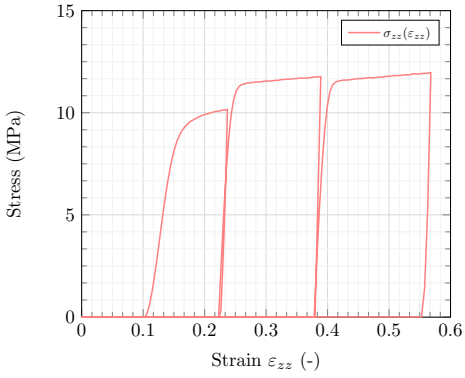

(d) Cyclic uniaxial out-of-plane load.

Figure 5.5: Characteristics of effective model: Offset and coating formulation under several loading cases.

The loading-unloading behavior was plotted in Figure 5.5(d) for a uniaxial loading in the out-of-plane direction for three consecutive cycles. It was observed that there was a recovery of the elastic strain after each cycle, however, the offset-strain, coating-strain and plastic-strain was non-recoverable at zero stresses. It may also be noted that this formulation permits only compressive loading in the out-of-plane direction.

5.7 Incorporation of thermal aspects

In the previous sections, a finite element framework was developed to model the mechanical behavior of the coated interconnect at room temperature which accounts for dimensional tolerances. However, in practical applications, SOCs operate at temperatures of about 600°C where the contact configuration determined at room temperature can change significantly due to temperature-driven factors such as thermal expansion, temperature-dependent material moduli, and creep/relaxation. While the current elasto-viscoplastic model is already equipped to simulate rate-dependent phenomena like creep and relaxation, a set of additional constitutive equations must be incorporated to consider effects of temperature variation. In the following sections, the model equations defined in Section 5.3 are extended to represent thermal expansion and the temperature dependence of the elastoplastic moduli which would equip the effective model to simulate the required loading steps for the SOC contact life-cycle [151].

Within a thermomechanical setting, the specific Helmholtz free energy ψ is considered to be a function of the elastic strain and temperature,

$$\psi = \psi(\boldsymbol{\varepsilon}^e, T) \tag{5.7.1}$$

which may be expressed in the form of its time derivative as,

$$\dot{\psi}(\boldsymbol{\varepsilon}^e, T) = \frac{\partial \psi}{\partial \boldsymbol{\varepsilon}^e} : \dot{\boldsymbol{\varepsilon}^e} + \frac{\partial \psi}{\partial T} : \dot{T} \qquad \text{where} \qquad \eta = -\frac{\partial \psi}{\partial T} \tag{5.7.2}$$

where η is the entropy related to the free energy and Equation 5.7.2 may be expressed as,

$$\dot{\psi}(\boldsymbol{\varepsilon}^e, T) = \frac{1}{2}\boldsymbol{\varepsilon}^e : \mathbf{C} : \boldsymbol{\varepsilon}^e - \eta \dot{T} \tag{5.7.3}$$

The Clausius-Duhem inequality defines positive local dissipation $\mathcal{D}$ for a thermomechanical problem without heat generation as

$$\mathcal{D} = \boldsymbol{\sigma} : \dot{\boldsymbol{\varepsilon}} - \dot{\psi} - \eta \dot{T} \geq 0 \tag{5.7.4}$$

then, on excluding the recoverable energies in the system, the dissipation inequality is reduced to the form,

$$\mathcal{D} = \boldsymbol{\sigma} : \dot{\boldsymbol{\varepsilon}}^{of} + \boldsymbol{\sigma} : \dot{\boldsymbol{\varepsilon}}^{co} + \boldsymbol{\sigma} : \dot{\boldsymbol{\varepsilon}}^{vp} \geq 0 \tag{5.7.5}$$

that must be fulfilled for all deformation states.

5.7.1 Thermal expansion

While considering varying temperatures, a temperature dependent thermal strain may be introduced which has a purely dilatational response and does not cause any shear. It may be expressed in Voigt notation as follows,

$$\boldsymbol{\varepsilon}^{th} = \boldsymbol{\alpha}^{th} \Delta T \qquad \text{with} \qquad \boldsymbol{\alpha}^{th} = \begin{bmatrix} \alpha_{11}^{th} \\ \alpha_{22}^{th} \\ \alpha_{33}^{th} \\ 0 \\ 0 \\ 0 \end{bmatrix} \qquad \text{and} \qquad \Delta T = T - T_0 \tag{5.7.6}$$

$\boldsymbol{\alpha}^{th}$ is a second order tensor representing the anisotropic coefficients of thermal expansion in the Voigt notation, where α_{11}^{th} and α_{22}^{th} describe the thermal expansion behavior in the in-plane direction and α_{33}^{th} describes the thermal expansion in the out-of-plane direction, T is the temperature of the system at time t and T_0 is the reference temperature.

While considering temperature change in the system, the total strain $\boldsymbol{\varepsilon}^{tot}$ may comprise of the mechanical strain additively coupled with the thermal strains. The corresponding mechanical strains may be expressed as,

$$\boldsymbol{\varepsilon} = \boldsymbol{\varepsilon}^{tot} - \boldsymbol{\varepsilon}^{th} \tag{5.7.7}$$

where, $\boldsymbol{\varepsilon}$ represents the total mechanical strain and $\boldsymbol{\varepsilon}^{th}$ represents the thermal strain in Equation 5.7.6. Here, the thermal strain is fully recoverable and may be computed as a function of the change in temperature which is a prescribed boundary condition.

5.7.2 Temperature dependent moduli

The moduli of the orthotropic elasticity tensor and Hill-type plasticity tensor are temperature dependent parameters and may vary over large range of temperatures. This may

be approximated by linearly interpolating the tensor coefficients between discrete known temperature intervals.

If the temperature $T \in [T^n, T^{n+1}]$, where n and $n+1$ is the temperature interval having tensor properties $\mathbb{A}$ with components $\mathbb{A}_{ijkl}$, the corresponding tensor coefficients may be assumed by linear interpolation and are given by

$$\frac{T - T^n}{T^n - T^{n+1}} = \frac{\mathbb{A}_{ijkl} - \mathbb{A}^n_{ijkl}}{\mathbb{A}^n_{ijkl} - \mathbb{A}^{n+1}_{ijkl}} \tag{5.7.8}$$

where, $\mathbb{A}^n_{ijkl}$ corresponds to the tensor coefficients at temperature T^n and $\mathbb{A}^{n+1}_{ijkl}$ corresponds to the tensor coefficients at temperature T^{n+1}. The components of orthotropic elastic tensor $\mathbb{C}$ and Hill-type plasticity tensor $\mathbb{M}$ may be interpolated using this approach between given discrete temperature ranges.

5.7.3 Implementation of thermal effects in the finite element framework

On considering the effects of thermal loading in the model, a thermal strain is introduced which is coupled with the total strain and determines the thermal effects in the model. The model equations defined in Section 5.7.1 may be used to determine the total mechanical strain $\boldsymbol{\varepsilon}$, is explicitly coupled to the workflow as derived in Section 5.3 as well as the algorithmic treatment in Section 5.4. The temperature dependence of moduli is achieved by linearly interpolating the coefficients of the orthotropic elasticity tensor $\mathbb{C}$ and Hill-type plasticity tensor $\mathbb{P}$ between discrete temperature ranges at the start of each time increment in the algorithmic setting. This is stated in Section 5.7.2.

The implementation in the algorithm including the aforementioned modifications are introduced in the flowchart in Figure 5.6.

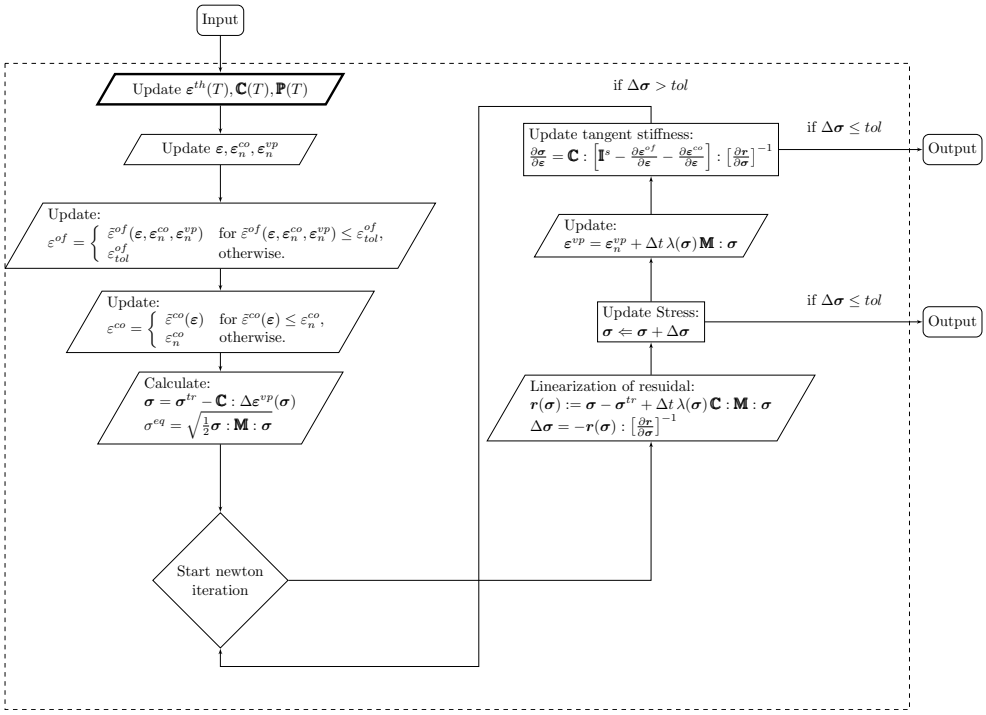

Figure 5.6: Algorithmic representation of constitutive model with temperature dependence

5.7.4 Characteristics for thermal and relaxation behavior

The thermal and relaxation effects are evaluated in the out-of-plane direction, as this is the primary direction of loading contributing to electrical contact resistance.

After applying mechanical loading to an effective block model with dimensions identical to the high-fidelity RVE model (i.e., 1.272 mm x 1.272 mm x 0.27 mm), the deformation was kinematically constrained and subjected to thermal loading from 25°C to 600°C. The resulting stress-temperature relation is plotted in Figure 5.7(a). This relationship considers the effects of thermal expansion and temperature dependence of moduli and shows similar characteristics to the homogenized model in Section 4.2.2.

In order to investigate the viscous characteristics of the model, the effective block model was held at the elevated temperature for a period of 10^4 s. The corresponding stress relax-

ation over time is plotted in Figure 5.7(b). The stress-time response obtained for the block model closely aligns with the behavior of the results from computational homogenization discussed in Section 4.2.3.

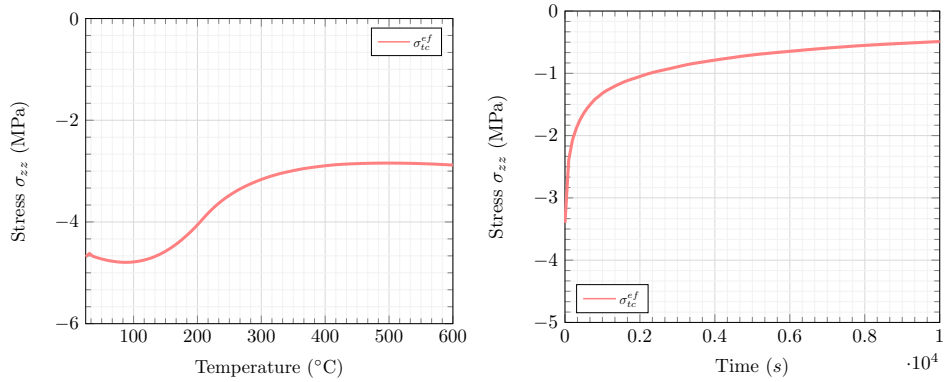

(a) Stress-temperature relation for thermal loading

(b) Stress-time relation during relaxation

Figure 5.7: Characteristics of the effective model at operational temperatures

5.8 Summary

The manufacturing non-idealities discussed in Chapter 4 showed two types of tolerances: bending profile tolerances and contact height tolerances. Bending profile tolerances may be addressed within the homogenization approach by geometrically representing the bending profiles of individual components. Contact height tolerances pose a challenge, as accounting for them geometrically is not feasible using conventional models. Therefore, this chapter focused on developing an appropriate effective material model to account for dimensional tolerances at the contact. To do so, offset and coating formulations were introduced which incorporated the dimensional tolerances and the porous coating behavior for a rate-dependent mechanical loading. The necessary constitutive equations were derived and implemented in an algorithmic framework for finite element analysis. This algorithm was subsequently modified to account for thermal effects.

With these developments, the finite element framework required to model dimensional tolerances in SOC contacts throughout their lifecycle is complete. In the next chapter, model

parameters are calibrated and the model is validated against high-fidelity simulations for a grid of contacts representing the active area of the interconnect.

6 Computational investigation and validation

In the previous chapters, a constitutive anisotropic viscoplastic material model was developed which represents the desired rheology for the effective model. The characteristics of this model include non-isochoric plasticity, offset formulation representing variability in height dimension as a material response and the coating formulation representing a porous coating layer. These features along with elastoviscoplastic behavior were incorporated in the finite element framework in an algorithmic setting which is aimed to represent the SOC contacts in the form of an effective model.

To achieve this, in this chapter, first the effective parameters for the constitutive model are calibrated. On obtaining the model parameters, the effective model is tested for accuracy in comparison with its high-fidelity counterpart. This comparison determines how closely the effective model may represent the high-fidelity model. Finally, the degree of accuracy with computational time reduction is demonstrated in this chapter.

As previously defined, the computational investigations are formulated into three process steps for which the effective model will be investigated:

- Assembly at room temperature during which is subjected to mechanical loading
- Temperature ramp-up subjecting it to thermal loading.
- Relaxation at operational temperature over long periods of time.

6.1 Assembly at room temperature

In this Section, the concepts developed for the offset and coating formulation are implemented to explain the variability in stress distribution created by the contact tolerances.

6.1.1 Parameter Identification

The effective constitutive model developed in Chapter 5 is calibrated to the homogenized responses for a steady state strain rate of 0.25 s^{-1} out-of-plane and 0.03 s^{-1} in-plane. These strain rates were calculated based on a routine for stack compression. However, in practice, the model may be calibrated with any strain rates determined from the experimental stacking process and is an input parameter.

Figure 6.1(d) shows the effective stress-strain response of uniaxial normal loading for a tall and short contact in the out-of-plane direction fitted to its homogenized response. Figures 6.1(a), 6.1(b) and 6.1(c) show the fitting of the effective model for remaining normal and shear loading cases in-plane and out-of-plane.

Similarly, the volume dilation for uniaxial normal loading cases in-plane and out-of-plane are also plotted in Figure 6.1. Figure 6.1(e) shows the effective strain components $\varepsilon_{yy}(\varepsilon_{xx})$ and $\varepsilon_{zz}(\varepsilon_{xx})$ fitted onto the high-fidelity homogenized model for a normal in-plane loading ε_{xx}. Figure 6.1(f) shows the effective strain components $\varepsilon_{xx}(\varepsilon_{zz})$ and $\varepsilon_{yy}(\varepsilon_{zz})$ fitted onto the high-fidelity homogenized model for a normal out-of-plane loading ε_{zz}.

The input properties for the effective model consists of an orthotropic elasticity tensor $\mathbb{C}$, a Hill-type plasticity tensor $\mathbb{M}$ and the viscoplastic coefficients $\dot{\epsilon}_0$, σ_0 and n, the limiting offset strain ϵ^{of}_{tol} and the coefficients for the coating strain a and b.

Table 6.1: Anisotropic input parameters for the effective model obtained from fit to homogenized response.

(a) Elasticity.

Elastic coefficients (MPa)	
$\mathbb{C}_{11}$	52000
$\mathbb{C}_{12}$	0
$\mathbb{C}_{13}$	0
$\mathbb{C}_{22}$	52000
$\mathbb{C}_{23}$	0
$\mathbb{C}_{33}$	650
$\mathbb{C}_{44}$	10000
$\mathbb{C}_{55}$	750
$\mathbb{C}_{66}$	750

(b) Viscoplasticity.

Hill-type coefficients (-)	
α_{11}	48.5
α_{12}	-19.5
α_{13}	0
α_{22}	200
α_{23}	0
α_{33}	3475
α_{44}	33.33
α_{55}	$408.33(tc), 466.667(sc)$
α_{66}	$408.33(tc), 466.667(sc)$

Table 6.1 summarizes the identified elastic and viscoplastic coefficients. Parameters for

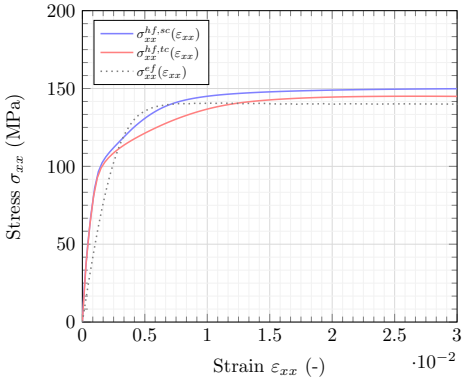

(a) In-plane normal

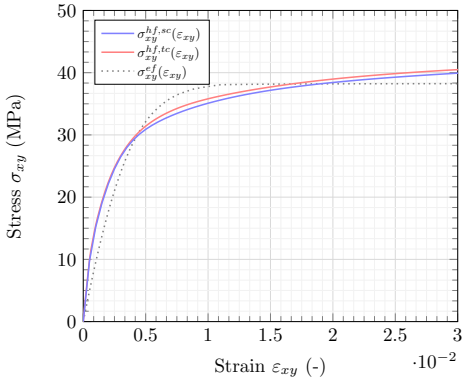

(b) In-plane shear

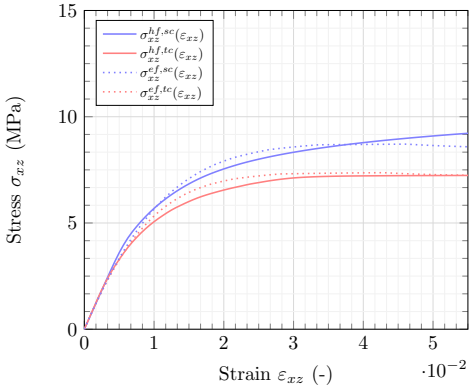

(c) Out-of-plane shear

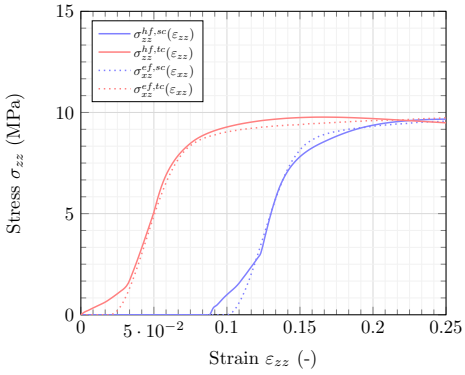

(d) Out-of-plane normal

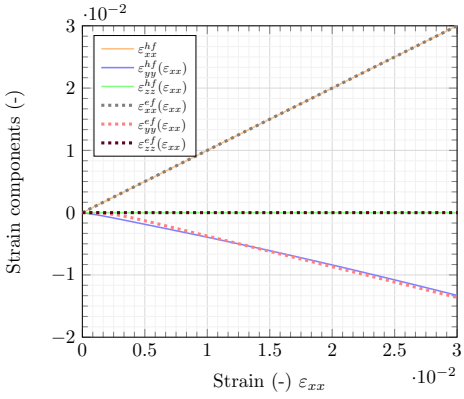

(e) Volume dilation (ε_{xx},ε_{yy}) for uniaxial normal in-plane loading (ε_{xx})

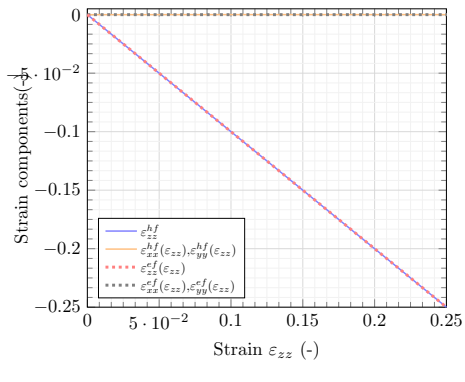

(f) Volume dilation (ε_{xx},ε_{yy}) for uniaxial normal out-of-plane loading (ε_{zz})

Figure 6.1: Parameter identification based on four basic deformation modes and volume dilation.

Table 6.2: Input parameters for the effective model obtained from fit to homogenized response.

(a) Viscoplasticity.

Initial strain rate (-)	
$\dot{\epsilon}_0$	0.00253602
Initial stress (MPa)	
σ_0	244.81
Exponent (-)	
n	1.55

(b) Tall contact.

Offset strain (-)	
$\varepsilon_{tol}^{of,tc}$	0.02
Coating thickness (mm)	
a^{tc}	0.04
Coating stiffness (MPa)	
b^{tc}	26.0

(c) Short contact.

Offset strain (-)	
$\varepsilon_{tol}^{of,sc}$	0.11
Coating thickness (mm)	
a^{sc}	0.04
Coating stiffness (MPa)	
b^{sc}	26.0

the viscoplastic response and parameters for the offset and coating strain for the tall and short contacts are summarized in Table 6.2.

6.1.2 Mechanical validation for 1-Layer: 16 Contacts

In order to validate the model, the effective model was compared to a high-fidelity simulation. The two coated contacts introduced and homogenized in Section 5.1 were used to create a grid of 16 contacts of two different height dimensions.

Their heights were 25 μm apart and were positioned at random locations in the grid. An effective model was constructed replacing the contacts by brick elements with same positions for tall and short contacts in the effective and high-fidelity models. The material properties for the effective model was taken from Section 6.1.1. Both models were compressed between rigid plates with the strain rates given in Section 6.1.1 and were constrained in-plane at their edges. Figure 6.2(a) and Figure 6.2(b) show the stress concentration in the high-fidelity model and effective model in the $zz-direction$. The tall contacts exhibited larger stresses in the $zz-direction$ and upon undergoing deformation of about 25 μm, the shorter contacts began to deform. Figure 6.2(c) shows the force-displacement curves from the compression simulations of the high-fidelity and effective models which show a good alignment. The accuracy of the effective model may be quantified to have an R-square value of 0.9917 in reference to the high-fidelity model. The effective model had a significantly reduced simulation time which was compared with the high-fidelity case. The high-fidelity model required 48 parallel CPUs on the high performance cluster and took about 28 hours, whereas the effective model took about 30

seconds on a standard workstation desktop. This shows that the effective model is capable of successfully simulating variability in the height dimension of contacts on an SOC interconnect as well as non-linear coating behavior.

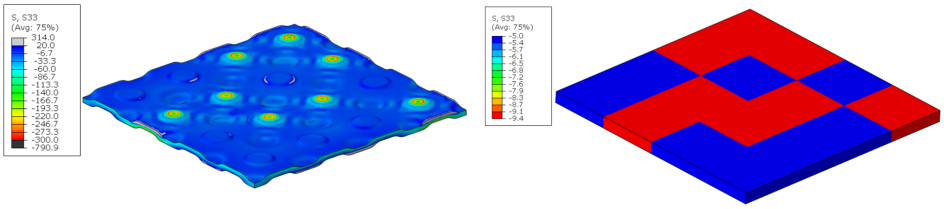

(a) High-fidelity model (b) Effective model

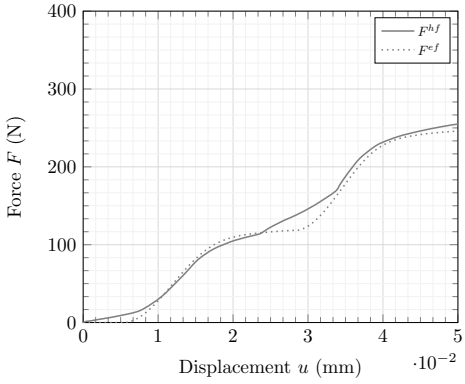

(c) Force-Displacement on 1-Layer: 16 contacts

Figure 6.2: Numerical validation for a 1-Layer interconnect

6.1.3 Mechanical validation for 2-Layer: 16 Contacts

In the previous section, the effective model was validated for the compression of a single interconnect layer. In this section, the repeatability of results for a multilayered stack was tested. The coated interconnect contacts of two height dimensions from the previous section were reused, however, one layer was rotated by 180 degrees to create a variability in the location of tall and short contacts in the two layers. Two such interconnects were stacked together separating each other with rigid plates. The effective model was constructed in a similar way as discussed in the previous subsection. The material properties for tall and short contacts and the loading conditions were same as for the 1-Layer test and evaluated in Section 6.1.1. Figure 6.3(a) and Figure 6.3(b) show the stress concentration

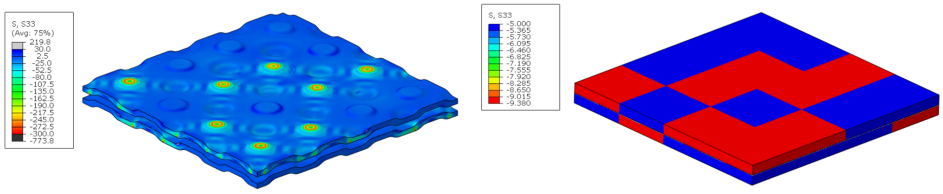

(a) High-fidelity model (b) Effective model

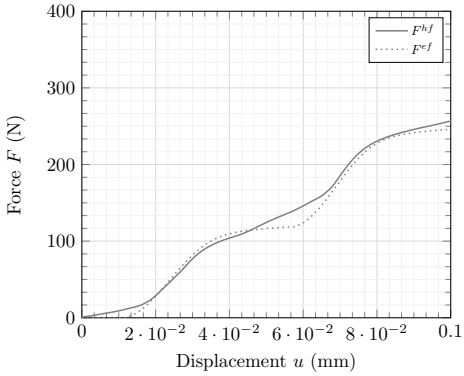

(c) Force-Displacement on 2-Layers: 16 contacts

Figure 6.3: Numerical validation for a 2-Layer interconnect

in the high-fidelity model and effective model. Figure 6.3(c) shows the force-displacement curves from the compression simulations. The accuracy of the effective model may be quantified to have an R-square value of 0.9827 in reference to the high-fidelity model. It may be noted that on increasing the number of layers, the effective model consistently represents the high-fidelity model.

Based on the results seen in Figure 6.2(c) and Figure 6.3(c), it may be noticed that the effective model represents the high-fidelity model with the accuracy quantified in terms of the R-square value stated in both cases. Considering the reduction in simulation time of several orders of magnitude, the given accuracy of the model may be seen as a good compromise. Moreover, the model accuracy is dependent on the parameter fitting done in Section 6.1.1 and can be better fitted if a higher level of accuracy is desired.

6.2 Temperature ramp-up

After mechanical assembly at room temperature the SOC stack is heated up to operational temperatures. This section focuses on investigating the combined impact of temperature-dependence of elastoplastic moduli and thermal expansion behavior on the dimensional variances in the high-fidelity model. Then, the effective model is calibrated with suitable parameters. Lastly, a comparison is done for a large grid of contacts between the high-fidelity and effective model configurations.

6.2.1 Parameter Identification

In order to visualize the effects of dimensional variability, interconnect contacts with two height dimensions, 3 μm apart in the out-of-plane direction are considered. The tall contact is shown in Figure 6.4(a) and the short contact is shown in Figure 6.4(b). Both contacts are subjected to periodic boundary conditions as mentioned in Chapter 4 and loaded mechanically in the out-of-plane direction representing the stack compression process. These contacts are then held in this configuration and subjected to a temperature increase from 25°C to 600°C.

The out-of-plane stress σ_{zz}^{hf} for the high-fidelity model during mechanical loading is plotted in Figure 6.4(c). At the end of the loading step, it may be noticed that the tall contact has a larger homogenized stress-state than the short contact. This indicates that within

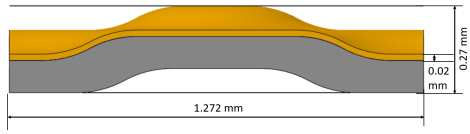

(a) Tall contact with coating

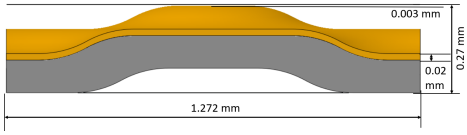

(b) Short contact with coating

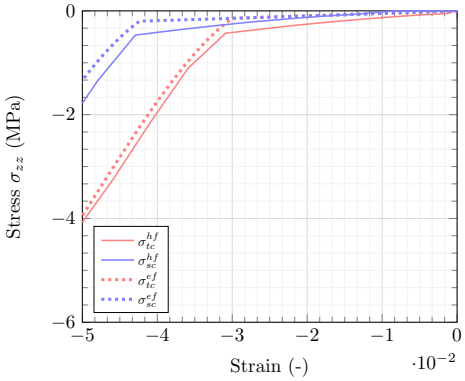

(c) Stress-Strain response for tall and short contacts in the high-fidelity and effective models

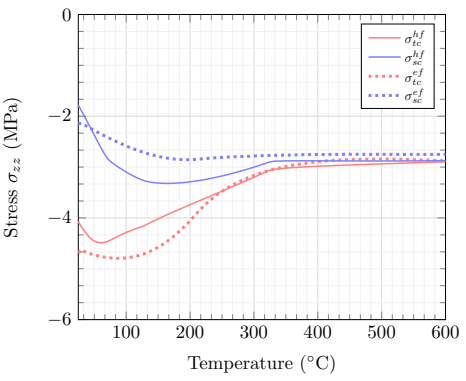

(d) Stress-Temperature response for tall and short contacts in the high-fidelity and effective models

Figure 6.4: Temperature ramp-up behavior for contacts with variability in height dimensions

the elastic domain, the height variance is proportional to the homogenized stress σ^{hf}_{zz}, however, with the onset of plasticity, both contacts may eventually reach the same final stress configuration. Using this response, the effective model is then calibrated after being subjected to the same boundary conditions as the high-fidelity model. The fitting of effective stresses σ^{ef}_{zz} to the homogenized stress σ^{hf}_{zz} response over strain is shown in Figure 6.4(c) for both contacts.

Table 6.3 summarizes the fitted orthotropic elastic and Hill-type viscoplastic coefficients in the effective model. Table 6.4 summarizes the rate dependent coefficients along with offset and coating parameters for the tall and short contacts.

It may be noted that, the primary loading during stacking is always in the out-of-plane direction. Due to this and the in-plane yield limit being much greater than the out-of-plane yield limit, it may be safe to assume in-plane elasticity for the effective model. This may be done by setting other components of the Hill-type tensor to zero and is seen in Table 6.3

Table 6.3: Anisotropic input parameters for the effective model obtained from fitting homogenized response.

(a) Elasticity

Elastic coefficients (MPa)	
$\mathbb{C}_{11}$	52000
$\mathbb{C}_{12}$	0
$\mathbb{C}_{13}$	0
$\mathbb{C}_{22}$	52000
$\mathbb{C}_{23}$	0
$\mathbb{C}_{33}$	650
$\mathbb{C}_{44}$	10000
$\mathbb{C}_{55}$	750
$\mathbb{C}_{66}$	750

(b) Viscoplasticity

Hill coefficients (-)	
α_{11}	0
α_{12}	0
α_{13}	0
α_{22}	0
α_{23}	0
α_{33}	$\bar{\alpha_{33}}$
α_{44}	0
α_{55}	0
α_{66}	0

After bringing the homogenized interconnect contacts to the mechanically compressed configuration, the high-fidelity model of the tall and short contacts are subjected to a temperature loading and the stress σ^{hf} is plotted over temperature in Figure 6.4(d). It is seen in Figure 6.4(d) that there is a different rate of yielding for both contacts. This is primarily due to different final configuration of stress states after mechanical loading which in turn maybe traced back to the difference in their height dimensions. This suggests that the evolution of plastic flow during temperature loading is somehow dependent on the variability of height dimension.

The orthotropic elastic tensor component does not change significantly with temperature in this case. However, the evolution of the Hill-type plasticity tensor component $\bar{\alpha_{33}}$ with temperature for the tall contact $\bar{\alpha_{33}^{tc}}$ and the short contact $\bar{\alpha_{33}^{sc}}$ are shown in Table 6.5. For all temperatures in between the stated values, the corresponding $\bar{\alpha_{33}}$ may be linearly interpolated. While application to a large range of varying height dimensions, the Hill-type coefficients $\bar{\alpha_{33}}$ may be calibrated for several height values in the tolerance domain and may be interpolated for the ones in between.

6.2.2 Thermal validation for 1-Layer: 16 Contacts

In order to validate the effects of dimensional variance seen during temperature ramp-up in the effective model, it may be compared to its corresponding high-fidelity counterpart.

Table 6.4: Input parameters for the effective model obtained from fit to homogenized response.

(a) Viscoplasticity.

Initial strain rate (-)	
$\dot{\epsilon}_0$	0.00253602
Initial stress (MPa)	
σ_0	244.81
Exponent (-)	
n	1.55

(b) Tall contact.

Offset strain (-)	
$\varepsilon_{tol}^{of,tc}$	0.025
Coating thickness (mm)	
a^{tc}	0.02
Coating stiffness (MPa)	
b^{tc}	40.0

(c) Short contact.

Offset strain (-)	
$\varepsilon_{tol}^{of,sc}$	0.036
Coating thickness (mm)	
a^{sc}	0.02
Coating stiffness (MPa)	
b^{sc}	40.0

(d) Thermal expansion

Thermal expansion coefficient	
α^{th}	10^{-6}
Reference temperature (°C)	
T_0	25.0

Table 6.5: Evolution of plasticity tensor with temperature for the tall and short contact

$temp$(°C)	25	200	400	600	700
$\bar{\alpha_{33}^{sc}}$	2000	4500	5000	6000	8000
$\bar{\alpha_{33}^{tc}}$	4410	5000	6000	7000	8000

To do so, the tall and short contacts described in Section 6.2.1 are used to create a grid of contacts representing a portion in the active area with heterogenous height dimensions. For simplicity, two configurations of contact heights 3 μm apart are considered and arranged in the grid. This grid of heterogenous contacts is constrained at its edges and compressed mechanically with a displacement of 14 μm in the out-of-plane direction. Later, the mechanical configuration of the contacts is kept fixed and the temperature of the system is ramped up from 25°C and 600°C. The stress distribution in the high-fidelity analysis is shown in Figure 6.5(a). The force plotted over displacement during mechanical compression is shown in Figure 6.5(c) and force plotted over temperature during heating up is shown in Figure 6.5(d). The effective model is subjected to the same boundary conditions and the average homogenized stress distribution is shown in Figure 6.5(b). The corresponding forces are plotted with displacements in Figure 6.5(c) and the forces plotted over temperatures are shown in Figure 6.5(d).

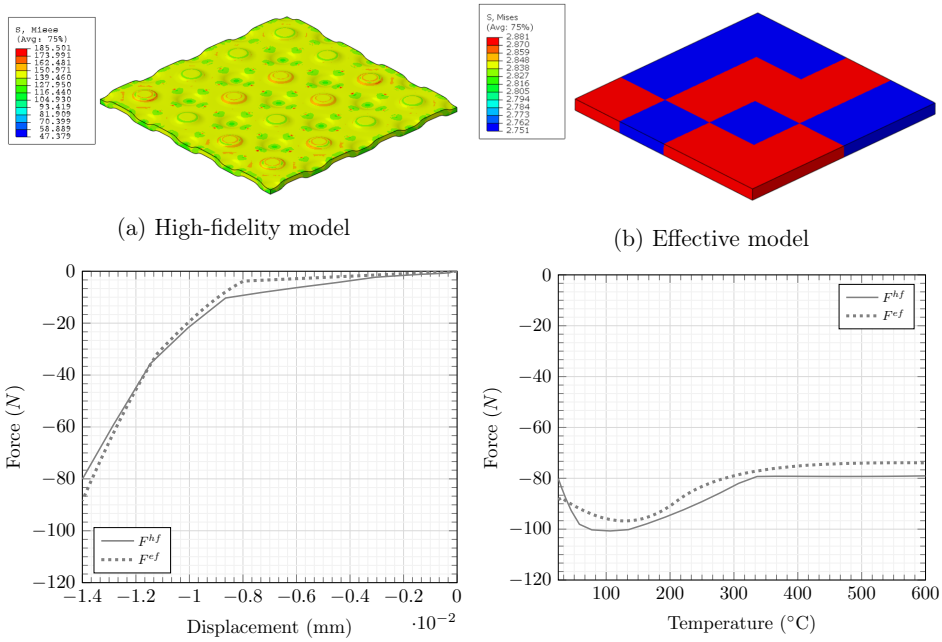

(a) High-fidelity model

(b) Effective model

(c) Force-deformation curve as a result of mechanical compression for the high-fidelity and effective models

(d) Force-deformation curve as a result of thermal expansion for the high-fidelity and effective models

Figure 6.5: Comparison of the effect of thermal expansion for the high-fidelity model and effective model of an interconnect with varying contact heights

The computational time required for the high-fidelity model was about 35 hours on the high performance cluster (HPC) with 48 cores. While the computation time required for the effective model was about 30 seconds on a standard desktop computer. The alignment of the force responses in the high-fidelity and effective models suggests that, the model accuracy achieved in the effective model, is a good compromise for the reduced simulation time.

6.3 Operation

During operation, the SOC stack is held at a constant temperature of about 600°C for prolonged periods of time. In this section, the relaxation behavior at single contacts over large

timescales are investigated using the homogenization approach assuming the variability in their height dimension. Later, an effective model is calibrated with suitable parameters to fit the high-fidelity model. Lastly, a comparison is done for a large grid of contacts between the high-fidelity and effective model configurations.

6.3.1 Parameter Identification

Generally, an SOC stack is constrained in a closed set up. During operation, the forces in a stack tend to relax due to the viscous behavior of metals at high temperatures over prolonged periods of time. This causes a reduction in the contact pressure over the lifetime of the stack, increasing ohmic resistance which deteriorates performance. These relaxation effects are attempted to be addressed using the homogenization approach in this section considering the heterogenous contact height distribution in the active area.

In order to achieve this, interconnect contacts with two height dimensions in the out-of-plane direction are considered, both being 3 μm apart as shown in Figure 6.6(a) and Figure 6.6(b). The representative unit volumes are then subjected to periodic boundary conditions as shown in Chapter 4. Let us assume their stress-states at the start of operation are defined in Figure 6.6(c) and Figure 6.6(d) for the tall and the short contact and the model is kinematically held in this configuration over a period of about $10^4 s$ at 600°C. The homogenized out-of-plane stress σ_{zz}^{hf} is plotted over time in Figure 6.6(c) for the tall contact and in Figure 6.6(d) for the short contact. It may be noted that the tall and the short contacts have the same stresses after $10^4 s$ suggesting that the rate of relaxation in the tall contact is larger than the short contact. This infers that the rate of relaxation, is dependent on the stress-state of the contact at the start of operation which is influenced by the height dimension. The effective model is subjected to the same boundary conditions so that the homogenized out-of-plane stress in the effective model σ_{zz}^{ef} is fit onto that in the high-fidelity model σ_{zz}^{hf}. This is shown for the tall contact in Figure 6.6(c) and the short contact in Figure 6.6(d). It may also be noted that, variability in the height dimension is accounted for by the *offset-strain* which is equal to the strain corresponding to 3 μm in the short contact. Therefore, simply varying the offset-strain in the two configurations of contact heights can represent the resulting effective stresses σ_{tc}^{ef} for the tall contact Figure 6.6(c) and σ_{sc}^{ef} for the short contact in Figure 6.6(d).

Table 6.6 summarizes the fitted orthotropic elastic and Hill-type viscoplastic coefficients in the effective model and Table 6.7 summarizes the rate dependent coefficients along with

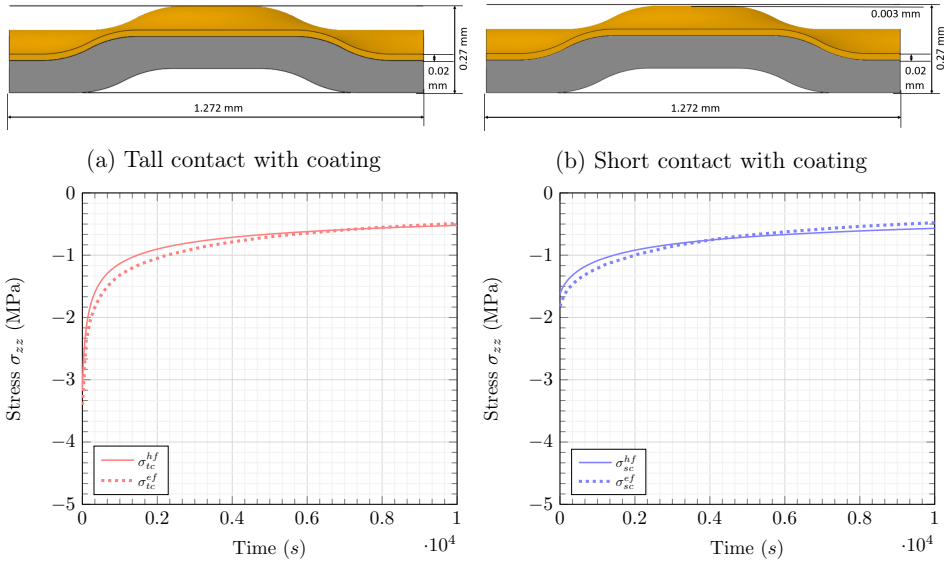

(a) Tall contact with coating

(b) Short contact with coating

(c) Stress-Time response for tall contact

(d) Stress-Time response for short contact

Figure 6.6: Relaxation behavior for contacts with variability in height dimensions

Table 6.6: Anisotropic input parameters for the effective model obtained from fitting homogenized response at 600°C.

(a) Elasticity

Elastic coefficients (MPa)	
$\mathbb{C}_{11}$	52000
$\mathbb{C}_{12}$	0
$\mathbb{C}_{13}$	0
$\mathbb{C}_{22}$	52000
$\mathbb{C}_{23}$	0
$\mathbb{C}_{33}$	310
$\mathbb{C}_{44}$	10000
$\mathbb{C}_{55}$	750
$\mathbb{C}_{66}$	750

(b) Viscoplasticity

Hill coefficients (-)	
α_{11}	0
α_{12}	0
α_{13}	0
α_{22}	0
α_{23}	0
α_{33}	2100000
α_{44}	0
α_{55}	0
α_{66}	0

Table 6.7: Input parameters for the effective model obtained from fit to homogenized response at 600°C.

(a) Viscoplasticity.

Initial strain rate (-)	
$\dot{\epsilon}_0$	3.5e−9
Initial stress (MPa)	
σ_0	290.81
Exponent (-)	
n	2.28

(b) Tall contact.

Offset strain (-)	
$\varepsilon_{tol}^{of,tc}$	0.025
Coating thickness (mm)	
a^{tc}	0.02
Coating stiffness (MPa)	
b^{tc}	40.0

(c) Short contact.

Offset strain (-)	
$\varepsilon_{tol}^{of,sc}$	0.036
Coating thickness (mm)	
a^{sc}	0.02
Coating stiffness (MPa)	
b^{sc}	40.0

offset and coating parameters for the tall and short contacts.

6.3.2 Relaxation validation for 1-Layer: 16 Contacts

In order to validate the relaxation behavior for the effective model, it may be compared to its corresponding high-fidelity model with varying height dimensions. As mentioned in the previous section, the contacts described in Section 6.3 are arranged together to form a grid of sixteen contacts representing a typical portion of the active area. The height difference between the two configurations of contacts were considered to be 3 μm apart. This grid of contacts was then preloaded mechanically with a displacement of 14 μm. Assuming this configuration as the starting point for operation, the system is then held in this position over a period of about $10^4 s$ at a temperature of 600°C. The stress distribution in the high-fidelity analysis is shown in Figure 6.7(a). The effective model is loaded with the same mechanical displacement for the same time period and temperatures and average homogenized stress distribution is shown in Figure 6.7(b). The relaxation force is plotted over time for the high-fidelity model and the effective-model in Figure 6.7(c).

The high-fidelity model took about 42 hours of run-time with 48 cores on the high performance cluster (HPC). Whereas, the effective model took about 3 minutes to completion on a standard desktop computer. The force responses in the high-fidelity model and the effective model indicate that the effective model represents the high-fidelity model to a high degree of precision and may be used to represent the high-fidelity model.

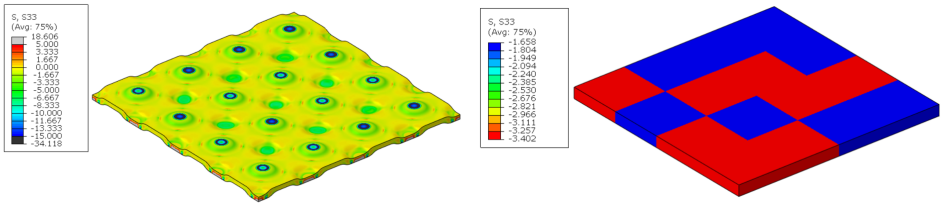

(a) High-fidelity model

(b) Effective model

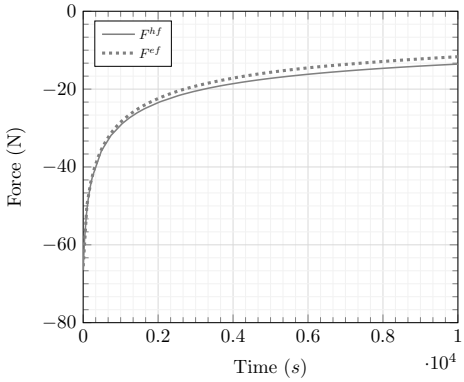

(c) Force-deformation curve as a result of relaxation for the high-fidelity and effective models

Figure 6.7: Comparison of the effect of relaxation for the high-fidelity model and effective model of an interconnect with varying contact heights

6.4 Unified model

Upon validating the individual effects on a grid of contacts for each loading step, all these steps in the life cycle of an SOC stack may be combined into one unified model. However, in order to model different time scales during temperature ramp-up and operation, it may not be possible to use the same set of viscoplastic material parameters for the two process steps using this material model. Therefore, each step needs to be modeled separately using a set of material parameters to obtain its corresponding stress state and model configuration at the end of the step. This deformed model configuration and stress state is then imported into the next process step for the current stress state and configuration. Using this approach, the theoretical contact pressures may be calculated stepwise and later, the corresponding operational electrical resistance may be estimated.

Figure 6.8 depicts the loading curves for the three process steps for the high-fidelity and effective models. In the mechanical loading phase, the contact is compressed uniaxially in the out-of-plane direction with a deformation of 14 μm. The corresponding stress-strain relationship is depicted in Figure 6.8(a). This deformed geometry and stress configuration is then subjected to a thermal loading from 25°C to 600°C while constraining further deformation. Figure 6.8(b) represents the stress-temperature relations for the high-fidelity and effective models during thermal loading. Once again, the deformed geometry and stress configuration obtained at the end of this stage are then allowed to relax over a time period of 10^4s. Figure 6.8(c) shows the stress-time relation during operation which depicts the relaxation behavior over large time scales.

As mentioned before, the model considered here uses a different set of material parameters for each stage because the set of material parameters required to fit larger timescales of operation are incapable of capturing the non-linear viscoplastic effects observed during smaller timescales of heating up. Using individual steps, the stress path across these loading steps may be determined to obtain contact forces on individual contacts in the active area of a stack at any stage during its lifetime.

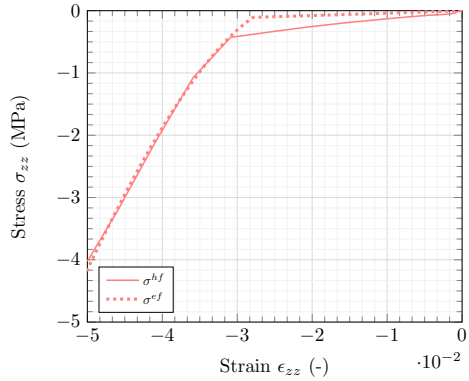

(a) Stress response with strain during mechanical compression of an SOC contact

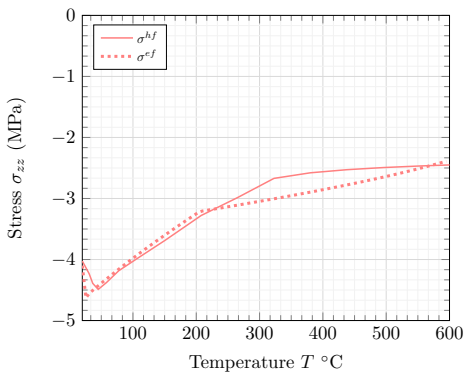

(b) Stress response with temperature during heating up an SOC contact

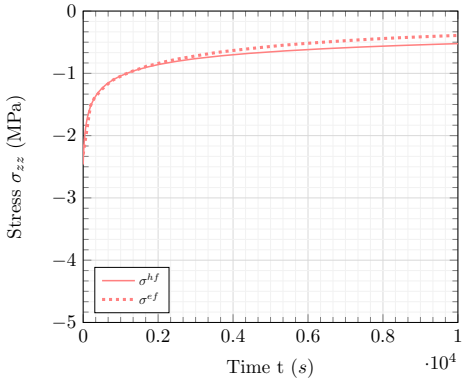

(c) Stress response with time during operation of an SOC contact

Figure 6.8: Unified model for the three process steps of an SOC contact life-cycle

6.5 Summary of computational investigations and validation

In summary to the investigations conducted in this chapter, a fast computing effective model was parameterized and fit to the homogenized high-fidelity simulations. The effective model was representative to the high-fidelity model in terms of all uniaxial orthotropic loading cases as well as volume dilational relations in the elasto viscoplastic framework.

In order to validate the proposed offset and coating formulations derived in Chapter 5, a corresponding full field simulation for individual loading steps was created and compared with the effective model. The loading steps represented the effect of contact tolerances during assembly, temperature ramp-up and operation to give the stress path during the lifecycle of individual contacts. It was noted that the computational time required for the effective model was reduced by several orders of magnitude while maintaining a high order of accuracy for each of the loading steps.

Finally, a unified model was demonstrated by performing each of the loading steps subsequently on the corresponding deformed configurations of the model from preceeding steps. In summary, this gives a fast computing model which accounts for the height variability of contacts considering all the model requirements stated in Chapter 4 and Chapter 5. In the next chapter, the output parameters obtained from the effective model will be used to extrapolate relavant parameters which determine the theoretical electrical contact resistance.

7 Correlating effective model parameters to contact resistance

With the validation of a computationally feasible finite element approach for evaluating mechanical stresses over the lifetime of SOC contacts in Chapter 6, the next step involves extrapolating the required parameters to estimate the electrical contact resistance. The influence of mechanical loading on electrical contact resistance has been studied previously in literature [21–25, 152]. These works provide insight into the correlation between mechanical loading and electrical contact resistance in a stack.

Building upon these insights and the model developed in the previous chapters, the current chapter aims at finding a path to determine some key performance parameters of an SOC using the finite element model. To achieve this, the model calculates stress on individual contacts within the finite element framework during different loading stages. These stress values can then be integrated into a relation which captures the dependence of contact resistance on mechanical loading in a generalized form, allowing for the estimation of theoretical contact resistance from the effective model parameters.

In the context of evaluating the required parameters from the model, there are two key quantities that can be measured experimentally:

- Contact pressure after mechanical assembly
- Electrical contact resistance during operation

The primary focus of this chapter is to determine these two measurable quantities from the finite element model by establishing a suitable workflow with simulation results.

7.1 Evaluation of contact pressure after mechanical assembly

To evaluate the contact pressure after mechanical loading, a suitable methodology is outlined in this section based on an assumption that the only form of tolerance on the SOC contacts is the variability in the height dimension, with all other dimensions being fixed according to design specifications. While estimating contact pressure in the high-fidelity model, the contact area varies due to deformation during the loading cycle, introducing a geometric dependence which can be attributed to the interconnect design. This geometric dependence can be effectively captured by considering the effective strain ($\boldsymbol{\varepsilon}^{ef} = \boldsymbol{\varepsilon} - \boldsymbol{\varepsilon}^{of}$) experienced by the contact during loading.

To achieve this, a relationship between the average contact pressure and the effective strain may be evaluated at an individual contact. This can be considered in a typical high-fidelity simulation as shown in Figure 7.1(a) and the corresponding relation for the average contact pressure p^{hf}_{avg} over a specific area in the RVE is shown in Figure 7.1(b). In a practical scenario, the driving displacement or applied force used for stack compression serves as the boundary condition for the effective model. Upon computing the effective strains within effective model, the relation from Figure 7.1(b) can be used to determine the average contact pressure directly from this model. For a more generalized workflow, the Gaussian function mentioned in Equation 7.1.1 is then fitted onto the relation by assigning suitable coefficients. With Equation 7.1.1, the contact pressure p^{ef} is written as a function of the effective strains ε^{ef}_{zz} and can be approximated directly in the effective model.

$$p^{ef}(\varepsilon^{ef}_{zz}) = k_1 \exp\left[-\left(\frac{\varepsilon^{ef}_{zz} - k_2}{k_3}\right)^2\right] + k_4 \exp\left[-\left(\frac{\varepsilon^{ef}_{zz} - k_5}{k_6}\right)^2\right] + k_7 \exp\left[-\left(\frac{\varepsilon^{ef}_{zz} - k_8}{k_9}\right)^2\right] \tag{7.1.1}$$

where, the effective strain is within the bounds for which the function is fitted $\varepsilon^{ef}_{zz} \in [0, 0.25]$. The coefficients for Equation 7.1.1 are evaluated using a curve fitting routine and summarized in Table 7.1. Using these parameters, the fitted function in Equation 7.1.1 is plotted as p^{ef} in Figure 7.1(b).

To check if this relation holds true for different tolerance values, the average contact pressure p^{hf}_{avg} at each contact is evaluated in a high-fidelity grid of sixteen contacts shown in Figure 7.2(a) and compared with the contact pressures p^{ef} evaluated from the effective

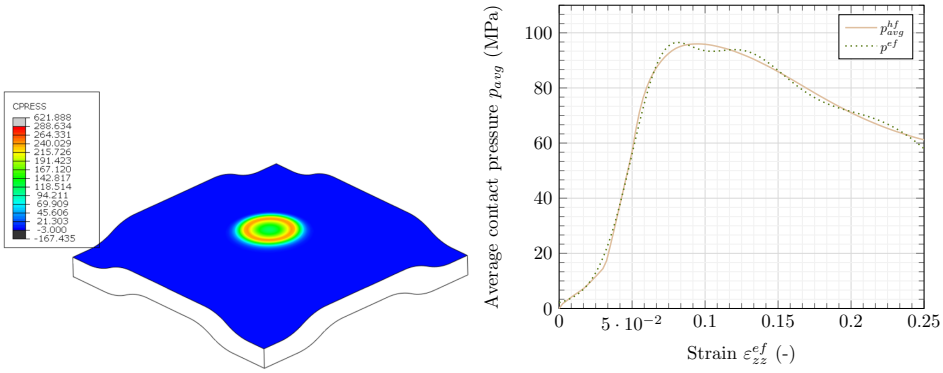

(a) Contact pressure p_{avg}^{hf} in high-fidelity simulation for one contact

(b) Fitting of contact pressure p^{ef} for effective model

Figure 7.1: Evaluating contact pressures at individual contacts in the high-fidelity p^{hf} and effective model p^{ef}.

Table 7.1: Input parameters for estimation of contact pressure from effective model response.

Contact pressure coefficients (-)	
k_1	46.83
k_2	0.06711
k_3	0.02851
k_4	63.51
k_5	0.1118
k_6	0.05506
k_7	67.28
k_8	0.2106
k_9	0.1014

model shown in Figure 7.2(b). At a nominal stacking force of about $218N$, the distribution of contact pressures at each contact is compared for the high-fidelity model and the effective model in Figure 7.2(c).

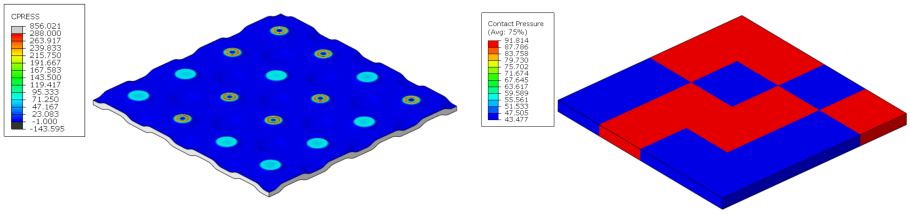

(a) Contact pressure p_{avg}^{hf} in high-fidelity simulation of 16 contacts

(b) Contact pressure p^{ef} in effective model of 16 contacts

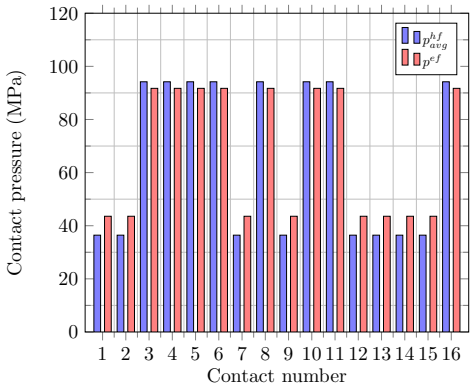

(c) Comparison of contact pressures in high-fidelity p^{hf} and effective model p^{ef} at $218N$

Figure 7.2: Validation of contact pressures at individual contacts in the high-fidelity p_{avg}^{hf} and effective model p^{ef}.

It is important to note that this relation is applicable to the contact pressure for a purely mechanical loading as the contact pressure is a function of the driving strain $p_{avg}(\boldsymbol{\varepsilon}^{ef})$. With this framework, the mechanical pressures at the interconnect contacts can be calculated after mechanical compression at room temperature.

7.2 Relation to electrical output

Upon defining a workflow to compute the contact pressure p^{ef} directly in the effective model, the next step is to establish a relation of the electrical contact resistance with the

output parameters available from the effective model [153]. In order do so, it is essential to isolate the contact resistances by considering a small portion of the interconnect with negligible in-plane bulk resistance in comparison to the contact resistance. Using an experimental arrangement as shown in Figure 7.3(a), the contact resistance at a single contact was measured while applying a force on the contact and heating it up to operational temperature. This test was done for different forces within the expected operational force range while measuring the contact resistance. Thus, a dependence of the contact resistance with the applied force is observed at operating temperatures in the normalized experimental relation and is plotted in Figure 7.3(b). As no other variables are considered for these tests, at a constant temperature, the contact resistance $R_{contact}$ may be expressed as a function of the applied contact force F^{ef} provided the applied force is within the domain of experimentally applied forces $F^{ef} \in [\mathcal{F}_0, \mathcal{F}_n]$.

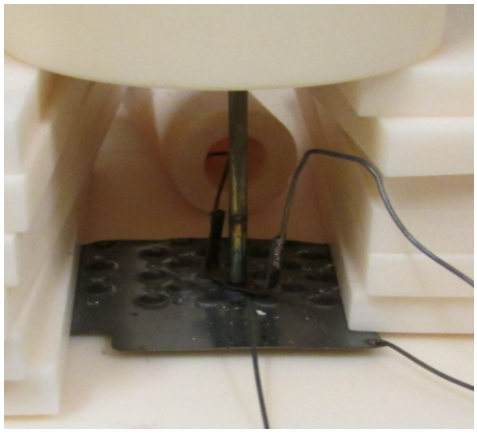

(a) Experimental set-up to determine contact resistance as a function of applied load

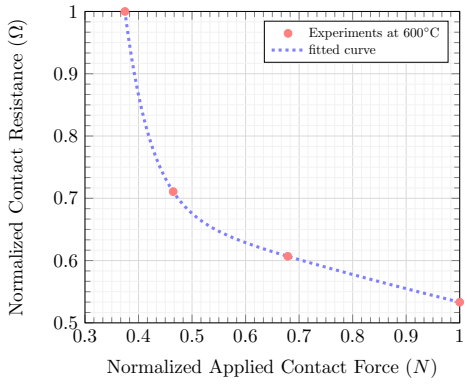

(b) Normalized relation of electrical resistance with contact force

Figure 7.3: Experimental evaluation of contact resistance as a function of contact pressure

$$R_{contact} = \{R_{contact}(F^{ef}) \,|\, F^{ef} \in [\mathcal{F}_0, \mathcal{F}_n]\} \tag{7.2.1}$$

This function was fitted onto the experimental data using a curve fitting routine and is shown in Figure 7.3(b). The corresponding mathematical formulation for the contact resistance $R_{contact}$ is expressed in Equation 7.2.2,

$$R_{contact}(F^{ef}) = k_1 e^{k_2 F^{ef}} + k_3 e^{k_4 F^{ef}} \tag{7.2.2}$$

where, the force is within the bounds for which the function is fitted $F^{ef} \in [\mathcal{F}_0, \mathcal{F}]$ and

Table 7.2: Coefficients for Equation 7.2.2 obtained from curve fitting routine.

Contact resistance coefficients (-)	
k_1	0.001763
k_2	-5.655
k_3	0.6182
k_4	-0.1111

the fitted coefficients k_1, k_2, k_3 and k_4 are noted in Table 7.2. Subsequently, the contact forces may be evaluated in the effective model from the stress states in the loading steps, seen in Section 6.4 can be directly plugged into Equation 7.2.2 to calculate the contact resistance within the given force range.

As depicted in Figure 7.4(a), while assuming negligible in-plane bulk resistance within the interconnect as well as the substrate, the individual contact resistances on a single interconnect form a set of parallel resistances for the contacting between each repeat unit. In a similar way, the stack may be viewed as parallel circuits connected in series with the subsequent repeat units. In such a way, the theoretical contact resistance in a stack may be evaluated.

In order to demonstrate this workflow, a grid of 16 contacts with arbitrary height dimensions on each contact is considered during operation and shown in Figure 7.4(b). The stress states during operation are simulated and used to calculate the resistance at each contact over life-time using the normalized relation shown in Equation 7.2.2. The contact resistances are plotted over the operating time for each contact in Figure 7.4(c). Finally, considering the grid as a circuit of parallel resistances, the total contact resistance of the grid is evaluated over the simulated operational duration using Equation 7.2.3.

$$\frac{1}{R_{Layer}} = \frac{1}{R_1} + \frac{1}{R_2} + \frac{1}{R_3} + ... + \frac{1}{R_n} \tag{7.2.3}$$

Upon computing the total resistance over time R_{Layer} for the grid of contacts, it is a common practice to compute the specific resistance $R_{sp} = R_{Layer}.A$, where A is the area under consideration in cm^2 which can be considered as unit area in this demonstration. In the next chapter, the demonstrated approach will be used to validated with experimental tests over a grid of contacts.

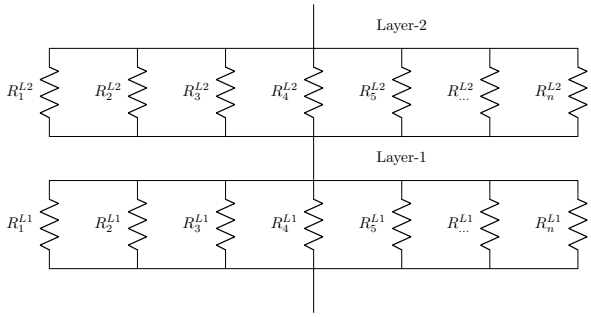

(a) An SOC stack in the form of a circuit of contact resistances

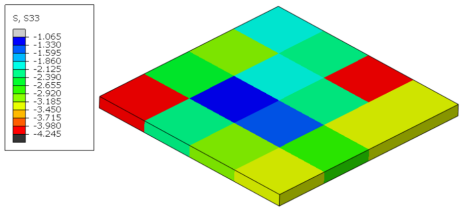

(b) Grid of contacts with varying height dimension during operation

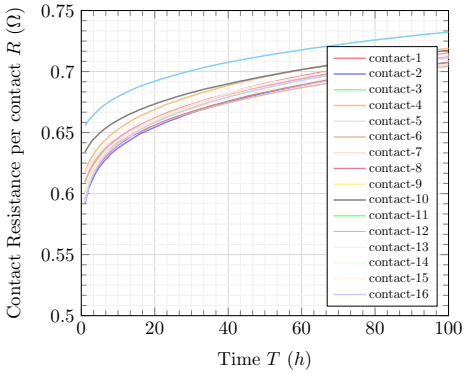

(c) Contact resistances at individual contacts over life-time

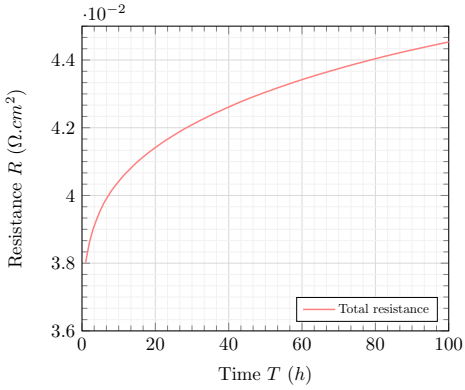

(d) Total resistance for the gird over life-time

Figure 7.4: Application: Evaluation of electrical contact resistance

7.3 Summary

The output parameters like stresses and strains in the finite element model are limited in terms of applicability in real-world SOC use-case. In this chapter, a suitable workflow was outlined to obtain typically used key performance parameters for an SOC use-case, directly from the effective model. This creates a framework to estimate the contact pressures after mechanical compression and the electrical contact resistance on the contacts from the output of the effective model.

8 Experimental validation

In the preceding chapters, a modeling approach was developed to calculate the theoretical contact pressures at individual contacts within the finite element framework. With this methodology, it is possible to calculate the ohmic contact resistance at individual interconnect contacts. In Chapter 4, challenges related to manufacturing tolerances were identified for the mechanical contacting during stacking. In Chapter 5, constitutive model equations were formulated and adapted to account for dimensional tolerances, and these were implemented using the homogenization approach to achieve practical computation times. In Chapter 6, the developed effective models were validated against their corresponding high-fidelity models for various loading steps encountered during the lifetime of an SOC stack. Chapter 7 employs the effective model to determine key parameters to evaluate the theoretical ohmic resistance. In the current chapter, the model is compared with experimental tests to assess its application in a typical use-case.

Validation experiments are conducted to examine two phenomena:

- Contact pressures distribution in the active area after mechanical stacking
- Total contact resistance across a grid of contacts at operational temperature

8.1 Mechanical contact pressure tests

In order to assess the efficiency of mechanical stacking, the quality of contacting after mechanical stack assembly is evaluated experimentally, as was briefly outlined in Section 4.3. This evaluation employs a method commonly known in the literature as pressure film testing. This section provides a detailed description of the pressure film test. Subsequently, the test is conducted on a 10-layer stack, and the results are compared with corresponding finite element simulations. By comparing the force-deformation relationships from experiments and simulations, along with the degree of similarity in contact

patterns, the accuracy of the formulated simulation methods may be evaluated for the given use-case.

8.1.1 Pressure film experiments

Several pressure film investigations concerning the contact pressure distribution in the active area have been carried out in literature [139, 140, 143]. Pressure films are thin, durable sheets embedded with microcapsules containing a coloring agent. When mechanical pressure exceeding a certain threshold is applied to the pressure films, these capsules burst, releasing the coloring agent, which then reacts with a color developer to produce red-colored areas on the film. The intensity of the color varies with the magnitude of the applied pressure, thereby creating a visible distribution of pressure across the contacting surfaces. Different variants of the pressure film sheets are designed to measure contact pressures within a specified range. The selection of the appropriate pressure film variant is crucial to ensure the pressure values fall within the effective measurement range of the pressure film [154–156].

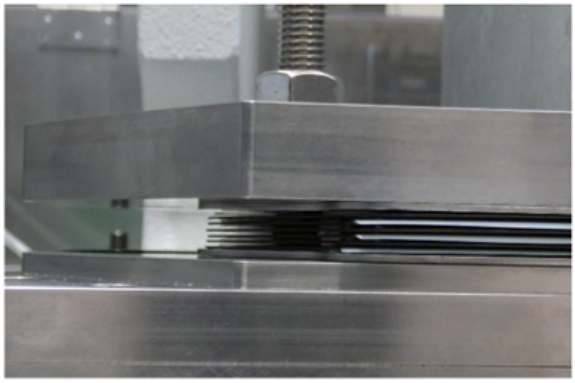

Figure 8.1: Mechanical setup of a stack with pressure films between cells

In an SOC stack, pressure films are commonly used to assess contact pressure distribution between repeat units in the active area. Typically, a stack is constructed using individual cells, with pressure films placed between them [157]. In this case, pressure films are placed at four locations in the stack, after every 2 repeat units. The mechanical setup for a 10-layer stack is shown in Figure 8.1. When mechanical loading is applied to compress the stack, the metallic interconnect leaves an imprint on the film, where the intensity of the imprint corresponds to the contact pressure created at that

contact. These imprints are then quantitatively analyzed using Fujifilm software (FPD-8010E).

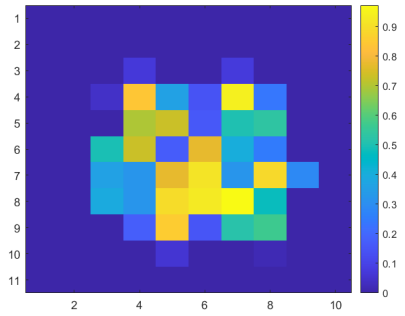

(a) Pressure distribution on a single contact

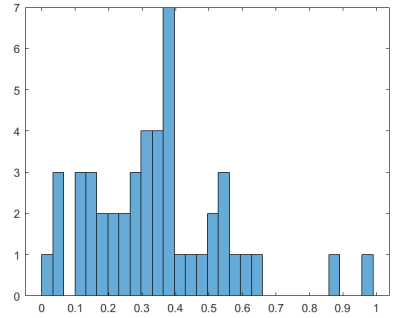

(b) Visualization of pressure film data

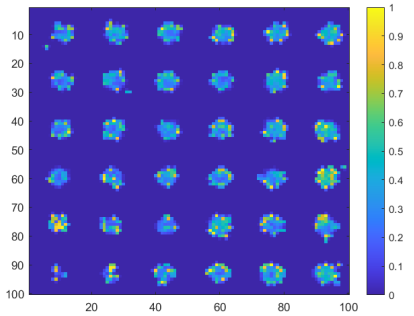

(c) Pressure distribution in a grid of contacts

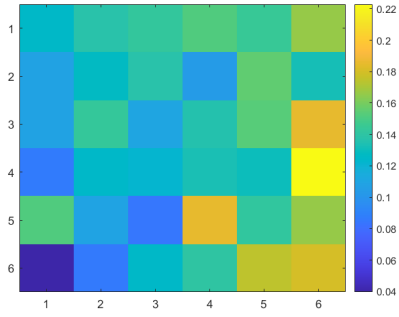

(d) Effective pressure distribution in a grid of contacts

Figure 8.2: Quantitative evaluation of pressure film data

After conducting the test, the pressure film image data is imported into the Fujifilm software, and a postprocessing step is performed in MATLAB to enhance the visualization of the pressure distribution. In this step, the intensity of red tones is replaced by a continuous spectrum, as shown in Figure 8.2(a) for a single contact. Additionally, the pressure intensities at the pixels of a scanned imprint may be represented as a histogram in Figure 8.2(b). The pressures at each distinct contact, shown in Figure 8.2(c), are then segmented using image processing tools, such as a bounding box. As depicted in Figure 8.2(d), the pressure over each contact is averaged across its area to determine the effective contact pressures. This postprocessing approach enhances the pressure distribu-

tion contour with an improved visualization of the averaged contact pressures for better interpretation.

Cautions with pressure film experiments

Pressure film experiments are reliable in capturing the variation of pressure distribution across the active area. However, the absolute pressure values may not be entirely repeatable in the current application due to the contact between small, relatively sharp surfaces. This may introduce inaccuracies in the absolute values of contact pressures obtained through experimental methods as each contact point may produce pressure imprints which may not be resolved by any single type of film. Nonetheless, the pressure distribution patterns across the active area tend to be consistent when the same stack is compressed multiple times.

Another limitation of the pressure film test is the potential presence of defects in the films, which can result in smudges on certain areas of the sheet. These smudges may arise from improper handling or inherent defects in specific locations of the pressure film. To ensure accurate pressure distribution measurements, it is crucial that the sheets are defect-free and handled with care during testing.

Finally, it is important to note that the contact patterns observed during mechanical stacking can change at operational temperatures due to various factors. However, the pressure film test is limited to room temperature and can only determine the contact pressure distribution after mechanical stacking step, without being able to give information on the change in contact configuration during operation.

8.1.2 Simulation of pressure film tests

In the previous subsection, an experimental setup of the pressure film test consisting of 10 repeat units were stacked together and compressed with a mechanical load to obtain the contact pressure distribution in the active area. In order to demonstrate the methods developed in this work, a finite element model of these repeat units is constructed to compare the key parameters obtained from simulations with the experimental results.

To achieve this, each repeat unit is measured at the measurement station described in Section 4.3.1. After postprocessing the measurement data, profiles of individual substrates

Table 8.1: Characterized profiles for measured interconnects and substrates and contact height distributions for interconnect contacts

Interconnect profile	Substrate profile	Contact height tolerance
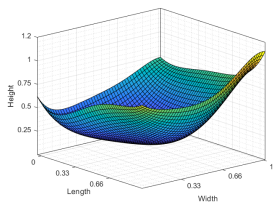	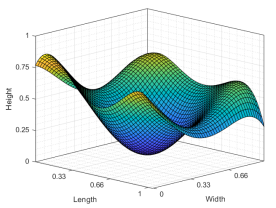	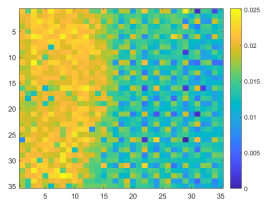
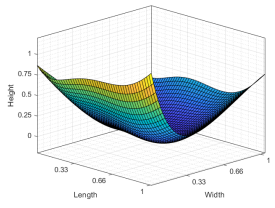	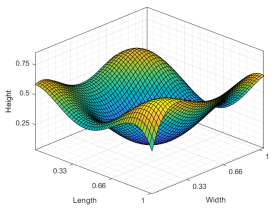	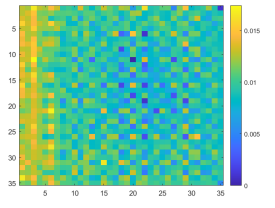
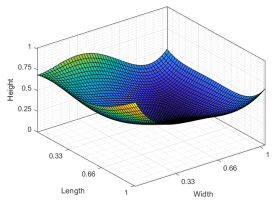	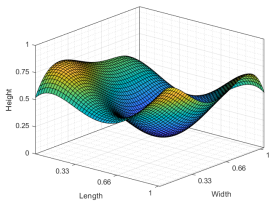	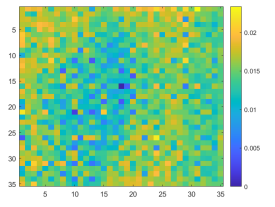
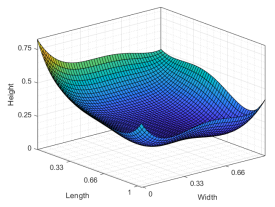	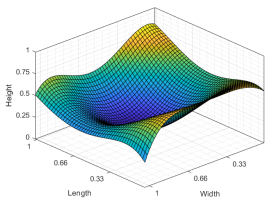	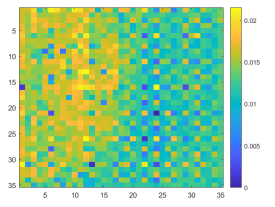

and interconnects are characterized by fitting them onto a 5^{th}order polynomial plane equation, of the form described in Equation 4.3.1. The characterized profiles for some of the substrates and interconnects are illustrated in Table 8.1. These profiles are then employed in the finite element framework by mapping the nodes of the discretized geometries of the interconnect and substrate to coordinates determined from their respective polynomial equations. The finite element solver ABAQUS CAE is used for this purpose and the geometries for each substrate and interconnect are generated using an automated workflow programmed in PYTHON. This ensures that the finite element model may accurately capture the unique geometric features of each repeat unit and provides a reliable basis for comparison with the experimental tests.

As outlined in Section 4.3.3, the contact height tolerances are spatially characterized in the form of a matrix which represents the tolerance values at each contact point. This matrix is imported into ABAQUS CAE through the PYTHON workflow and then each element is assigned a value of offset-strain which is directly correlated to the corresponding contact height tolerance. As discussed in Section 4.3.3, this approach allows the precise reflection of the dimensional variability present at the interconnect contacts. With the characterized profile geometries and evaluated offset strains, the manufacturing non-idealities described in Section 4.3 are systematically integrated into the model.

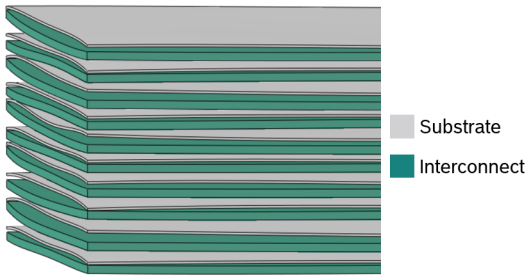

Figure 8.3: Simplified finite element model of the stack based on measurement data

The discretization of individual repeat units is done in such a way that each representative unit volume of the interconnect may represent a single element. Hexagonal elements (C3D8) are used to discretize the interconnect and continuum solid shell elements (CSS8) are chosen for the metallic substrate due to their higher degree of bending. The repeat units are stacked together into an assembly and held between rigid plates. A surface-to-surface contact formulation is defined for each contacting surface in the assembly. The assembly for the model is depicted in Figure 8.3. Finally, compressive

deformation is applied representing boundary conditions similar to the experimental tests over one static time step. The corresponding finite element calculations are done numerically in the ABAQUS solver and the results obtained will be looked at in the next section.

8.1.3 Comparison of simulation results with experiments

In this section, a comparison between the results of the experimental and simulation approaches is made for the 10-layer stack. Two key parameters are chosen to serve as a basis for comparison of the two approaches:

- Force-deformation relation of the stack
- Contact pressure distribution patterns in the active area

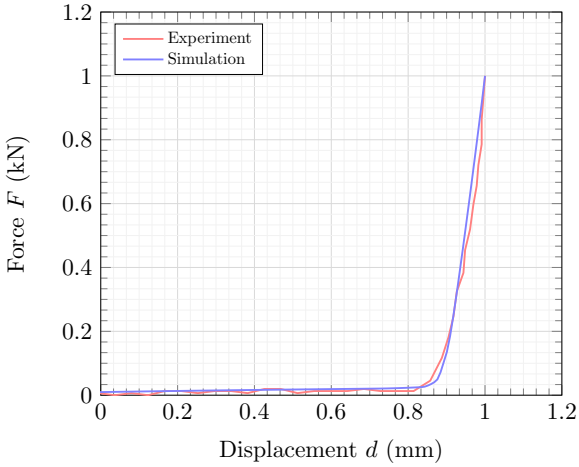

Figure 8.4: Force-Deformation relation of a 10-layer stack during mechanical compression

Upon completion of the simulation, the force-deformation curves of the simulations and experiments are compared. Figure 8.4 presents the force-deformation behavior for both the experimental tests and simulations. The initial portion of the curve is characterized by a low stiffness, which is attributed to the compression of the non-repeated bending profiles that have gaps between the layers. Once these profile gaps are closed, the stiffness sharply increases until the target force is reached, as seen in Figure 8.4. The force-deformation curves for the simulations and experiments appear to align closely with

each other. This correlation between the model and experimental tests suggests that the model represents the mechanical response of the tests to a high degree of precision.

Another key aspect of this study is to understand the effect of the applied force on contact pressure distribution across the active area. In order to do so, the contact pressure distribution generated during simulations and experiments must be compared. This may be achieved by simply comparing the degree of similarity between contact patterns for the simulations and experiments. For the experimental approach, the data obtained from pressure films was postprocessed in MATLAB to visualize the contour of contact pressure distribution as described in Section 8.1.1. Similarly, the simulation data was postprocessed using the same steps and the resulting pressure contours were compared in Table 8.2.

The results reveal that, the contact pressures are generally higher at the edges compared to the center of the active area. As the simulated model captures these details, these effects may be seen as a consequence of the interaction of contact height distributions and profiles of individual components which is considered by the effective model. The comparison of contact patterns for the four measured layers show a strong spatial correlation between the simulation and experimental results, indicating that the finite element model effectively represents the experimental stack compression behavior. This validates the simulation model for stack compression analysis.

Table 8.2: Comparison of experimental and simulated contacting patterns in the active area

Simulation	Experiment	Probability distribution
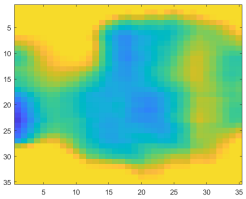	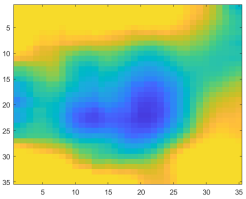	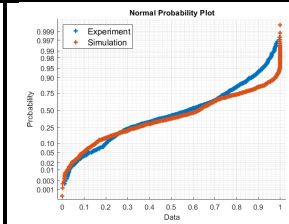
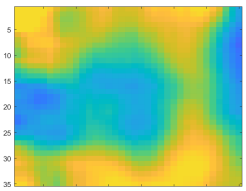	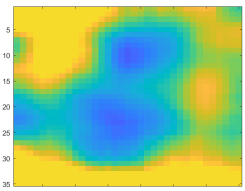	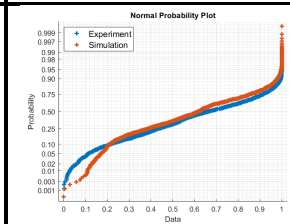
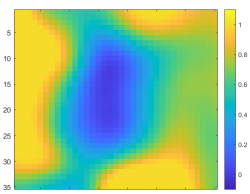	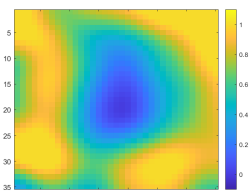	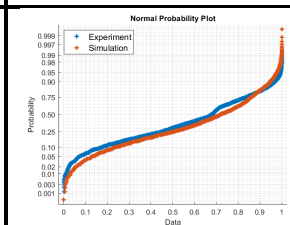
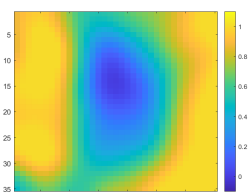	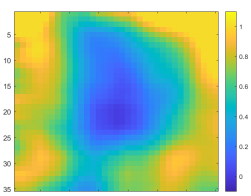	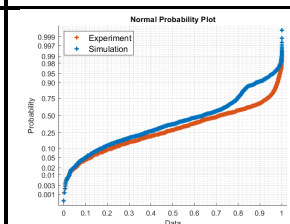

8.2 Operational contact resistance tests

8.2.1 Experimental set-up

As discussed in the previous chapters, at operational temperatures, various thermal influences come into play and can alter the contact pressure configuration established at room temperature, which may consequently change the contact resistance. The final objective of this work is to apply the developed methods to a specific use-case to determine the mechanical loading at individual contacts and to evaluate the theoretically derived contact resistance presented in Chapter 7.

To evaluate the contact resistance over a representative section of the active area, a grid of 9x9 contacts from the active area of the interconnect is cut out and integrated into an experimental setup, as shown in Figure 8.5(a). This grid is connected in a series circuit together with the metallic substrate depicted in Figure 8.5(b) where the voltage drop across the interconnect and substrate is recorded. This assembly is compressed under varying loads, applied as weight placed on the interconnect. The interconnect-substrate assembly is placed in an oven and heated up to 600°C as depicted in Figure 8.5(b). The temperature of the interconnect is monitored using a thermoelement. The resistance across the interconnect and the substrate is calculated at operational temperatures using a device called a RESISTOMAT.

In order to demonstrate the applicability of the model, the weights on the interconnect-substrate assembly are varied and the tests are repeated for different weights. These tests are conducted for four weights corresponding to 10N, 50N, 120N and 200N of force. The contact resistances are then evaluated at 600°C for the corresponding applied forces are plotted in the next section in Figure 8.7 and compared to simulation results.

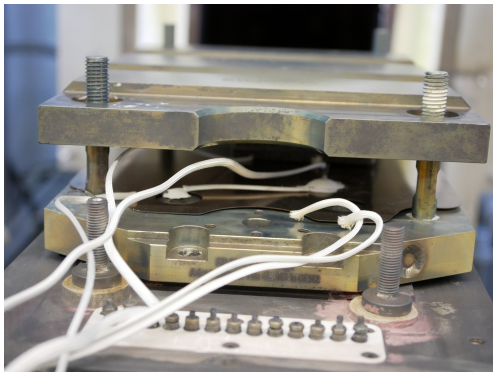

(a) Experimental arrangement for contact resistance tests

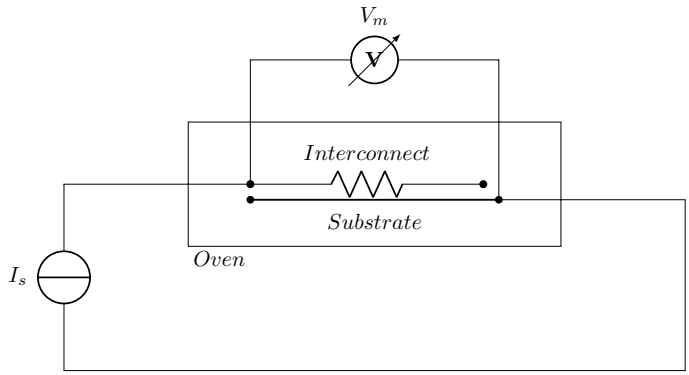

(b) Schematic representation of the experimental set-up in the form of a circuit diagram

Figure 8.5: Experimental approach for measuring contact resistance across a grid of contacts

8.2.2 Simulation model

In order to test the methods developed in this work, a finite element model of the grid of contacts shown in Figure 8.5(a) is created in ABAQUS. The dimensional variability across the grid of contacts was measured using the measurement station described in Section 4.3.1 and the contact height distribution is presented in Figure 8.6(a). Due to the relatively small portion of the active area, the bending profile measured was flat and was not required to be fit with polynomial equation.

The measured contact heights are translated into the model as offset strains and considering the flat profile of the interconnect. The grid of contacts was loaded with a range of forces up to 200 N. Keeping the force constant, a thermal loading was applied to the grid of contacts from 25°C up to 600°C.

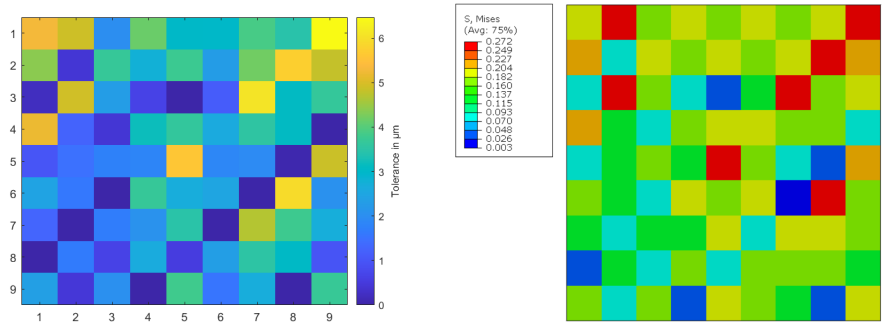

(a) Contact height distribution across the interconnect grid

(b) Stress distribution across the interconnect grid

Figure 8.6: Contact height distribution of the contact grid and stress distribution across the contact grid on application of loading

Using the methodology described in Section 7.2, the contact forces are determined from the stress-state at the end of the thermal loading and these contact forces are then used to evaluate the contact resistance at each contact using Equation 7.2.2. Upon doing so, the total resistance of the contacts are calculated with the relation for parallel resistances demonstrated in equation 7.2.3.

The simulated contact resistances are plotted against their corresponding applied forces in Figure 8.7. The experimental contact resistances evaluated at specific forces are plotted in the comparison to the simulated curve. This demonstrates that the proposed workflow

gives a reasonable estimate of the contact resistance during operation. Consequently, it also means that the variation of forces with temperature shown in the model are in alignment with experimental contact forces which in turn show a good alignment of their contact resistances.

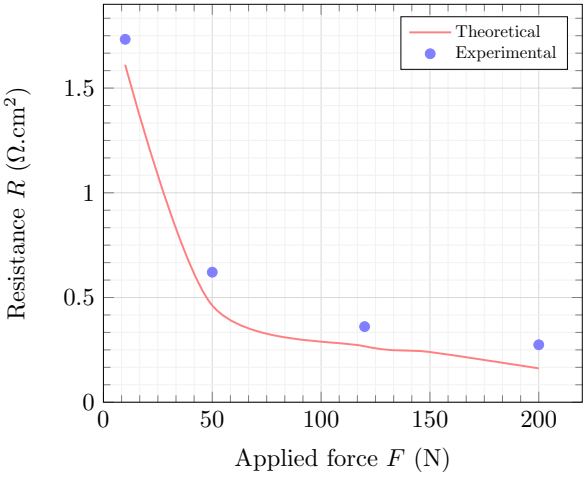

Figure 8.7: Comparison of theoretical resistances with experimental tests

8.3 Summary

In summary of the current chapter, the developed model was applied to use-cases for the mechanical stacking process and to estimate the electrical contact resistance at the contacts. On comparison with experimental results the model showed a close alignment with experimental data.

9 Conclusion and Outlook

9.1 Conclusion

This work focuses on developing the necessary tools within the finite element framework to estimate the effects of non-ideal manufacturing conditions on SOC components, particularly in relation to the contact configuration. To derive the necessary material data, experimental tests were conducted on individual contacts for the outlined loading conditions expected within the lifetime of the SOC stack.

Due to the large computational times required for commercial stack simulations, computational homogenization methods were employed by characterizing the periodically repeating structure of SOC contacts as the representative volume of the active area. However, there was a deviation between simulation results and experimental tests due to manufacturing tolerances on components. These manufacturing tolerances on the SOC interconnect were characterized into two types:

- Bending tolerances
- Contact height tolerances

Out of the two mentioned forms of manufacturing tolerances the bending tolerances were easily adaptable into the homogenization framework, however, conventional plasticity models could not represent the tolerance behavior on individual contacts as an equivalent material response. Moreover, the behavior of the coating and volume dilation within the plastic domain also needed to be considered. In order to model all these effects using the homogenization approach, within the finite element framework, a constitutive material model was developed with the *offset formulation* and *coating formulation*. The constitutive model was then adapted to show thermal and rate dependent effects like thermal expansion, temperature dependence of elastoplastic material

response and creeping/relaxation. The constitutive model is then represented in an algorithmic setting and implemented into the finite element framework in the form of a subroutine.

Upon developing a model that is capable of capturing the aforementioned effects, the model was calibrated with suitable parameters to represent the different loading cases in the lifetime of the SOC stack. The methodology was then applied to a grid of contacts with variability in the contact height dimensions, to compare the full-field and simplified models. Upon comparison it was seen that the high-fidelity model closely represented the full-field model and captured the required aspects.

In order to extract the required key parameters from the finite element model, a workflow was created to obtain these parameters directly from the effective model. The two key parameters which were considered important for the electrical contact resistance were:

- Contact pressure after mechanical stacking.
- Electrical contact resistance

Finally, the developed methodology was applied to an experimental use-case. The two use cases were:

- Mechanical stack assembly at room temperature: In this test, a stack was mechanically compressed and the mechanical stiffness, along with the generated contact patterns of the simulation were compared to experiments.
- Electrical contact resistance: In this test, a grid of contacts were compressed and heated to operational temperature. Within a series circuit, the electrical contact resistance across the grid was measured and compared to the values estimated from simulations.

The above-mentioned use-cases, give confidence that the developed model shows the experimentally observed mechanical behavior during the stacking process. Moreover, the convergence of the calculated electrical contact resistance with experimental values suggests that, the finite element model demonstrates a reasonable evolution of the contacting configuration at operational temperatures.

Limitations of model

Along with the aforementioned methodology and potential applications for the model, it may be worthwhile to examine the limitations and future prospects that could be incorporated into this model. One such prominent aspect is the thermal cycling behavior [158–160]. Although the proposed model is assumed to operate under steady-state conditions in this work as it is done in most studies, the inclusion of such transient behavior may be interesting to understand its effect on the contacting configuration and its impact on stack performance. For this, it may be necessary to calibrate the model parameters to a thermal cycling suitable use case.

Another aspect could be the formation of oxide layers on metallic components of the SOC, which may cause degradation over prolonged operational times [161, 162]. The effect of this oxidation is not incorporated into the proposed model and may be seen as an area for improvement. The offset formulation may be adapted to account for this behavior by introducing an additional strain component that varies as a function of operation time, thereby increasing the total effective strain. With suitable enhancements to the current framework of constitutive equations, along with appropriate thermodynamic considerations, these degradation mechanisms could be considered as a potential scope for incorporating this phenomenon.

9.2 Outlook and further scope

9.2.1 Incorporation of design specific components into the model

The work presented in this dissertation focuses mainly on the active area region of the SOC. However, for a practical application, there may be significant interaction between the active area with the sealing gaskets which may have some influence on the force distribution in the stack. In order to account for these effects, the inclusion of sealing gaskets, welded cells and other design specific components must be considered to obtain the final contacting configuration of a specific stack design.

9.2.2 Parameter optimization

Using the proposed workflow, it becomes possible to optimize several parameters like stacking force, geometric design of contacts, materials used etc. for achieving the desired level of contacting in the active area. Moreover, it also becomes possible to define a limiting range of allowable tolerances from the perspective of process optimization.

9.2.3 Optimization of stacking sequence

On validating the established simulation methods with experimental tests, it is now possible to obtain the contact configuration for every manufactured repeat unit in a stack after mechanical stacking without costly experiments and minimal computational effort. Upon measuring manufactured parts, the entire simulation workflow is automated in PYTHON to create a continuous generation of data of contact patterns after the stacking process.

One criteria for process optimization without change in design or material is the sequence in which cells may be stacked. This was initiated by using the same cells to simulate different stacking sequences to observe a difference in contacting quality. This indicates that there may be an optimal sequence for stacking any given set of manufactured cells, having specified their variability in their bending profiles and their contact height distributions.

On attempting this approach for limited number of trials, it was seen that some configurations of stacking sequences showed a slightly more homogenous contacting quality than others. This suggests potential for further investigation in the direction of creating data driven approaches like neural networks to identify the optimal stacking sequence of manufactured cells.

10 List of Publications

Journal papers

- Pinto, R.; Welschinger, F.; Giesselmann, N.; Reinshagen, H.; Menzler, N.H.; A constitutive model for homogenized solid oxide cell contacts with dimensional tolerances. International Journal of Hydrogen Energy, 80, 343-356,(2024). https://doi.org/10.1016/j.ijhydene.2024.07.092
- Pinto, R.; Welschinger, F.; Giesselmann, N.; Reinshagen, H.; Vaßen, R.; Menzler, N.H.; Multiscale modeling approach of solid oxide cell contacts with dimensional tolerances for estimating electrical contact resistance. International Journal of Hydrogen Energy, 91, 1274-1288,(2024). https://doi.org/10.1016/j.ijhydene.2024.10.114
- Pinto, R.; Giesselmann, N.; Reinshagen, H.; Menzler, N.H.; Evaluation of an effective mechanical stiffness for rough, porous coating layers of SOC interconnects using a data driven approach. Surfaces and Interfaces, 72, 107204,(2025). https://doi.org/10.1016/j.surfin.2025.107204

Conference proceedings

- Pinto, R.; Welschinger, F.; Giesselmann, N.; Reinshagen, H.; Menzler, N.H.; Homogenization of fuel cell interconnects to determine the contacting configuration in a stack; A1516-10228; EFCF 2024: 16^{th} European SOFC & SOEC Forum; 2-5 July 2024, Lucerne Switzerland. https://www.efcf.com/community/live-5-7-july/proceedings/mount-point-of-poc-2024/pocaz

Patents

- Pinto, R.; Welschinger, F.; Verfahren zur Herstellung eines elektrochemischen Stacks, elektrochemischer Stack; Status: Application filed; Application date: 12^{th} December, 2023; Application number: 102023212085.2.

Bibliography

[1] S. Steinbach and N. Bunk, "The future european hydrogen market: Market design and policy recommendations to support market development and commodity trading," *International Journal of Hydrogen Energy*, vol. 70, pp. 29–38, 2024.

[2] G. Zhao, E. Nielsen, E. Troncoso, K. Hyde, J. Romeo, and M. Diderich, "Life cycle cost analysis: A case study of hydrogen energy application on the orkney islands," *International Journal of Hydrogen Energy*, vol. 44, pp. 9517–9528, 2019.

[3] M. Khaleel, Z. Lin, P. Singh, W. Surdoval, and D. Collin, "A finite element analysis modeling tool for solid oxide fuel cell development: coupled electrochemistry, thermal and flow analysis in marc®," *Journal of Power Sources*, vol. 130, pp. 136–148, 2004.

[4] D. Chen, Y. Xu, B. Hu, C. Yan, and L. Lu, "Investigation of proper external air flow path for tubular fuel cell stacks with an anode support feature," *Energy Conversion and Management*, vol. 171, pp. 807–814, 2018.

[5] J. Duhn, A. Jensen, S. Wedel, and C. Wix, "Optimization of a new flow design for solid oxide cells using computational fluid dynamics modelling," *Energy Conversion and Management*, vol. 336, pp. 261–271, 2016.

[6] B. Lin, Y. Shi, M. Ni, and N. Cai, "Numerical investigation on impacts on fuel velocity distribution nonuniformity among solid oxide fuel cell unit channels," *International Journal of Hydrogen Energy*, vol. 40, pp. 3035–3047, 2015.

[7] A. Nakajo, F. Mueller, J. Brouwer, J. Van herle, and D. Favrat, "Mechanical reliability and durability of sofc stacks. part i: Modelling of the effect of operating conditions and design alternatives on the reliability," *International Journal of Hydrogen Energy*, vol. 37, pp. 9249–9268, 2012.

[8] A. Nakajo, F. Mueller, J. Brouwer, J. Van herle, and D. Favrat, "Mechanical reliability and durability of sofc stacks. part ii: Modelling of mechanical failures during ageing and cycling," *International Journal of Hydrogen Energy*, vol. 37, pp. 9269–9286, 2012.

[9] G. Jing, C. Hu, Y. Qin, X. Sun, and T. Ma, "Complex mechanisms of pemfc performance variations influenced by both structural deformation and contact resistance under the clamping force," *International Journal of Hydrogen Energy*, vol. 58, pp. 137–148, 2024.

[10] C. Wu, Z. Chen, and G. Tang, "Component tolerance design for minimum quality loss and manufacturing cost," *Computers in Industry*, vol. 35, pp. 223–232, 1998.

[11] D. Parkinson, "Tolerancing of component dimensions in cad," *Computer-Aided Design*, vol. 35, pp. 25–32, 1984.

[12] S. Golkhatmi, M. Asghar, and P. Lund, "A review on solid oxide fuel cell durability: Latest progress, mechanisms, and study tools," *Computer-Aided Design*, vol. 161, p. 112339, 2022.

[13] K. Kendall and M. Kendall, *High-Temperature Solid Oxide Fuel Cells for the 21st Century: Fundamentals, Design and Applications*. Elsevier, 2015.

[14] C. Lenser, J. Zurek, D. Naumenko, C.-A. Thieu, J.-W. Son, U. de Haart, Q. Fang, L. Blum, and N. Menzler, "Performance analysis of a planar solid oxide fuel cell stack between 750°C and 500°C," *Journal of Power Sources*, vol. 474, p. 228671, 2020.

[15] W. Wu, L. Wang, M. Guan, Y. Zhen, and W. Wang, "Effect of contact method between interconnects and electrodes on area specific resistance in planar solid oxide fuel cells," *Fuel Cells*, vol. 13, p. 743–750, 2013.

[16] M. Shen and P. Zhang, "Progress and challenges of cathode contact layer for solid oxide fuel cell," *International Journal of Hydrogen Energy*, vol. 45, pp. 33876–33894, 2020.

[17] G. Ghiara, P. Piccardo, V. Bongiorno, L. Repetto, C. Geipel, and R. Spotorno, "Characterization of metallic interconnects extracted from solid oxide fuel cell stacks operated up to 20,000 h in real life conditions: The fuel side," *International Journal of Hydrogen Energy*, vol. 46, pp. 23815–23827, 2021.

[18] F. Tietz, H.-P. Buchkremer, and D. Stoever, "Components manufacturing for solid oxide fuel cells," *Solid State Ionics*, vol. 152-153, pp. 373–381, 2002.

[19] K. Kendall, "Composite sofc designs for small scale cogeneration," *The Electrochemical Society*, vol. ECS Proceedings Volumes, Volume 1993-4, pp. 813–821, 1993.

[20] Z. Wu, Y. Zhou, G. Lin, S. Wang, and J. Hub, "An improved model for predicting electrical contact resistance between bipolar plate and gas diffusion layer in proton exchange membrane fuel cells," *Journal of Power Sources*, vol. 182, pp. 265–269, 2008.

[21] J. Riba and P. Bas-Calopa, "Analysing the pressure effect on the contact resistance of electrical connections," *European Journal of Physics*, vol. 43, p. 12, 2022.

[22] T. Deya, D. Singdeo, J. Deshpande, and P. Ghosh, "Structural analysis of solid oxide fuel cell under externally applied compressive pressure," *Energy Procedia*, vol. 54, pp. 789–795, 2014.

[23] G. Almutairi, "A simple model for solid oxide fuel cells," *Energy Transitions*, vol. 4, pp. 163–167, 2020.

[24] Z. Z. Chen, X. Wang, N. Brandon, and A. Atkinson, "Numerical study of solid oxide fuel cell contacting mechanics," *Fuel Cells*, vol. 1, p. 42–50, 2018.

[25] M. Kusnezoff, N. Trofimenko, M. Müller, and A. Michaelis, "Influence of electrode design and contacting layers on performance of electrolyte supported sofc/soec single cells," *materials*, vol. 9, p. 906, 2016.

[26] J. Ma, S. Ma, X. Zhang, D. Chen, and J. He, "Development of large-scale and quasi multi-physics model for whole structure of the typical solid oxide fuel cell stacks," *Sustainability*, vol. 10, p. 3094, 2018.

[27] C. Carral and P. Mele, "A numerical analysis of pemfc stack assembly through a 3d finite element model," *International Journal of Hydrogen Energy*, vol. 39, pp. 4516–4530, 2014.

[28] W. Cai, Q. Zheng, J. Yuan, W. Yu, Z. Yin, Y. Wu, and Z. Zhang, "Thermo-electro-chemo-mechanical coupled modeling of solid oxide fuel cell with lscf-gdc composite cathode," *International Journal of Molecular Sciences*, vol. 24, p. 4137, 2023.

[29] X.-Y. Miao, O. B. Rizvandi, M. Navasa, and H. L. Frandsen, "Modelling of local mechanical failures in solid oxide cell stacks," *Applied Energy*, vol. 291, p. 116901, 2021.

[30] M. Rabuni, N. Vatcharasuwan, T. Li, and K. Li, "High performance micro-monolithic reversible solid oxide electrochemical reactor," *Journal of Power Sources*, vol. 458, p. 228026, 2020.

[31] S. O.Z. and M. Orhan, "High performance micro-monolithic reversible solid oxide electrochemical reactor," *Renewable Sustainable Energy Reviews*, vol. 31, pp. 810–853, 2014.

[32] S. Campanari, L. Mastropasqua, M. Gazzani, P. Chiesa, and M. Romano, "Predicting the ultimate potential of natural gas sofc power cycles with co 2 capture e part a: methodology and reference cases," *Journal of Power Sources*, vol. 324, pp. 598–614, 2016.

[33] "How does our sofc system work?."

[34] Z. Zakaria, Z. Awang Mat, S. Abu Hassan, and Y. Boon Kar, "A review of solid oxide fuel cell component fabrication methods toward lowering temperature," *Journal of Energy Research*, vol. 44, pp. 594–611, 2020.

[35] A. Stambouli and E. Traversa, "Solid oxide fuel cells (sofcs): a review of an environmentally clean and efficient source of energy," *Renewable Sustainable Energy Reviews*, vol. 6, pp. 433–455, 2002.

[36] N. Mahato, A. Banerjee, A. Gupta, S. Omar, and K. Balani, "Progress in material selection for solid oxide fuel cell technology: a review.," *Progress in Material Science*, vol. 72, pp. 141–337, 2015.

[37] T. Adams, J. Nease, D. Tucker, and P. Barton, "Energy conversion with solid oxide fuel cell systems: a review of concepts and outlooks for the short- and long-term," *Industrial and Engineering Chemistry Research*, vol. 52, pp. 3089–3111, 2013.

[38] Y. Wang, W. Li, L. Ma, W. Li, and X. Liu, "Degradation of solid oxide electrolysis cells: phenomena, mechanisms, and emerging mitigation strategiesda review," *Journal of Materials Science and Technology*, vol. 55, pp. 35–55, 2020.

[39] X. Wu, W. Zhang, B. Yu, X. Guo, and J. Xu, "Research progress on the interconnect coating technology for the sofc/soec," *Xiyou Jinshu Cailiao Yu Gongcheng/Rare Metal Materials and Engineering*, vol. 44, pp. 1555–1560, 2015.

[40] N. Minh, "Ceramic fuel cells," *Journal of American Ceramic Society*, vol. 76, p. 563–588, 1993.

[41] N. Minh and T. Takahashi, *Science and technology of ceramic fuel cells*. Elsevier, Oxford, 1995.

[42] B. Boukamp, "Fuel cells: The amazing perovskite anode," *Nature Materials*, vol. 2, p. 294–296, 2003.

[43] O. Yamamoto, Y. Arachi, H. Sakai, Y. Takeda, N. Imanishi, Y. Mizutani, M. Kawai, and Y. Nakamura, "Zirconia based oxide ion conductors for solid oxide fuel cells," *Ionics*, vol. 4, p. 403–408, 1998.

[44] M. Choolaei, Q. Cai, R. Slade, and B. Amini Horri, "Nanocrystalline gadolinium-doped ceria (gdc) for sofcs by an environmentally-friendly single step method," *Ceramics International*, vol. 44, pp. 13286–13292, 2018.

[45] S. Badwal, "Stability of solid oxide fuel cell components," *Solid State Ionics*, vol. 143, p. 39–46, 2001.

[46] A. Hernandez, L. Mogni, and A. Caneiro, "Ruddlesden-popper phase materials for solid oxide fuel cell cathodes: A short review," *International Journal of Hydrogen Energy*, vol. 35, p. 6031–6036, 2010.

[47] W. Tinglian, L. Xiaofei, K. Chukun, and W. Weppner, "Conductivity of mgo-doped zro2," *Solid State Ionics*, vol. 18–19, pp. 715–719, 1986.

[48] S. Skinner and J. Kilner, "Oxygen ion conductors," *Materials today*, vol. 6, pp. 30–37, 2003.

[49] A. Jacobson, "Materials for solid oxide fuel cells," *Chemistry of Materials*, vol. 22, p. 660–674, 2010.

[50] M. Han, X. Tang, H. Yin, and S. Peng, "Fabrication, microstructure and properties of a ysz electrolyte for sofcs," *Journal of Power Sources*, vol. 165, p. 757–763, 2007.

[51] T. Ishihara, H. Matsuda, and Y. Takita, "Doped lagao3 perovskite type oxide as a new oxide ionic conductor," *Journal of the American Chemical Society*, vol. 116, p. 3801–3803, 1994.

[52] B. Shri Prakash, S. Kumar, and S. Aruna, "Properties and development of ni/ysz as an anode material in solid oxide fuel cell: a review," *Renewable Sustainable Energy Reviews*, vol. 36, pp. 149–179, 2014.

[53] J. Lee, J. Park, and Y. Shul, "Tailoring gadolinium-doped ceria-based solid oxide fuel cells to achieve 2wcm2 at 550c," *Nature Communications*, vol. 5, p. 4050, 2014.

[54] H. Shabri, M. Othman, M. Mohamed, T. Kurniawan, and S. Jamil, "Recent progress in metal-ceramic anode of solid oxide fuel cell for direct hydrocarbon fuel utilization: a review," *Fuel Processing Technology*, vol. 212, p. 106626, 2021.

[55] S. Tao and J. Irvine, "A redox-stable efficient anode for solid-oxide fuel cells," *Nature Materials*, vol. 2, p. 320–323, 2003.

[56] W. Zhu and S. Deevi, "A review on the status of anode materials for solid oxide fuel cells," *Materials Science and Engineering A*, vol. 362, p. 228–239, 2003.

[57] S. Tao and J. Irvine, "Discovery and characterization of novel oxide anodes for solid oxide fuel cells," *The Chemical Record*, vol. 4, p. 83–95, 2004.

[58] J. Mah, A. Muchtar, M. Somalu, and M. Ghazali, "Metallic interconnects for solid oxide fuel cell: A review on protective coating and deposition techniques," *Energy Technology*, vol. 42, pp. 9219–9229, 2017.

[59] J. Zhu, D. Chesson, and Y. Yu, "Review—(mn,co)3o4-based spinels for sofc interconnect coating application," *Journal of The Electrochemical Society*, vol. 168, p. 114519, 2021.

[60] N. Gruenwald, D. Sebold, Y. Sohn, N. Menzler, and R. Vaßen, "Self-healing atmospheric plasma sprayed mn1.0co1.9fe0.1o4 protective interconnector coatings for solid oxide fuel cells," *Journal of Power Sources*, vol. 363, pp. 185–192, 2017.

[61] B. Timurkutluk, C. Timurkutluk, M. Mat, and Y. Kaplan, "A review on cell/stack designs for high performance solid oxide fuel cells," *Renewable and Sustainable Energy Reviews*, vol. 56, pp. 1101–1121, 2016.

[62] D. Udomsilp, C. Lenser, O. Guillon, , and N. Menzler, "Performance benchmark of planar solid oxide cells based on material development and designs," *Energy Technology*, vol. 9, p. 2001062, 2021.

[63] X. Fang, J. Zhu, and Z. Lin, "Effects of electrode composition and thickness on the mechanical performance of a solid oxide fuel cell," *Energies*, vol. 11, p. 1735, 2018.

[64] M. Chelmehsara and M. J., "Techno-economic comparison of anode-supported, cathode-supported, and electrolyte-supported sofcs," *International Journal of Hydrogen Energy*, vol. 43, pp. 15521–15530, 2018.

[65] D. Panthi, N. Hedayat, T. Woodson, B. Emley, and Y. Du, "Tubular solid oxide fuel cells fabricated by a novel freeze casting method," *American Ceramic Society*, vol. 103, pp. 878–888, 2020.

[66] M. Khan, A. Iltaf, H. Ishfaq, F. Khan, W. Tanveer, R. Song, and et al., "Flat-tubular solid oxide fuel cells and stacks: a review," *Journal of Asian Ceramic Societies*, vol. 9, pp. 745–770, 2021.

[67] G. Li, Y. Gou, J. Qiao, W. Sun, Z. Wang, and K. Sun, "Recent progress of tubular solid oxide fuel cell: from materials to applications," *Journal of Power Sources*, vol. 477, p. 228693, 2020.

[68] K. Howe, G. Thompson, and K. K., "Micro-tubular solid oxide fuel cells and stacks," *Journal of Power Sources*, vol. 196, pp. 1677–1686, 2020.

[69] Ceres Intellectual Property Company Limited, WO 2020/1264S6 A1, *Fuel cell unit and fuel cell stack*, 2020.

[70] R. Leah, A. Bone, M. Lankin, A. Selcuk, M. Rahman, A. Clare, L. Rees, S. Phillip, S. Mukerjee, and M. Selby, "Ceres power steel cell technology: Rapid progress towards a truly commercially viable sofc," *The Electrochemical society*, vol. 8, pp. 95–107, 2015.

[71] P. Bance, N. Brandon, B. Girvan, P. Holbeche, S. O'Dea, and B. Steele, "Spinning-out a fuel cell company from a uk university—2 years of progress at ceres power," *Journal of Power Sources*, vol. 131, pp. 86–90, 2004.

[72] N. P. Brandon, D. Corcoran, D. Cummins, A. Duckett, K. El-Khoury, D. Haigh, R. Leah, G. Lewis, N. Maynard, T. McColm, R. Trezona, A. Selcuk, and M. Schmidt, "Development of metal supported solid oxide fuel cells for operation at 500–600c," *Fuel Cells: Materials, Processing And Manufacturing Technologies*, vol. 13, p. 253–256, 2004.

[73] R. Leah, A. Bone, A. Selcuk, D. Corcoran, M. Lankin, Z. Dehaney-Steven, M. Selby, and P. Whalen, "Development of highly robust, volume-manufacturable metal-supported sofcs for operation below 600c," *The Electrochemical society*, vol. 35, pp. 351–367, 2011.

[74] R. Leah, A. Bone, P. Hjalmarsson, A. Selcuk, M. Lankin, M. Rahman, J. Felix, F.and De Vero, C. Macauley, and C. Charbonneau, "Commercialization of ceres

steelcell® technology for power generation and electrolysis," *The Electrochemical society*, vol. 111, pp. 121–131, 2023.

[75] R. Leah, A. Bone, M. Lankin, A. Selcuk, M. Rahman, A. Clare, G. Reade, F. Felix, J. De Vero, and X. Wang, "Commercialization of the ceres power steelcell technology: Latest update," *The Electrochemical society*, vol. 103, pp. 679–684, 2021.

[76] R. Leah, M. Lankin, A. Bone, A. Selcuk, R. Pierce, L. Rees, D. Corcoran, P. Muhl, Z. Dehaney-Steven, C. Brackenbury, and S. Mukerjee, "Towards a fully redox stable sofc: Cell development at ceres power," *The Electrochemical society*, vol. 7, pp. 849–856, 2013.

[77] J. Fergus, "Metallic interconnects for solid oxide fuel cells," *Materials Science and Engineering: A*, vol. 397, pp. 271–283, 2005.

[78] D. M. Bastidas, "High temperature corrosion of metallic interconnects in solid oxide fuel cells," *Revista de Metalurgia*, vol. 42, pp. 425–443, 2006.

[79] Z. Shao and M. Tade, *Intermediate-Temperature Solid Oxide Fuel Cells*. Springer, 2016.

[80] J. Wu and X. Liu, "Recent development of sofc metallic interconnect," *Revista de Metalurgia*, vol. 26, pp. 293–305, 2010.

[81] W. Chang, J. Hwang, F. Weng, and S. Chan, "Effect of clamping pressure on the performance of a pem fuel cell," *Journal of Power Sources*, vol. 166, p. 149–154, 2007.

[82] Y. Gao, M. Zhang, W. Fu, M. Hu, H. Tong, and Z. Tao, "A comprehensive review of recent progresses in cathode materials for proton-conducting sofcs," *Energy Reviews*, vol. 2, p. 100038, 2023.

[83] S. Hussain and L. Yangping, "Review of solid oxide fuel cell materials: cathode, anode, and electrolyte," *Energy Transitions*, vol. 4, p. 113–126, 2020.

[84] P. Pianko-Oprych, T. Zinko, and Z. Jaworski, "Modeling of thermal stresses in a microtubular solid oxide fuel cell stack," *Journal of Power Sources*, vol. 300, pp. 10–23, 2015.

[85] T. Hsu, H. Kim, J. Mason, M. Rubayyat, W. Epting, H. Abernathy, G. Hackett, S. Litster, A. Rollett, and P. Salvador, "High performance finite element simulations of infiltrated solid oxide fuel cell cathode microstructures," *Journal of Power Sources*, vol. 541, p. 231652, 2022.

[86] M. Andersson, J. Yuan, and B. Sunden, "Sofc cell design optimization using the finite element method based cfd approach," *Fuel Cells*, vol. 14, pp. 177–188, 2014.

[87] W. Lai, D. Rubin, and E. Krempl, *Introduction to the mechanics of a continuous medium*. Elsevier, 2010.

[88] L. Malvern, *Introduction to the mechanics of a continuous medium*. Prentice-Hall, 1969.

[89] G. Maugin, *The Thermomechanics of Plasticity and Fracture*. Cambridge University Press, 1992.

[90] J. Hutchinson, "Bounds and self-consistent estimates for creep of polycrystalline materials," *Proceedings of Royal Society of London A*, vol. 348, p. 101–127, 1976.

[91] R. Hill, "Elastic properties of reinforced solids: Some theoretical principles," *Journal of the Mechanics and Physics of Solids*, vol. 11, p. 357–372, 1963.

[92] R. Hill, "The essential structure of constitutive laws for metal composites and polycrystals," *Journal of the Mechanics and Physics of Solids*, vol. 15, p. 79–95, 1967.

[93] W. Han and B. Reddy, *Plasticity: Mathematical theory and numerical analysis*. Springer, 1999.

[94] B. Reddy, *Introductory functional analysis: with applications to boundary value problems and finite elements*. Springer Science and Business Media, 1998.

[95] C. Miehe, N. Apel, and M. Lambrecht, "Anisotropic additive plasticity in the logarithmic strain space: modular kinematic formulation and implementation based on incremental minimization principles for standard materials," *Computer methods in applied mechanics and engineering*, vol. 191, pp. 5383–5425, 2002.

[96] C. Miehe, J. Schotte, and M. Lambrecht, "Homogenization of inelastic solid materials at finite strains based on incremental minimization principles. application to the texture analysis of polycrystals," *Journal of the Mechanics and Physics of Solids*, vol. 50, pp. 2123–2167, 2002.

[97] J. Simo and M. Ortiz, "A unified approach to finite deformationelastoplastic analysis based on the use of hyperelastic constitutive equations," *Computer methods in applied mechanics and engineering*, vol. 49, pp. 221–245, 1985.

[98] D. Tsalis, G. Chatzigeorgiou, and C. Tsakmakis, "Dissipation inequality based periodic homogenization of wavy materials," *Composites Part B*, vol. 76, p. 89–104, 2015.

[99] P. Steinmann, *Geometrical Foundations of Continuum Mechanics: An Application to First- and Second-Order Elasticity and Elasto-Plasticity.* Springer, 2015.

[100] B. Coleman and M. Gurtin, "Thermodynamics with internal state variables," *The Journal of Chemical Physics*, vol. 47, p. 597–613, 1967.

[101] G. Maugin, *The Thermomechanics of Nonlinear Irreversible Behaviors – An Introduction.* World Scientific, 1999.

[102] S. Nemat-Nasser, "Decomposition of strain measures and their rates in finite deformation elastoplasticity," *International Journal of Solids and Structures*, vol. 15, pp. 155–166, 1978.

[103] J. Simo and R. Taylor, "Consistent tangent operators for rate-independent elastoplasticity," *Computer methods in applied mechanics and engineering*, vol. 48, pp. 101–118, 1985.

[104] J. C. Simo and T. J. R. Hughes, *Computational Inelasticity.* Springer, 1998.

[105] J. Simo and L. Vu-quoc, "Three dimensional finite-strain rod model. part ii: Computational aspects," *Computer methods in applied mechanics and engineering*, vol. 58, pp. 79–116, 1986.

[106] J. Simo, "A finite strain beam formulation. the three-dimensional dynamic problem. part i," *Computer methods in applied mechanics and engineering*, vol. 49, pp. 55–70, 1985.

[107] R. Hill, "Classical plasticity: A retrospective view and a new proposal," *Journal of the Mechanics and Physics of Solids*, vol. 42, pp. 1803–1816, 1994.

[108] F. Praud, *Multi-scale modelling of thermoplastic-based woven composites, cyclic and time-dependent behaviour.* Phd thesis, l'École Nationale Supérieure d'Arts et Métiers, November 2018.

[109] D. Naake, *Simulation of damage mechanisms in weave reinforced materials based on multiscale modeling.* PhD thesis, Karlsruhe Institute of Technology, 2019.

[110] J. Michel, H. Moulinec, and P. Suquet, "Effective properties of composite materials with periodic microstructure: a computational approach," *Computer Methods in Applied Mechanics and Engineering*, vol. 172, p. 109–143, 1999.

[111] R. Hill, "Continuum micro-mechanics of elastoplastic polycrystals," *Journal of the Mechanics and Physics of Solids*, vol. 13, p. 89–101, 1965.

[112] R. Hill and J. Rice, "On constitutive macro-variables for heterogeneous solids at finite strain," *Proceedings of the Royal Society of London A*, vol. 326, p. 131–147, 1972.

[113] "Reversible solid oxide electrochemical cell."

[114] C. Berges, J. Hidalgo, R. Andújar, R. Campana, and G. Herranz, "Prospects of producing solid oxide fuels interconnectors processed by metal injection moulding," *Results in Engineering*, vol. 11, p. 100268, 2021.

[115] M. Xu, T. Li, Y. Ming, and M. Andersson, "Solid oxide fuel cell interconnect design optimization considering the thermal stresses," *Science Bulletin*, vol. 61, pp. 1333–1344, 2016.

[116] R. Leah, M. Lankin, A. Bone, S. Mukerjee, and M. Selby, "Kinetics of internal methane reforming on the anodes of low temperature ceres power steel cell sofcs," *The Electrochemical society*, vol. MA2015-03, pp. 238–238, 2015.

[117] M. Tomas, A. Visibile, J.-E. Svensson, and J. Froitzheim, "Novel coatings for protecting solid oxide fuel cell interconnects against the dual-atmosphere effect," *International Journal of Hydrogen Energy*, vol. 48, pp. 18405–18419, 2023.

[118] H. Abdoli, M. Sebastian, and H. Farnoush, "Effect of interconnect coating procedure on solid oxide fuel cell performance," *Material Letters*, vol. 259, p. 126898, 2020.

[119] F. Shen, S. A. Ibanez, and M. C. Tucker, "Dynamic oxidation of (mn,co) 3o 4-coated interconnects for solid oxide electrolysis cells," *International Journal of Hydrogen Energy*, 2023.

[120] VDM Metals International GmbH, *Werkstoffdatenblatt Nr. 4146 VDM® Crofer 22 APU*, 2022.

[121] Dassault Systèmes Simulia Corporation, *ABAQUS documentation*, 2021.

[122] T. T. Molla, K. Kwok, and H. L. Frandsen, "Efficient modeling of metallic interconnects for thermo-mechanical simulation of sofc stacks: Homogenized behaviors and effect of contact," *International Journal of Hydrogen Energy*, vol. 41, pp. 6433–6444, 2016.

[123] M. Peksen, "Numerical thermomechanical modelling of solid oxide fuel cells," *Progress in Energy and Combustion Science*, vol. 48, pp. 1–20, 2015.

[124] M. Navasa, X.-Y. Miao, and H. L. Frandsen, "A fully-homogenized multiphysics model for a reversible solid oxide cell stack," *International Journal of Hydrogen Energy*, vol. 44, pp. 23330–23347, 2019.

[125] H. Frandsen, B. Chatzichristodoulou, C.and Charlas, R. Kiebach, K. Kwok, P. Norby, and P. Hendriksen, "Fast relaxation of stresses in solid oxide cells through reduction. part i: Macro-stresses in the cell layers," *International Journal of Hydrogen Energy*, vol. 46, pp. 1548–1559, 2021.

[126] F. Harewood and P. McHugh, "Investigation of finite element mesh independence in rate dependent materials," *Computational Materials Science*, vol. 37, p. 442–453, 2006.

[127] L. Anand and M. Kothari, "A computational procedure for rate-independent crystal plasticity," *Journal of Physics and Mechanics of Solids*, vol. 44, pp. 525–558, 1996.

[128] W. Feather, H. Lim, and M. Knezevic, "A numerical study into element type and mesh resolution for crystal plasticity finite element modeling of explicit grain structures," *Computational Mechanics*, vol. 67, pp. 33–55, 2021.

[129] W. Cai, Q. Zheng, J. Yuan, W. Yu, Z. Yin, Y. Wu, and Z. Zhang, "Thermo-electro-chemo-mechanical coupled modeling of solid oxide fuel cell with lscf-gdc composite cathode," *International Journal of Molecular Sciences*, vol. 24, p. 4137, 2023.

[130] S. Li, N. Warrior, Z. Zou, and F. Almaskari, "A unit cell for fe analysis of materials with the microstructure of a staggered pattern," *Composites: Part A*, vol. 42, pp. 801–811, 2011.

[131] G. Chatzigeorgiou, F. Meraghni, and N. Charalambakis, *Multiscale Modeling Approaches for Composites*. Elsevier, 2022.

[132] G. Chatzigeorgiou, F. Meraghni, Y. Chemisky, and N. Charalambakis, *Thermomechanical Behavior of Dissipative Composite Materials*. Elsevier, 2018.

[133] G. Chatzigeorgiou, F. Meraghni, Y. Chemisky, and N. Charalambakis, "Periodic homogenization for fully coupled thermomechanical modeling of dissipative generalized standard materials," *International Journal of Plasticity*, vol. 81, pp. 18–39, 2016.

[134] W. Feather, H. Lim, and M. Knezevic, "Four exact relations for the effective relaxation function of linear viscoelastic composites," *Comptes Rendus Mecanique*, vol. 340, p. 387–399, 2012.

[135] P. Suquet, *Elements of Homogenization for Inelastic Solid Mechanics*. Springer, 1987.

[136] J. Simo and C. Miehe, "Associative coupled thermoplasticity at finite strains: Formulation, numerical analysis and implementation," *Computer Methods in Applied Mechanics and Engineering*, vol. 98, p. 41–104, 1992.

[137] L. Tartar, *Nonlinear Constitutive Relations and Homogenization*. 1978.

[138] M. Tsuda, E. Takemura, T. Asada, N. Ohno, and T. Igari, "Homogenized elastic-viscoplastic behavior of plate-fin structures at high temperatures: Numerical analysis and macroscopic constitutive modeling," *International Journal of Mechanical Sciences*, vol. 52, pp. 648–656, 2010.

[139] E. Alizadeh, M. M. Barzegari, M. Momenifar, M. Ghadimi, and S. H. M. Saadat, "Investigation of contact pressure distribution over the active area of pem fuel cell stack," *International Journal of Hydrogen Energy*, vol. 41, pp. 3062–3071, 2016.

[140] J. H. Zhu and H. Ghezel-Ayagh, "Cathode-side electrical contact and contact materials for solid oxide fuel cell stacking: a review," *International Journal of Hydrogen Energy*, vol. 42, pp. 24278–24300, 2017.

[141] C.-H. Chien, Y.-H. Hu, T.-H. Su, H.-T. Liu, T. Wang, C., P.-F. Yang, and Y.-X. Lu, "Effects of bolt pre-loading variations on performance of gdl in a bolted pemfc by 3-d fem analysis," *Energy*, vol. 113, pp. 1174–1187, 2016.

[142] W. Jiang, K. Zhang, X. Huang, Z. Cai, J. Zheng, Y. Kai, B. Zheng, and K. Song, "Influence of clamping pressure on contact pressure uniformity and electrical output performance of proton exchange membrane fuel cell," *Applied Energy*, vol. 353, p. 122021, 2024.

[143] D. Kennouche, Q. Fang, L. Blum, and D. Stolten, "Analysis of the cathode electrical contact in sofc stacks," *Journal of The Electrochemical Society*, vol. 165, pp. 677–683, 2018.

[144] A. Pfister, *Umbau eines 3D-Scan-Messstands zur geometrischen Erfassung von Festoxid-Brennstoffzellen-Komponenten sowie Erstellung und Validierung der erforderlichen Messroutinen.* thesis, Hochschule Coburg, September 2022.

[145] J. Ulloa, R. Alessi, J. Wambacq, G. Degrande, and F. Stijn, "On the variational modeling of non-associative plasticity," *International Journal of Solids and Structures*, vol. 217–218, pp. 272–296, 2021.

[146] V. S. Deshpande and N. A. Fleck, "Isotropic constitutive models for metallic foams," *Journal of the Mechanics and Physics of Solids*, vol. 48, pp. 1253–1283, 2000.

[147] Z. Xue and J. W. Hutchinson, "Constitutive model for quasi-static deformation of metallic sandwich cores," *Composites: Part A*, vol. 61, pp. 2205–2238, 2004.

[148] Z. Xue and J. Hutchinson, "Preliminary assessment of sandwich plates subject to blast loads," *International Journal of Mechanical Sciences*, vol. 45, p. 687–705, 2003.

[149] R. Hill, "A theory of yielding an plastic flow of anisotropic materials," *Proceedings of The Royal Society A*, vol. 193, pp. 281–297, 1948.

[150] R. Pinto, F. Welschinger, N. Giesselmann, H. Reinshagen, and N. Menzler, "A constitutive model for homogenized solid oxide cell contacts with dimensional tolerances," *International Journal of Hydrogen Energy*, vol. 80, pp. 343–356, 2024.

[151] R. Pinto, F. Welschinger, N. Giesselmann, H. Reinshagen, R. Vaßen, and N. Menzler, "Multiscale modeling approach of solid oxide cell contacts with dimensional tolerances for estimating electrical contact resistance," *International Journal of Hydrogen Energy*, vol. 91, pp. 1274–1288, 2024.

[152] D. Udomsilp, D. Roehrens, N. Menzler, R. Conradt, and O. Guillon, "Characterization of the contact resistance of cathodic sofc contacting," *The Electrochemical Society*, vol. 68, pp. 751–756, 2015.

[153] F. Schaldach, *Untersuchungen zum Einfluss der Fügespannung sowie thermischer Belastung auf das Leistungspotenzial einer Festoxid-Brennstoffzelle.* thesis, Technische Universität Dortmund, December 2021.

[154] F. Dorner, C. Korblein, and C. Schindler, "On the accuracy of the pressure measurement film in hertzian contact situations similar to wheel-rail contact applications," *Wear*, vol. 317, pp. 241–245, 2014.

[155] J. Lekue, F. Dorner, and C. Schindle, "Calibration of a finite element model of prescale film for wheel-rail normal contact area measurements," *Meccanica*, vol. 56, p. 3097–3106, 2021.

[156] J.-J. Liaua, C.-K. Chenga, C.-H. Huanga, and W.-H. Loc, "Effect of fuji pressure sensitive film on actual contact characteristics of artificial tibiofemoral joint," *Clinical Biomechanics*, vol. 17, pp. 698–704, 2002.

[157] S. Glaser, *Optimierung der Krafteinleitung in den Brennstoffzellenstack zum Erreichen einer homogenen mechanischen und elektrischen Kontaktierung des Zellstapels*. thesis, Dualen Hochschule Baden-Württemberg Mosbach, September 2022.

[158] J. Pan, J. Yang, D. Yan, J. Pu, B. Chi, and J. Li, "Effect of thermal cycling on durability of a solid oxide fuel cell stack with external manifold structure," *International Journal of Hydrogen Energy*, vol. 45, pp. 17927–17934, 2020.

[159] M. Hanasaki, C. Uryu, T. Daio, T. Kawabata, Y. Tachikawa, S. Lyth, Y. Shiratori, S. Taniguchi, and K. Sasaki, "Sofc durability against standby and shutdown cycling," *Journal of The Electrochemical Society*, vol. 161, pp. F850–F860, 2014.

[160] Y. Matus, L. De Jonghe, C. Jacobson, and S. Visco, "Metal-supported solid oxide fuel cell membranes for rapid thermal cycling," *Solid state ionics*, vol. 176, pp. 443–449, 2005.

[161] G. Yang, A. Potter, and J. Joy Sumner, "An overview on oxidation of metallic interconnects in solid oxide fuel cells under various atmospheres," *International Journal of Hydrogen Energy*, vol. 99, pp. 974–984, 2025.

[162] Z. Yang, G.-G. Xia, M. Walker, C.-M. Wang, J. Stevenson, and S. P., "High temperature oxidation/corrosion behavior of metals and alloys under a hydrogen gradient," *International Journal of Hydrogen Energy*, vol. 32, pp. 3770–3777, 2007.

List of Figures

List of Tables

Band / Volume 660
Recyclingmöglichkeiten für die Keramikkomponenten einer Festoxidzelle
S. Sarner (2025), VIII, 122 pp
ISBN: 978-3-95806-816-2

Band / Volume 661
Methodological Approach Enabling the Two-phase Flow Investigation in Alkaline Electrolysis under Demanding Conditions
S. Renz (2025), IX, 252 pp
ISBN: 978-3-95806-821-6

Band / Volume 662
Variable renewable energy potential estimates based on high-resolution regional atmospheric modelling over southern Africa
S. Chen (2025), XIII, 141 pp
ISBN: 978-3-95806-822-3

Band / Volume 663
Advances in Understanding Nitrate Aerosol Formation and the Implications for Atmospheric Radiative Balance
A. Milousis (2025), 195 pp
ISBN: 978-3-95806-823-0

Band / Volume 664
Optimization of NaSICON-type lithium-ion conductors for solid-state batteries
A. Loutati (2025), viii, 104 pp
ISBN: 978-3-95806-824-7

Band / Volume 665
Innovative Plasma Sprayed Thermal Barrier Coatings for Enhanced Flexibility in Gas Turbine Operation
J. Igel (2025), V, 153, XXXVI pp
ISBN: 978-3-95806-827-8

Band / Volume 666
Techno-ökonomisches Potenzial dezentraler und autarker Energiesysteme
S. K. A. Risch (2025), xxiii, 210 pp
ISBN: 978-3-95806-829-2

Band / Volume 667
Reactive Field Assisted Sintering of Novel Rare Earth Garnets for Plasma Etching Applications
C. Stern (2025), VII, 101, XXVIII pp
ISBN: 978-3-95806-833-9

Band / Volume 668
Effects of mucilage and extracellular polymeric substances on soil gas diffusion
A. Haupenthal (2025), v, 99 pp
ISBN: 978-3-95806-834-6

Band / Volume 669
Quantifying Recombination Losses and Charge Extraction in Halide Perovskite Solar Cells
L. Krückemeier (2025), vi, 286 pp
ISBN: 978-3-95806-835-3

Band / Volume 670
Investigation of Dynamic Material Changes During the Preparation of ZnPd Nanoparticles Supported on ZnO and their Catalytic Application in Methanol Steam Reforming on the Atomic Level
A. Meise (2025), xviii, 175 pp
ISBN: 978-3-95806-838-4

Band / Volume 671
Improving Energy Efficiency of Public Buildings by Influencing Occupant Behaviour using Dashboards and Gamification
E. Ubachukwu (2025), xxi, 191 pp
ISBN: 978-3-95806-840-7

Band / Volume 672
Exploring Plant Responses to Changing Environments: Integrating Phenotyping and Modeling Across Scales
F. M. Bauer (2025), xxix, 188 pp
ISBN: 978-3-95806-845-2

Band / Volume 673
A constitutive theory to represent non-idealities in contacting of SOC interconnect contacts
R. M. Pinto (2025), xii, 139 pp
ISBN: 978-3-95806-846-9

Energie & Umwelt / Energy & Environment
Band / Volume 673
ISBN 978-3-95806-846-9

Mitglied der Helmholtz-Gemeinschaft

JÜLICH
Forschungszentrum